In-situ grown complex metal oxide heterostructures for efficient oxygen evolution and hydrogen evolution reactions

A Dissertation Submitted to the

Indian Institute of Technology Guwahati

in Partial Fulfilment for the Degree of

DOCTOR of PHILOSOPHY

by

Adit Kumar Shah

DEPARTMENT OF CHEMISTRY

INDIAN INSTITUTE OF TECHNOLOGY GUWAHATI

GUWAHATI, ASSAM, INDIA

FEBRUARY 2022

TH-2636_166122040

In-situ grown complex metal oxide heterostructures for efficient oxygen evolution and hydrogen evolution reactions

A Dissertation Submitted to the

Indian Institute of Technology Guwahati

in Partial Fulfilment for the Degree of

DOCTOR of PHILOSOPHY

by

Adit Kumar Shah

Roll No - 166122040

DEPARTMENT OF CHEMISTRY

INDIAN INSTITUTE OF TECHNOLOGY GUWAHATI

GUWAHATI, ASSAM, INDIA

FEBRUARY 2022

TH-2636_166122040

STATEMENT

I hereby declare that the scientific findings included in this thesis entitled, "**In-situ grown complex metal oxide heterostructures for efficient oxygen evolution and hydrogen evolution reactions**" is the outcome of research work carried out by me under the supervision of Prof. Mohammad Qureshi, at the Department of Chemistry, Indian Institute of Technology Guwahati, Assam, India, for the award of the degree of Doctor of Philosophy.

The work embodied in this thesis is the result of original research done by me except where otherwise stated in this thesis with proper citations. I confirm that the investigations were conducted in accord with the ethics policies and integrity standards of the Indian Institute of Technology Guwahati and that the research data are presented honestly and without prejudice. The thesis work has not been submitted for a degree or professional qualification to any other university or institution.

Adit Kumar Shah

IIT Guwahati
February 2022

Adit Kumar Shah
Candidate
Department of Chemistry
IIT Guwahati
Guwahati-781039, Assam
India

TH-2636_166122040

Dr. Mohammad Qureshi
Professor
Department of Chemistry
Indian Institute of Technology Guwahati
Guwahati – 781039, India
Tel: +91 – 361 – 2582320;
Fax: +91 – 361 – 2582349
Email: mq@iitg.ac.in

Certificate

Certified that the work described in this thesis entitled "**In-situ grown complex metal oxide heterostructures for efficient oxygen evolution and hydrogen evolution reactions**" by Mr. Adit Kumar Shah, Department of Chemistry, Indian Institute of Technology Guwahati has been carried out under my supervision and has not been submitted elsewhere for a degree.

Guwahati
February 2022

Mohammad Qureshi
Thesis supervisor
Department of Chemistry
Indian Institute of Technology Guwahati
Guwahati – 781039, Assam, India

TH-2636_166122040

ACKNOWLEDGEMENT

I feel pleased to express my sincere appreciation and gratitude to those who have contributed to the successful outcome of my thesis work and supported me in one way or another in this truly memorial and overwhelming journey.

First of all, I would like to express my sincere gratitude to my thesis supervisor Prof. Mohammad Qureshi for his expert supervision, prudent suggestions, and encouragement, without whom this work would not have been possible. I sincerely thank him for having trust in me and giving me total freedom in choosing the direction of my research. I am fortunate enough to work under his expert guidance which has thought me a lot about scientific research and life in general. Thank you, sir, for continuously helping me in pushing my limits.

I would also like to extend my heartiest thanks to my doctoral committee members, Prof. Aditya Narayan Panda, Dr. Kalyan Raidongia, and Dr. Shyam Prosad Biswas for their valuable suggestions and periodic evaluation throughout my Ph.D. work. I sincerely thank my collaborators, Dr. Nageswara Rao Peela and Devipriya Gogoi for their continuous help and support. I also thank Prof. C. V. Sastri for providing the CH instrument facility. I would like to thank all the faculty members and staff members of the Chemistry department. My sincere thanks to the staff of the Central Instruments Facility, for their help and in hand guidance to several analytical instruments, required during my research work. Special thanks to Dr. Ashim Malakar for giving me the opportunity to operate the TRPL instrument. I wish to express my sincere gratitude to IIT Guwahati for the fellowship and all other facilities that were made available to me and the Ministry of Science and Technology, India for the financial support.

Without a modicum, of doubt MSL team deserve the best and utmost respect for their hard work, diligence, and indispensable input into the overall research work. I would like to thank all my senior group members Dr. Anindya Sundar Patra, Dr. Mohammad Shaad Ansari, Dr. Avishek Banik, Dr. Gaurangi Gogoi, Dr. Tushar Kanta Sahu, my batchmate Dr. Suhaib Alam, present lab members Moite, Sourav, Manoj, Alpana, Nitul and Peeyush for their timely help, support and for creating a pleasant atmosphere in the lab.

A special thanks to all my friends in and out of IIT Guwahati Sulendar, Deepjyoti, Raja, Bikash, Prabir, Sansuma, Mintu, Umesh, Siddharth, Nashim, Tukhar, Bikash, Arnob,

TH-2636_166122040

Subajit, Pappu, Nitin, Vinay, and all the members of my morning football team for giving me unforgettable moments, emotional support, and delightful experiences. I would also like to thank all the tea stalls inside the campus, mess workers, and housekeeping for providing good food and clean surroundings, which made my stay in the campus pleasant.

Finally, my Ph. D. endeavor could not have been completed without the endless love, unending support, tolerance, and blessings from my family. I would like to express my deepest gratitude to my parents (Mr. Om Prakash Shah & Mrs. Prem Kumari Shah) for their prayers, unconditional love, and sacrifices they have made to complete my dreams. I am also grateful to my sisters (Rinku & Punam) and brother (Ajith) for their eternal love, affection, and emotional support which had immensely needed during my Ph.D. tenure.

Still many, more names are missing whose contribution and help are worth mentioning.

Adit

TH-2636_166122040

TABLE OF CONTENTS

TH-2636_166122040

TH-2636_166122040

TH-2636_166122040

Dedicated To

Maa, Papa

&

Bhai

TH-2636_166122040

Thesis Title:	**In-situ grown complex metal oxide heterostructures for efficient oxygen evolution and hydrogen evolution reactions**
Name of the Candidate:	Adit Kumar Shah
Registration Number:	166122040
Thesis Supervisor:	Prof. Mohammad Qureshi
Department:	Chemistry
Institute:	Indian Institute of Technology Guwahati, Assam – 781039, India.

Thesis Overview

Chapter 1: Current chapter discusses the urgent necessity to move towards a clean and renewable way of energy production, as excessive use of non-renewable resources cause's issues like climate change, rise in global temperature, and many more. The present chapter also includes a brief literature survey of current state-of-the-art scenarios and challenges related to the development of efficient, cost-effective, and easily synthesizable, working electrodes. This chapter is concluded with objectives and motivation behind designing different semiconductor metal oxides-based electrodes for (photo) electrochemical water splitting applications.

Chapter 2: This chapter discusses the detailed synthetic protocols of catalysts, used for (photo)electrochemical application, it also discusses instrumentation techniques used for material and (photo)electrochemical characterization. The amount of gas that evolved during the water-splitting process is measured and analysed through online gas chromatography. The in-situ growth of the catalysts directly over the conductive substrate is also discussed in the conclusion of this chapter.

Chapter 3: RGO-$CuBi_2O_4$ heterojunction as a photocathode for efficient hydrogen evolution reaction (Sustainable Energy & Fuels, 2019, 3, 1554)

In this chapter, noble metal-free $CuBi_2O_4$ composited with RGO layers was proposed as an efficient photoelectrochemical water-reducing catalyst. Herein, p-type $CuBi_2O_4$ directly fabricated over FTO overlaid with reduced graphene oxide (RGO). $CuBi_2O_4$ with an optimized

TH-2636_166122040

number of RGO deposition cycles displayed the highest current density, which is ~2 times higher than that of the pristine $CuBi_2O_4$ photocathode.

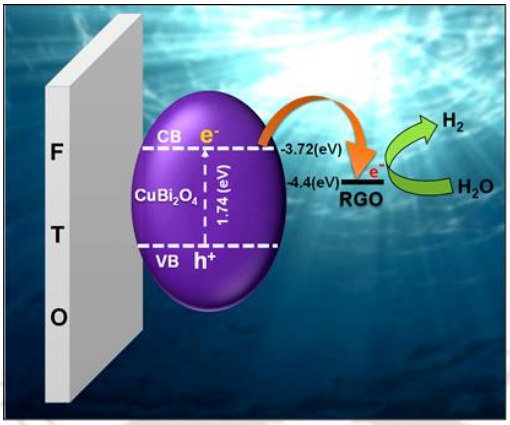

Figure 3.1. Schematic representation of reduced graphene oxide coated onto noble metal-free $CuBi_2O_4$ for favorable charge recombination kinetics to enhance solar hydrogen production.

Average faradaic efficiency of 91.7% was achieved, indicating that the photocurrent generated in the RGO modified $CuBi_2O_4$ photocathode is attributed solely to the water reduction. With RGO modification over $CuBi_2O_4$, charge carrier density increases from 3.76 X 10^{20} cm^{-3} to 7.92 X 10^{20} cm^{-3} obtained from Mott–Schottky plots. Schematic representation of reduced graphene oxide coated onto noble metal-free $CuBi_2O_4$ for favorable charge recombination kinetics to enhance solar hydrogen production, is shown in figure 3.1.

Chapter 4: Surface-engineering decahedral indium doped bismuth vanadate using g-C_3N_4 quantum dots for improved oxygen evolution reaction (J. of Power Sources 2020, 477, 229024)

Here in this chapter, we chose monoclinic $BiVO_4$ and g-C_3N_4 quantum dots (CNQDs) as a model system to perform photoelectrochemical water oxidation. Here, melamine was used for the low-temperature green synthesis of CNQDs. Indium-doped $BiVO_4$ with decahedron morphology was synthesis directly over FTO and CNQDs was incorporated to form type II heterojunction for enhanced water oxidation efficiency of ($BiVO_4$:In)-CNQD photoanode.

TH-2636_166122040

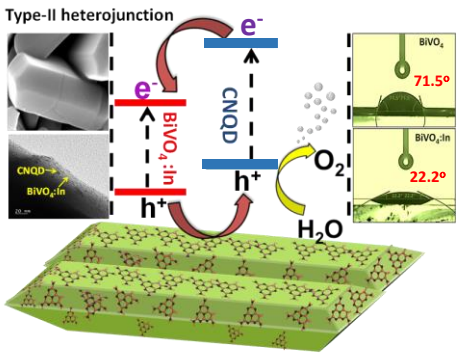

Figure 4.1 Schematic representation of Indium doped $BiVO_4$ with decahedron morphology synthesis directly over FTO and CNQDs was incorporated to form type II heterojunction for enhanced water oxidation efficiency of (BiVO4:In)-CNQD photoanode.

A photocurrent density of ~2.42 mA/cm^2 with an average Faradaic yield of 90%, which is ~4- folds higher than its pristine counterpart. ($BiVO_4$:In)-CNQD photoanode shows a ~5 fold increase in charge carrier density to 7.7×10^{20} cm^{-3}, and a significant cathodic shift of 136 mv was also observed than its pristine counterpart. Indium in $BiVO_4$ favours the creation of oxygen vacancies, which improves charge separation and charge carrier density in $BiVO_4$:In photoanode. It is also observed that the $BiVO_4$:In photoanode shows higher surface hydrophilic characteristics, resulting in more polar surface and water adsorption on the surface, leading to more active water at the reaction site. Schematic representation of Indium doped $BiVO_4$ with decahedron morphology synthesis directly over FTO, and CNQDs was incorporated to form type II heterojunction for enhanced water oxidation efficiency of ($BiVO_4$:In)-CNQD photoanode is shown in figure 4.1

Chapter 5: Hollow cuboidal $MnCo_2O_4$ / nickel phosphate heterojunction: A promising oxygen evolution reaction electrocatalyst (Chem. Commun., 2021, 57, 8027)

In this chapter, $MnCo_2O_4$ with hollow cuboidal morphology was synthesised directly over a low-cost substrate hydrothermal procedure. In-situ growth of hollow cuboidal $MnCo_2O_4$ (h-MCO) over FTO provides good ohmic contact, which helps in faster charge transfer between hollow cuboidal MCO and FTO. Deposition of nickel phosphate (NiPi) over h-MCO through electrodeposition method, enhances the OER activity of modified h-MCO/NiPi electrode to a lower overpotential of 230 mV and Tafel slope to 57 mV/dec.

TH-2636_166122040

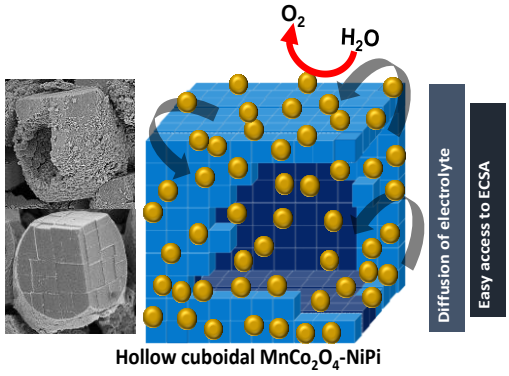

Figure 5.1 Schematic representation showing growth of unique hierarchical hollow-cuboidal complex metal oxide directly on the substrate coupled with nickel phosphate.

A high C_{dl} value of 31.9 mF/cm^2 signifies more available electrochemically surface active sites on the composite with a TOF of 0.23/sec which is ~ 3 fold higher than its pristine counterpart. h-MCO/NiPi shows excellent long-term stability of 30 h without any significant decrease in current density, with a Faradic yield of 98 % confirming that the current generated is only due to the OER activity of the catalyst. High stability, low cost, and green synthesis procedure mark h-MCO/NiPi as one of the futuristic catalysts to be used in industrial applications. Figure 5.1 shows, the growth of unique hierarchical hollow-cuboidal complex metal oxide directly on the substrate coupled with nickel phosphate. Figure 5.2. (a, b, c, d) shows the FESEM images of h-MCO, FETEM image of composite, and h-MCO/NiPi HRTEM image of h-MCO respectively. Figure 5.2. (e, f) display, linear sweep voltammetry (LSV) plot, and stability test of h-MCO/NiPi and pristine h-MCO electrodes, respectively.

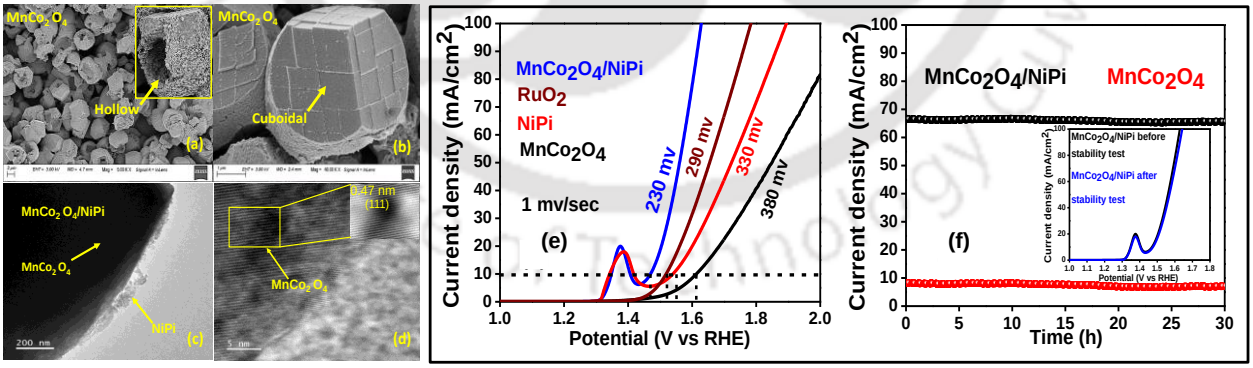

Figure 5.2 (a, b) FESEM images of h-MCO. (c) FETEM image of composite h-MCO/NiPi, (d) HRTEM image of h-MCO. (e) Linear sweep voltammetry (LSV) plot. (f) Stability test of h-MCO/NiPi and pristine h-MCO electrodes.

Chapter 6: Cuboidal $MnCo_2O_4$/h-boron nitride heterojunction: Enhanced oxygen evolution reaction via efficient hole extraction approach (ACS Appl. Energy Mater. 2022, 5, 1551)

TH-2636_166122040

In this chapter, surfactant-free cuboidal $MnCo_2O_4$ was grown directly over low-priced FTO substrate by a green hydrothermal method, providing a good ohmic contact, which helps in faster charge transfer between cuboidal $MnCo_2O_4$ and FTO interface. Cuboidal $MnCo_2O_4$ modified with metal-free h-BN nanosheets, which exhibits excellent hole extraction ability assisting in the upsurge of OER activity in C-MCO/h-BN heterostructure. C-MCO/h-BN displays an overpotential of 240 mV and a Tafel slope value of 66 mV/dec, making the electrode an efficient OER active catalyst.

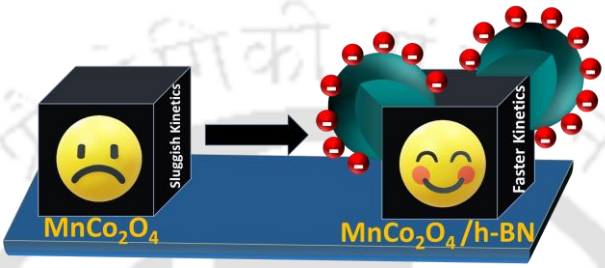

Figure 6.1 Schematic representation showing deposition of h-boron nitride over cuboidal $MnCo_2O_4$ for enhanced water oxidation efficiency.

Surface modified C-MCO/h-BN shows faster charge transfer kinetics at the working electrode and the electrolyte interface, C-MCO/h-BN shows ~5.5-fold enhancement in C_{dl} than its pristine counterpart, indicating more accessible electrochemically surface-active sites on it, therefore ~ 2.8-fold enhancement in TOF was observed. Green and sustainable C-MCO/h-BN electrode, shows excellent OER activity and exhibits 35 h of outstanding long-term stability in harsh alkaline conditions, thus it has the potential to be used in large-scale industrial applications. Figure 6.1 shows, a schematic representation showing deposition of h-boron nitride over cuboidal $MnCo_2O_4$ for enhanced water oxidation efficiency. Figure 6.2. (a, b, c, d) shows, FESEM image of in-situ grown C-MCO, FESEM image of h-BN nanosheets, FETEM image of C-MCO/h-BN showing deposition of h-BN nanosheets over C-MCO, HRTEM image of C-MCO/h-BN, d-spacing values of 0.3 nm and 0.21 nm corresponds to (220) and (101) plane of C-MCO and h-BN nanosheets, respectively. Figure 6.2. (e, f) linear sweep voltammetry (LSV) plot, stability test of C-MCO/h-BN and pristine C-MCO electrodes, respectively.

TH-2636_166122040

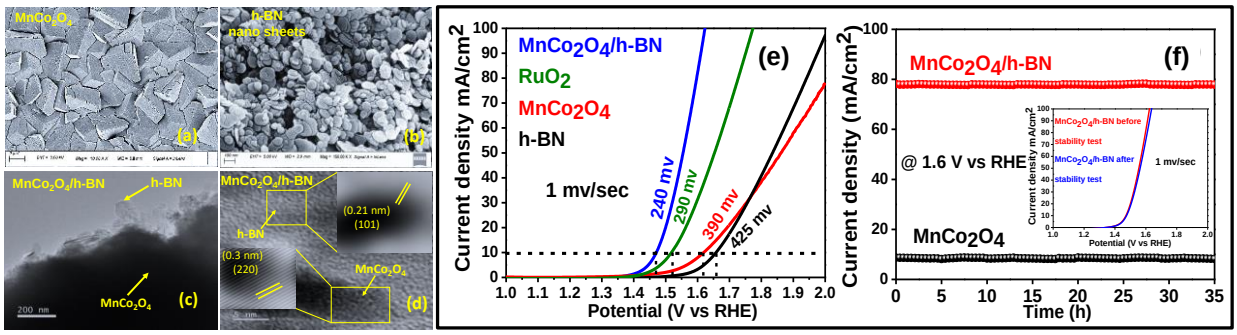

Figure 6.2 (a) FESEM image of in-situ grown C-MCO. (b) FESEM image of h-BN nanosheets. (c)FETEM image of C-MCO/h-BN, showing deposition of h-BN nanosheets over C-MCO. (d) HRTEM image of C-MCO/h-BN, d-spacing values of 0.3 nm and 0.21 nm corresponds to (220) and (101) plane of C-MCO and h-BN nanosheets respectively. (e) Linear sweep voltammetry (LSV) plot. (f) Stability test of C-MCO/h-BN and pristine C-MCO electrodes.

Chapter 7: Thesis overview and future perspectives

The current chapter, in short, summarizes the conclusions and the overview of the present thesis. Herein, it also discusses the possible modification in the near future that can be done with the metal oxides to enhance OER and HER performance.

TH-2636_166122040

CHAPTER 1

Introduction

This chapter describes how the water-splitting technique can play a crucial role in overcoming the crisis of global warming and increased energy demands. It also discusses the working principle of (photo)electrochemical water splitting. The present chapter also includes a brief literature survey of current state-of-the-art scenarios and challenges related to the development of efficient, cost-effective, and easy synthesizable working electrodes. This chapter also comprises several strategies which are adopted to enhance the water-splitting efficiency of the semiconductors.

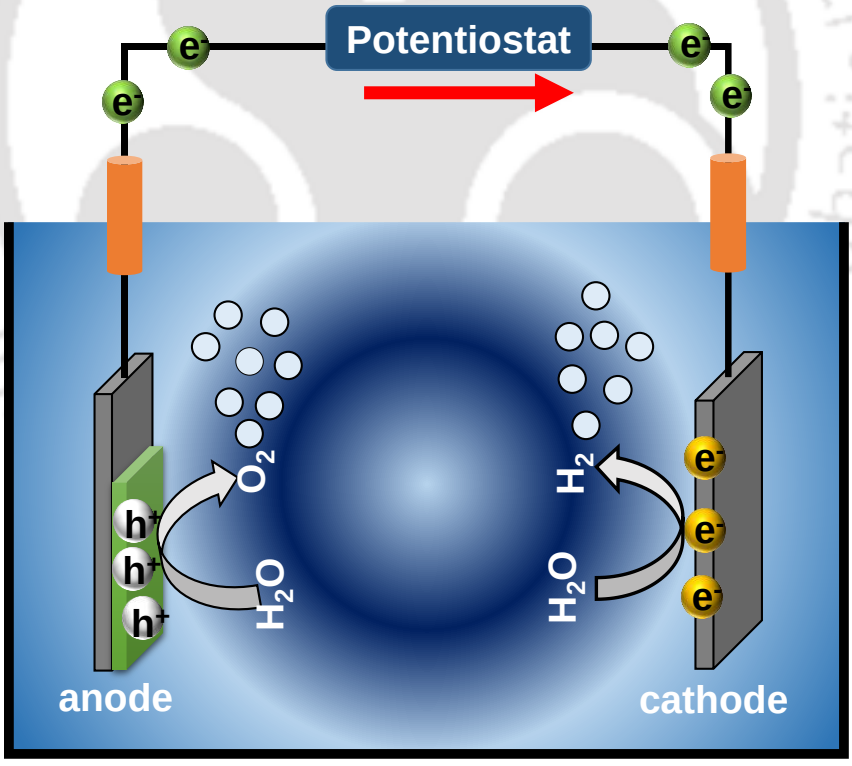

1.1 GLOBAL ENERGY AND ENVIRONMENTAL CHALLENGES

Worldwide massive energy need and environmental pollution are the major issues to be handled in the present time.[1] As, currently a major portion of the world's energy needs are fulfilled by fossil fuels, which leads to excessive emission of greenhouse gases (CO_2, CH_4, N_2O, etc.), creating significant concerns like climate change, rise in the earth's temperature, pollution and health hazards.[2] Countries and regions have united to establish different plans to diminish and eliminate excessive greenhouse gas emissions. The Kyoto Protocol and Paris Climate Agreement are the two excellent illustrations of the determination and cooperation of human beings, to fight against this crisis.[3-4] Conferring to the reports of the Intergovernmental Panel on Climate Change (IPCC), it has been agreed to stay within a goal of 2 ℃ rise above the pre-industrial global average temperature, by 2050.[5] In general, reduction of fossil fuel usage and decline of carbon emissions from fossil fuel is very crucial to control the emission of carbon into the atmosphere. Although non-conventional and nuclear energy sources have been established at a firm pace, they are still not been fast enough to considerably lessen the fossil fuel usage. According to U.S. Energy Information Administration (EIA), shown in **Figure 1.1 (a)**, it is estimated that in a few decades (from 2010 to 2050) that global energy demand will escalate by ~ 50%.[6] However, despite the sharp drop in fossil fuel consumption, oil continued to be a major energy source with a share of 31.2%, coal (27.2%), and natural gas (24.7%), of world energy consumption, while only 5.7% of the world's energy demands are accomplished by renewable energy sources, as shown in **Figure 1.1 (b)**. In 2018, fossil fuels bear 80% of the global energy demand and are anticipated to still account for 68% in 2050. Hence, in the calculable future, it is estimated that a major portion of the world energy requirements will still mainly come from fossil fuels.

Fossil fuel consumption also needs a check due to the release of a huge amount of CO_2, SO_x, and particulate into the atmosphere.[7] Each year, emissions of CO_2 is estimated to rise by

TH-2636_166122040

~ 3%.[8] CO_2 in the atmosphere absorbs infrared radiation from Sunlight, and hence, increases the average temperature of the earth. The advancement of new technologies is crucial to come across the present and future energy demands, and check the emission of greenhouse gasses. To minimize the reliance on fossil fuels as an energy source, new greener, and renewable alternatives have been searched and proposed as solutions for clean and efficient energy resources.

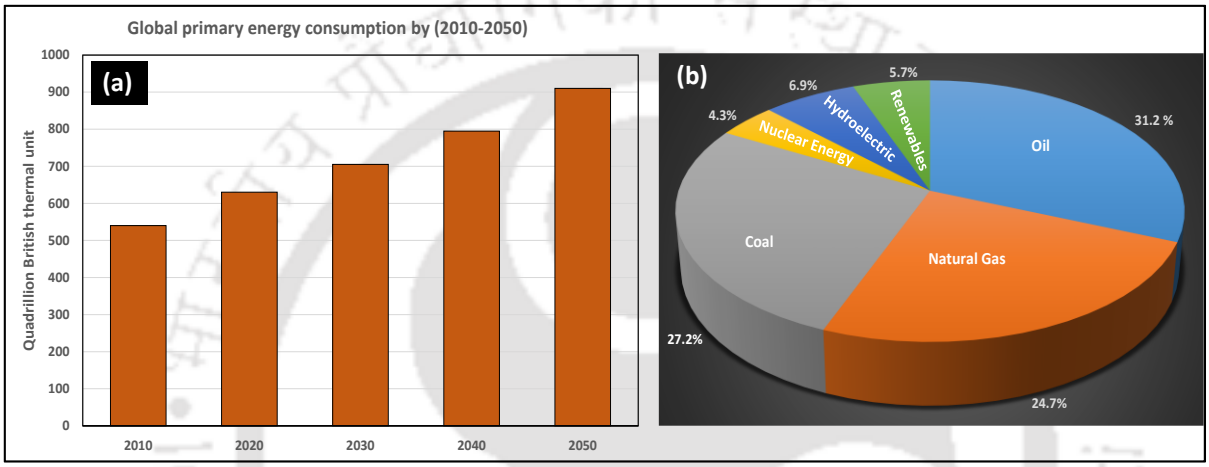

Figure 1.1 (a) Showing estimated worldwide energy consumption. (Source. U.S. Energy Information Administration, International Energy Outlook 2019). (b) Showing the Primary global energy consumption by category in the year 2020 (source. https://www.forbes.com/sites/rrapier/2021/07/11/highlights-from-the-bp-statistical-review-of-world-energy-2021).

1.2 RENEWABLE ENERGY SOURCES

Currently, researchers have extensively strived to use inexhaustible and renewable energy to address the concerns of global warming and increasing energy demand. There are several available renewable resources, such as Sunlight, tides, wind, geothermal heat, and hydropower, which are cleaner and zero CO_2 emitters.[7] Amid the existing renewable energy sources, Sunlight is the most abundant and consistent source of energy. Sun emits solar energy at the rate of 3.8×10^{23} kW, out of which ~ 1.8×10^{14} kW is captured by the earth.[9] Solar energy has great potential to meet current and future global energy demand, moreover can

TH-2636_166122040

overcome present environmental calamity. In addition to being renewable, solar energy, due to the absence of harmful environmental side effects associated with its use is generally considered a "green" source of energy.

Energy from solar power is often used to generate electricity or heat, through different available technologies, among which, solar thermal, photovoltaic, and solar fuels, are prime solar energy harnessing technologies.[10] Therefore, it is essential to advance towards the energy sources that are storable, clean, and inexpensive. An ideal alternative for proper utilization of solar energy is to convert solar energy to chemical energy and store it for future use. In this context, hydrogen can be considered as a potential energy carrier to store and transport the natural form (chemical) of renewable energy.[11] The Earth's surface is mainly covered with 71% of water, thus, it can be the most suitable source for the purest form of H_2 generation.[12] Thus, solar water-splitting has been an essential factor in order to reduce the CO_2 emission in the atmosphere.

When compared to several conventional sources of energy such as gasoline (46.4 MJ kg^{-1}), kerosene (46.2 MJ kg^{-1}), diesel (45.6 MJ kg^{-1}), and methane (55.5 MJ kg^{-1}), hydrogen also known as zero-emission fuel has a higher calorific value of ~141.7 MJ kg^{-1}.[13,14] Coal gasification and steam reforming methane gas are currently major sources of H_2 production on an industrial scale, which in turn emit a large amount of greenhouse gases.[15] Hence, for sustainable, cost-efficient, carbon-free, and with high efficacy, H_2 production, there is an urgent need for an unconventional technology. Recently several technologies are used for H_2 production, amid which (Photo)electrochemical water-splitting technique has the potential to grow into an extensive pathway for imminent energy production.

TH-2636_166122040

1.3 (PHOTO)ELECTROCHEMICAL WATER-SPLITTING

In plants, Sunlight is used to convert water and CO_2 into O_2 and carbohydrates called, natural photosynthesis (NP). Photoelectrochemical water splitting (PEC) mimics the NP of producing H_2 by splitting water using Sunlight, converting water into H_2 and O_2, also named artificial photosynthesis.[16] Photoelectrochemical water splitting (PEC) was first reported by Fujishima and Honda in 1972, since then many efforts are made to improve the water-splitting efficiency for hydrogen production.[17] With a similar structure as a conventional electrolysis system, PEC water-splitting technique is also comprised of, electrolyte and two electrodes, where at least one electrode is photoactive.[18,19] **Figure 1.2** shows the basic principle of water-splitting. In the PEC process when Sunlight shines over a semiconducting material (photoanode), it absorbs photons and the electrons from their valence band get excited to the conduction band, thereby generating an electron-hole. Light-induced electron-hole pairs need to be separated to avoid eventual recombination. Electrons (e^-) through the external circuit move to the cathode to take part in the water reduction process to produce H_2 and the holes (h^+) transfer to the semiconductor/electrolyte interface and oxidize water into O_2.[20, 21] Solar energy is plentiful but tends to be unpredictable and intermittent. As our dependence on renewable energy raises, there will be an increasing need to store this energy for times when the Sun is not shining.[22] As Sunlight is not available during night time, and various region on earth for a certain period of time does not receive Sunlight or it is not intense enough to carry out PEC water-splitting. To carry out water-splitting 24 X 7, the electrochemical water-splitting technique was adopted. Herein, the basic process of water-splitting remains similar to PEC, only the difference is electron-hole pair generation. In PEC, electron-hole pairs are generated

TH-2636_166122040

by absorbing energy from Sunlight, while in the electrochemical water-splitting technique they are generated by applying a potential to semiconducting material from an external source.[23, 24]

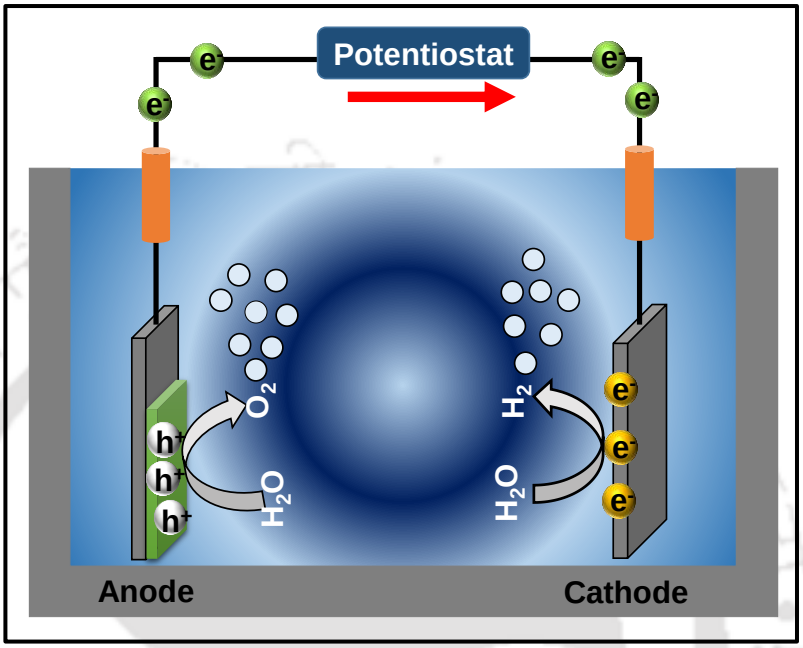

Figure 1.2. Schematic showing oxidation of water at the anode and reduction at the cathode to produce O_2 and H_2 respectively, inside a (photo)electrochemical cell. (ref. 21, 23)

The chemical reaction takes place on respective electrodes during (photo)electrochemical water-splitting process in neutral and basic conditions are as follows: [25-27]

$$\text{Anode: } 2H_2O + 4\,h^+ \longrightarrow O_2 + 4H^+ \quad (1.1)$$

$$\text{Cathode: } 4H^+ + 4e^- \longrightarrow 2H_2 \quad (1.2)$$

$$\text{Overall: } 2H_2O \longrightarrow 2H_2 + O_2 \quad (1.3)$$

Alkaline conditions:

$$\text{Anode: } 4OH^- + 4h^+ \longrightarrow O_2 + 2H_2O \quad (1.4)$$

$$\text{Cathode: } 4H_2O + 4e^- \longrightarrow 2H_2 + 4OH^- \quad (1.5)$$

TH-2636_166122040

$$\text{Overall: } 2H_2O \longrightarrow 2H_2 + O_2 \qquad (1.6)$$

$$\Delta G = +237.2 \text{ kJ/mol} \approx 1.23 \text{ eV}$$

The water-splitting is an uphill process with a change in Gibbs free energy of 237.2 KJ/mol, corresponding to 1.23 eV. The oxidation potential of H_2O/O_2 is 1.23V vs. normal hydrogen electrode (NHE) and the reduction potential of H^+/H_2 is 0V vs NHE. Therefore, at least a bandgap of 1.23 eV is required to enable water-splitting in semiconducting materials. Band positions of a semiconductor are another factor that governs its water-splitting capability. The valence band of the semiconductor must be more positive than the oxidation potential of H_2O/O_2, while the conduction band must be more negative than the reduction potential of H^+/H_2, for oxidation and reduction of water to take place respectively on its surface.[28-30]

During PEC water-splitting process, photo induced processes involved on the surface and inside a semiconductor electrode are shown in **Figure 1.3**. The steps are as follows, (i) absorption of light, (ii) charge separation, (iii) bulk and surface recombination, (iv) charge injection.[31, 32]

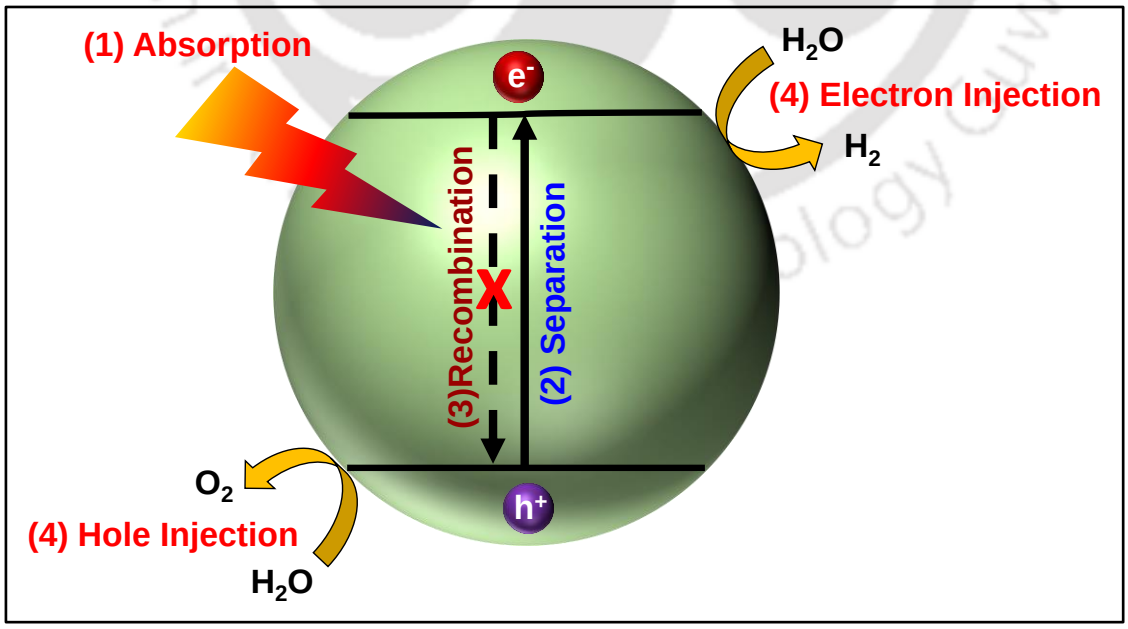

Figure 1.3. Schematic diagram showing various steps involved in PEC water-splitting.

TH-2636_166122040

1.4 DIFFERENT STRATEGIES TO IMPROVE (PHOTO)ELECTROCHEMICAL PERFORMANCE

After the revolutionary work by Fujishima and Honda in 1972, the PEC water-splitting reaction has been largely explored as a promising H_2 source. Numerous semiconductor metal oxides have been investigated to show (photo)electrochemical water-splitting activity. [33-36] Complete solar spectrum accounts for 45% for visible light, only about 5% UV, and 50% for near-infrared (NIR) light.[38,39] In PEC, to carry out water-splitting, minimum photon energy of 1.23 eV is essential (corresponding to wavelengths <1010 nm) to trigger the PEC process in a semiconductor.[37] Hence, it is very important to choose semiconducting materials having a bandgap >1.23 eV and can absorb the maximum portion of the solar spectrum.

Under standard conditions, theoretically, the potential at which water-splitting takes place is 1.23 V. However, because of the existence activation barrier of anode and cathode as well as other resistance such as contact and solution resistances, the high potential that is higher than the theoretical value is always required to initiate the water-splitting. [40] The difference between the applied potential and theoretical value (1.23 V) is overpotential, which is effectually lowered by using highly active OER (oxygen evolution reaction) and HER (hydrogen evolution reaction) catalysts. Hence, in the electrochemical water-splitting technique, the main objective of using catalysts is to execute water-splitting at lower overpotential with faster reaction kinetics, thereby resulting in efficient OER and HER activity.[41] For superior (photo)electrochemical water-splitting device, the following critical criteria should meet: (1) absorbing broad range of solar spectrum, (2) efficient charge separation, (3) efficient charge transfer towards the surface of the semiconductor, (4) effective charge injection at electrode-electrolyte interface, (5) lesser overpotential, (6) sufficient

TH-2636_166122040

number of electrochemical active sites, (7) faster water oxidation and reduction kinetics, (8) long term stability in a wide range of pH.

It is been observed that semiconductor metal oxides are way away from their theoretical water-splitting efficiency. Hence, various strategies are applied to metal oxide-based electrodes to improve the efficiency of each step as mentioned above and summarised in **Figure 1.4**, which are as follows: (a) quantum dot sensitization, (b) elemental doping, (c) morphology modulation, (d) heterojunction formation, (e) co-catalyst formation, (f) hole/electron extracting layers.

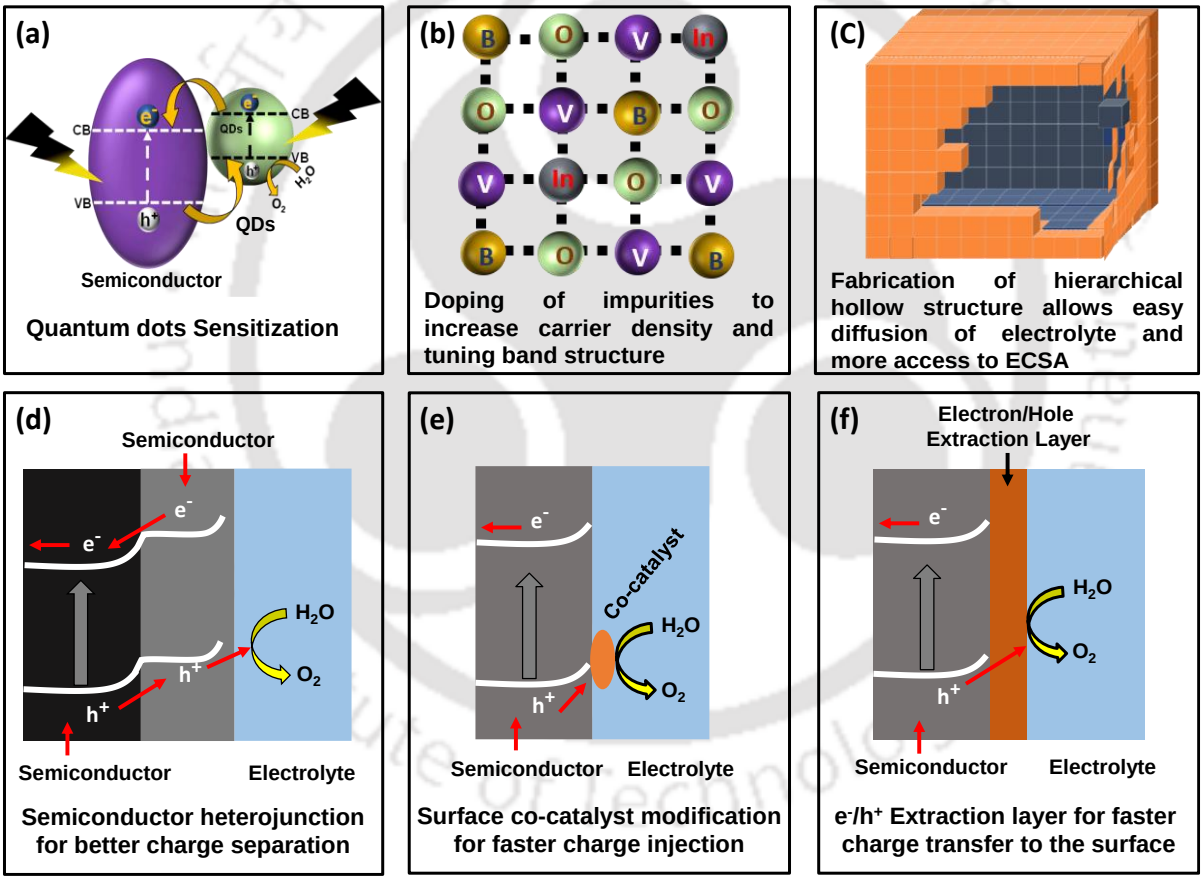

Figure 1.4. Schematics showing various strategies adopted for the enhancement in (photo)electrochemical water-splitting efficiency of metal oxide-based electrodes (Ref. 42-48).

1.4.1 Quantum Dot Sensitization

Many great efforts have been made to develop efficient dye-sensitized photoelectrodes to carry out PEC water-splitting, however their low current density and poor stability, limit

TH-2636_166122040

their further practical applications in PEC.[49] The semiconductor (quantum dots) QDs, such as CdS QDs, CdTe QDs, CdSe QDs, etc., shows many advantages in terms of durability, absorptivity, tunability, and when compared with organic dye molecules.[50-56] Thus considered as a promising alternative for PEC water-splitting application. Firstly, due to quantum confinement effects, QDs show size-dependent absorption property. It implies we can improve the exploitation of solar spectrum, by controlling their sizes. Secondly, the charge separation and migration in a semiconductor can be enhanced by modulating the band positions of QDs.[57-66] Moreover, easy-to-surface modification and high surface binding sites, make QDs ready to incorporate with other semiconducting materials.[67] These properties of QDs make it promising and versatile sensitizers for making efficient and stable PEC devices. Recently, non-metallic QDs, such as graphene and g-C_3N_4 quantum dots, have appeared as the possible advanced materials that holds promise in environmental and energy applications.[68]

In oxygen evolution reaction (OER), to achieve enhanced OER performance, it is important to increase exposed surface area and the number of active sites. The QDs is known for its high surface-to-volume ratio; thus, provides more active sites for OER activity, therefore results in better electrochemical activity.[69]

1.4.2 Elemental Doping

Tuning the electrical properties of semiconductor materials by doping foreign elements is a promising strategy.[70-73] Through doping, other elements (metallic or non-metallic) are introduced into the semiconductor lattice to modify its electronic properties such as the band-gap of the material, donor density, and charge mobility. In many cases, doping not only enhance the absorption of visible light due to the formation of localized or delocalized electronic states, but also enhance the separation efficiency of photo-generated electron-hole pairs.[74-76] N-doped ZnO nanorods was fabricated by Wang *et al*., distributed with a gradient concentration along the c-axis. The absorption abilities of N:ZnO in the visible range were improved with an

TH-2636_166122040

increase in the concentration of N.[77] Doping semiconductor with a heteroatom having different size and valence, helps in stabilizing and introducing oxygen vacancies (O_{vac}) in the material.[78,79] With the occurrence of surface O_{vac}, space charge region width is reduced, resulting in enhanced charge separation and transfer. Moreover, from the kinetics viewpoint, the surface O_{vac} could also increase the surface hydrophilicity.[80] For example, Jiang and Miao have doped Zn in CoOOH, showing the creation of oxygen vacancies and indicating that the oxygen vacancies are created when the Zn replaces the lattice site of Co.[81] Several reports on doping shows that there is an enhancement in the adsorption of water molecules on the surface of semiconducting material, with the creation of oxygen vacancies in it, hence results in enhance photocatalytic activity.[82] N/Si co-doped TiO_2 nanorods were fabricated by Zhang *et al*. via a one-step hydrothermal process. TiO_2 nanorods displayed enhanced light-harvesting with N/Si co-doping. It also demonstrated better electrical conductivity by the improved donor density with co-doping.[83] Jo *et al*. in an attempt to make doping simultaneously at the bismuth and vanadium sites in $BiVO_4$, through In^{3+} and Mo^{6+} dual doping were able to enhance water-splitting performance in $BiVO_4$. However, no significant enhancement in light absorption was observed.[84]

Elemental doping is the most efficient way to engineer the activity of OER catalysts. Doping with metallic elements or non-metallic is widely considered to be an effective approach for generating active sites in the catalyst.[85,86] Doping tune the electronic structure, hence influencing the binding energy of OER intermediates, such as*O–OH, *O, and *OH.[87] Hence, doping provides an effective way to achieve long-term stability and large-scale activity under harsh applied anodic overpotential. Additionally, dopants can also greatly accelerate charge transfer, optimize the hydrogen adsorption free energy, and improve electrochemical active sites, enhance the electrocatalytic performance.

TH-2636_166122040

1.4.3 Morphology Modulation

The syntheses and morphology modulation of semiconductors are important as they offer a higher number of active sites for (photo)electrochemical water-splitting.[88] Several reports have shown various morphologies and their growth mechanisms. Morphology design and engineering of semiconductors can alter their key properties such as electrical conductivity, specific surface area, crystallinity, reaction kinetics, overpotential, number of active sites and optical absorbance.[89-91] They are optimised all together, to achieve stable and enhanced water-splitting efficiency. Moreover, by providing shorter paths for charge transport and improved charge separation, by morphology tuning of semiconductors, promotes their HER and OER activity.

In the case of a 0-D nanoparticles catalyst, the charge carriers travel through random pathways to reach the collecting electrode. Therefore, 0-D shows high e-h recombination with a high population of trap sites. While the one-dimensional (1D) nanostructures show excellent charge carrier transporter, they have less exposed surface area for water-splitting reaction. Nanowires,[92] nanorods,[93] nanobelts,[94] and nanotubes,[95] are examples of 1D-nanostructures, which exhibited enhanced water-splitting performance. Two-dimensional (2-D) materials commonly hold a large surface area which is helpful in providing better contact between the electrolyte and photoanode.[96] Nanoplates and Nanosheets are the typical representatives of 2-D materials.[97, 98] Three dimensional (3-D) nanostructures, another effective way to reduce overpotential for catalytic activity and efficient absorption of light. 3D-nanomaterials, with significantly increased surface area and a much higher numbers of active sites are gaining larger attention in (photo)electrochemical water-splitting applications.[99] For instance, Wang *et al.* synthesized self-assembled 3D foam-like $NiCo_2O_4$, which provides good electrocatalytic activity towards the OER.[100] $NiCo_2O_4/Ni_2P$ core-shell nano-cone array were synthesized by

TH-2636_166122040

Luyu Wang *et al.;* and the catalyst was found to enlarge the active sites in electrocatalytic water-splitting.[101] Different morphologies of catalyst used for (photo)electrochemical water-splitting, shown in **Figure 1.5**.

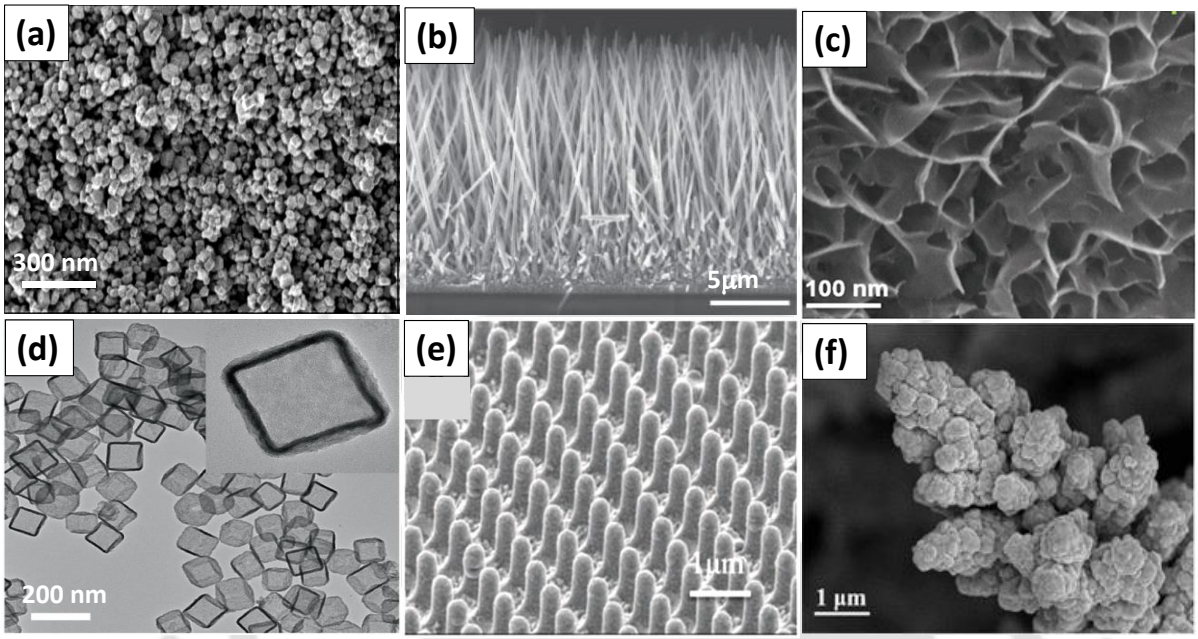

Figure 1.5. Some examples associated to application of different nanostructure morphologies in (photo)electrochemical water-splitting. (Ref.102- 107)

1.4.4 Co-Catalyst Modifications

Oxygen and hydrogen evolution half-reactions, which involve multi-electron transfer reactions, is one of the biggest challenges to overcome the thermodynamically uphill water-splitting.[108] Co-catalysts facilitate photocatalytic reactions by accommodating excited electrons/holes and undergoing redox reactions on the surface of the semiconductor. Generally, by oxidation of the metallic element of the co-catalyst itself, facilitates oxidation reactions of water. Co-catalysts plays a crucial role in improving both the reliability and activity of semiconductor in (photo)electrochemical water-splitting. (i) Co-catalysts could lower the activation energy or overpotential for H_2 or O_2 evolution reactions on the surface of semiconductors, (ii) Co-catalysts enhance charge separation at the semiconductor/co-catalyst interface, (iii) Co-catalysts reduces the photo-corrosion and enhance the stability of

TH-2636_166122040

photoelectrode.[109] Ability of O_2 and H_2 evolution in a co-catalyst modified semiconductor is affected by many reasons, such as the co-catalyst loading amount, structure, and particle size. Too much loading of co-catalysts on the surface of the semiconductor leads to the shielding of the incident light, and therefore prevent the absorption of light and generation of photogenerated charge carriers in the semiconductor.[110, 111] Noble metal oxides such as RuO_x and IrO_x have been studied as conventional co-catalysts for the water oxidation reaction.[112-114] Despite having strong activity, the high cost of Ru and Ir and their low abundance make them less suitable to use in water oxidation. Due to their low-cost, first-row transition metal oxides are usually used as co-catalyst to overcome the drawback of poor OER kinetics to accomplish a higher OER activity and decent reaction rates. Amid several metal oxide-based OERs, cobalt oxide and manganese oxide have appeared as effective water oxidation co-catalysts and can operate under neutral and harsh alkaline conditions.[115] For instance, the electrocatalytic function of the well-known co-catalyst, Co-Pi, is accompanied with oxidation from Co(II) to Co(III) and Co(IV), leading to the creation of high-valence Co(IV)-O intermediates.[116-118] Recent work has displayed that with metals such as Cr on the MoS_2 nanosheets surface showed enhanced stability and photocatalytic activity during photocatalytic hydrogen evolution compared to pristine MoS_2.[119] Several electrocatalysts such as NiCo, Mn-Bi, CoAl, NiFe, Ni-Bi, Ni_4O_4, CoFe-PB, NiOOH, FeOOH, and CoOOH, were widely used to enhance the oxygen evolution reaction.[120-129]

1.4.5 Semiconductor Heterojunction

In comparison to single component photocatalysts, heterojunction semiconductors are an effective system for charge separation and transport of photogenerated charge carriers. In photoelectrochemical water-splitting it has been demonstrated that the heterojunction semiconductors show greatly enhanced water-splitting activities. In designing a heterojunction, the energy level of each coupling material needs to have nearly matched overlapping band

TH-2636_166122040

structures. Heterojunctions can be separated into Z-scheme, (Type-I, Type-II, and Type-III) heterojunction and p–n heterojunction.[130-136] In type I heterojunction, both the photogenerated holes and electrons in one semiconductor (A) transfer to another semiconductor (B) with more negative CB and a more positive VB. The transfer of photogenerated holes and electrons from TiO_2 to Fe_2O_3 is an example of type-I heterojunction.[137] In type II heterojunction, the valance band (VB) position of A has more positive than (B), but the conduction band (CB) position of material B is more negative than material A. Consequently, electrons and holes transfer in reverse ways, the hole flows from A to B and the electron flows from material B to A. One example of a type II heterojunction system is, WO_3–$BiVO_4$ heterojunction. This kind of flow charge results in efficient charge separation and thus improves its photocatalytic performance.[137] Band structure type III heterojunction is alike to type II heterojunction. In heterojunction, the difference between the VB and CB of two materials is larger, which delivers a higher driving force for charge transfer hence resulting in enhanced photocatalytic performance. The photogenerated hole from material B combines with the electrons from material A, and the hole from material A and the electron from material B participate in the oxidation and reduction of water respectively. The Sb_2Se_3 and FeS_2 system denote type III heterojunction.[137] In p-n heterojunction at the interface between p and n-type semiconductors internal electric field arises due to the diffusion of charge carriers between both the semiconductors. The internal electric field pushes holes to the valence band of p-type semiconductor and electrons to the conduction band of n-type semiconductor. Hence, the existence of the inner electric field in p-n heterojunction effectively separates holes and electrons. Zhu *et al*. by wet chemical synthesis process, combining n-type ZnO nanoflower (3D) with p-type CuO nanoparticles (0D) have fabricated a very interesting p-n heterojunction.[138] In Z-scheme, the electrons from the semiconductor (A) with a lower conduction band combine with holes from a higher valence band semiconductor (B). Liu *et al*.

TH-2636_166122040

displayed the Z-scheme mechanism in the TiO_2/g-C_3N_4 composites, and in the CdS/WO_3, Jin *et al.* shows the presence of the Z-scheme.[139, 140]

1.4.6 Electron/Hole Extraction Layer

The charge extraction layer support hole transfer from the photoanode to oxygen evolution catalysts (OECs) and also enhances holes lifetime on the surface of the photoanode. For instance, as hole-storage layer ferrihydrite was deposited over cubic Ta_3N_5 photoanode, improves the stability of Ta_3N_5 photoanode protecting it against photo-corrosion.[141] The surface of WO_3 nano blocks was modified with hexagonal boron nitride quantum dots, enhancing charge separation and water oxidation.[142] Into the NiOOH/FeOOH layer and $BiVO_4$, carbon quantum dots were introduced, considerably enhancing its PEC water- splitting efficiency.[142] In recent times, van de Krol *et al*. specified the roles of a few OECs, such as RuOx and Co-Pi, from the perspectives of the surface recombination and surface reaction kinetics.[143] The small thermodynamic driving force caused by insufficient hole extraction from the photoanodes, strongly limited the water oxidation capability of OECs.[144] This limitation means that for one of the finest prevailing photoanode, a semiconductor with an OEC ($BiVO_4$/OEC), the band bending at the electrode/electrolyte interface of $BiVO_4$ must be optimized.[144-146] For instance, Kim and Choi demonstrated that, because the hole transport resistance of FeOOH is lower than that of NiOOH, the incorporation of a FeOOH compound can accelerate hole transport from $BiVO_4$ to the NiOOH.[147] Graphene is used as a hole transport layer to improve hole tunnelling efficacy, demonstrated by Qin *et al.* where the role of graphene in $BiVO_4$/TiO_2/Graphene photoanode was studied [148]. Chen *et al.* between the layer Fe_2O_3 and ZnO inserted a $ZnFe_2O_4$ to extract the trapped holes to the surface[149]. The use of black phosphorene was demonstrated by Zhang *et al.* as an efficient hole-extracting layer to increase the water oxidation ability of co-catalyst in $BiVO_4$ based photoanode.[150]

TH-2636_166122040

1.5 MOTIVATION AND OBJECTIVES OF THE PRESENT WORK

Many reports depict the use of semiconducting material in PEC water-splitting, but their water-splitting performances are still far away from their theoretical value. Reasons for the poor performance of the photoelectrode are such as excessive recombination at the interface of photoanode-electrolyte and recombination in bulk. The main advantage of PEC water-splitting is that it requires a lower potential for water-splitting, while the disadvantage of it is that it can't be operational 24X7. Electrochemical water-splitting is alternate to overcome the drawbacks of PEC, where catalysts are used to show water-splitting in absence of the Sun. Several reports show efficient OER performance using noble metal oxides, but their poor stability and high cost, make researchers think of alternate electrocatalysts. These key shortcomings of metal oxide-based photocatalyst and electrocatalyst must be addressed to further enhance their water-splitting performance. The objectives of the present thesis work are as follows:

(1) Fabrication and design of electrodes that have distinctive combinations of properties appropriate for HER and OER activity.

(2) Designing various morphologies of the semiconducting material for better (photo)electrochemical performance.

(3) Applying different approaches such as material doping, co-catalyst modification, heterojunctions formation, doping, and electron/hole extraction layer, for stable and efficient catalyst.

(4) Using noble metal-free catalyst, and green synthetic route for their synthesis to show HER and OER activity.

(5) Understanding of (photo)electrochemical water-splitting mechanism in the fabricated electrode.

TH-2636_166122040

(6) Using new, simple, and cost-effective fabrication techniques to get efficient electrodes for HER and OER performance.

Based on the above objectives semiconductor metal oxides such as $CuBi_2O_4$ and $BiVO_4$ are suitable for PEC water-splitting, due to their appropriate band positions, abundantly available, and stability neutral conditions. While $MnCo_2O_4$, with high stability in harsh alkaline conditions, their ample amount and higher intrinsic conductivity, makes it a promising material for electrochemical water-splitting.

1.6 REFERENCES

1. M. A. M. Hasan, Y. Wang, C. R. Bowen, Y. Yang, *Nano-Micro Lett.*, 2021, **13**, 82.
2. E. V. Schneidemesser, P. S. Monks, *Environ. Sci.: Processes Impacts*, 2013, **15**, 1315.
3. United Nations Framework Convention on Climate Change, *Adoption of the Paris Agreement*, 21st Conference of the Parties, Paris, 2015.
4. United Nations Framework Convention on Climate Change, *Kyoto Protocol Reference Manual On Accounting Of Emissions And Assigned Amount*, 2008.
5. European Environment Agency (EEA), *https://www.eea.europa.eu*
6. EIA, International Energy Outlook, 2019, U.S. Energy Information Administration (EIA), 2019, https://www.eia.gov/outlooks/ieo/pdf/ieo2019.pdf (accessed March 2021).
7. R. J. Detz, J. N. H. Reek and B. C. C. Van Der Zwaan, *Energy Environ. Sci.*, 2018, **11**, 1653.
8. R. Lindsey, *Climate Change: Atmospheric Carbon Dioxide*, August 2020.
9. N. L. Panwar, S. C. Kaushik and S. Kothari, *Renewable Sustainable Energy Rev.*, 2011, **15**, 1513.
10. S. Yun, Y. Qin, A. R. Uhl, N. Vlachopoulos, M. Yin, D. D. Li, X. Han and A. Hagfeldt, *Energy Environ. Sci.*, 2018, **11**, 476.

TH-2636_166122040

11. L. Xiao, S. Y. Wu and Y. R. Li, *Renewable Energy,* 2012, **41**, 1.

12. A. Thakur, P. Kumar, S. M. Thalluri, R. K. Sinha, P. Devi, *Int. J. Hydrogen Energy*, 2021, **46**, 8444.

13. S. S. Lam, V. Nguyen, M. T. N. Dinh, D. Q. Khieu, D. D. La, H. T. Nguyen, D. V. N. Vo, R. S. Varma, M. Shokouhimehr, C. C. Nguyen, Q. V. Le and W. Peng. *J. Mater. Chem. A,* 2020, **8**, 10571.

14. P. Nikolaidis and A. Poullikkas, Renew. *Sust. Energ. Rev.*, 2017, **67**, 597.

15. F. Dalena, A. Senatore, M. Basile, S. Knani, A. Basile and A. Iulianelli, *Membranes*, 2018, **8**, 98.

16. C. Jiang, S. J. Moniz, A. Wang, T. Zhang and J. Tang, *Chem. Soc. Rev.*, 2017, **46**, 4645.

17. K. Sekizawa, K. Oh-ishi and T. Morikawa, *Dalton Trans.*, 2020, **49**, 659.

18. Baxter, Z. Bian, G. Chen, D. Danielson, M. S. Dresselhaus, A. G. Fedorov, T. S. Fisher, C. W. Jones, E. Maginn, U. Kortshagen, A. Manthiram, A. Nozik, D. Rolison, T. Sands, L. Shi, D. Sholl and Y. Wu, *Energy Environ. Sci.*, 2009, **2**, 559.

19. C. Ros, T. Andreu and J. R. Morante, *J. Mater. Chem. A*, 2020, **8**, 10625.

20. M. Bhatt and J. Lee, *J. Mater. Chem. A,* 2015, **3**, 10632.

21. H. M. Chen, C. K. Chen, R.-S. Liu, L. Zhang, J. Zhang and D. P. Wilkinson, *Chem. Soc. Rev.*, 2012, **41**, 5654.

22. I. Roger, M. A. Shipman and M. D. Symes, *Nat Rev Chem*, 2017, **1,** 2397.

23. B. Rausch, M. D. Symes, G. Chisholm and L. Cronin, *Science,* 2014, **345**, 1326.

24. C. L. Hu, L. Zhang and J. L. Gong, *Energy Environ. Sci.*, 2019, **12**, 2620.

25. J. R. Bolton, S. J. Strickler and J. S. Connolly, *Nature,* 1985, **316**, 495.

26. S. Chen, D. Huang, P. Xu, W. Xue, L. Lei, M. Cheng, R. Wang, X. Liu and R. Deng, *J. Mater. Chem. A,* 2020, **8**, 2286.

TH-2636_166122040

27. X. Peng, C. Pi, X. Zhang, S. Li, K. Huo and P. K. Chu, *Sustain. Energy Fuels*, 2019, **3**, 366.

28. A. Wolcott, W. A. Smith, T. R. Kuykendall, Y. Zhao and J. Z. Zhang, *Small*, 2009, **5**, 104.

29. M. G. Walter, E. L. Warren, J. R. McKone, S. W. Boettcher, Q. Mi, E. A. Santori and N. S. Lewis, *Chem. Rev.*, 2010, **110**, 6446.

30. K. Sivula, F. Le Formal and M. Gr¨atzel, *ChemSusChem*, 2011, **4**, 432.

31. A. G. Tamirat, J. Rick, A. A. Dubale, W.-N. Su and B.-J. Hwang, *Nanoscale Horizons*, 2016, **1**, 243.

32. B. Y. Alfaifi, H. Ullah, S. Alfaifi, A. A. Tahir and T. K. Mallick, *Veruscript Funct. Nanomater.*, 2018, **2**, BDJOC3.

33. J. R. Swierk and T. E. Mallouk, *Chem. Soc. Rev.*, 2013, **42**, 2357.

34. R. Liu, Z. Zheng, J. Spurgeon and X. Yang, *Energy Environ. Sci.*, 2014, **7**, 2504.

35. J. W. Ager, M. R. Shaner, K. A. Walczak, I. D. Sharp and S. Ardo, *Energy Environ. Sci.*, 2015, **8**, 2811.

36. M. E. G. Lyons and S. Floquet, *Phys. Chem. Chem. Phys.*, 2011, **13**, 5314.

37. W. Yang, R. R. Prabhakar, J. Tan, S. D. Tilley and J. Moon, *Chem. Soc. Rev.*, 2019, **48**, 4979.

38. E. Hu, Y. Yao, Y. Cui and G. Qian, *Materials Today Nano*, 2021, **15**, 100124.

39. T. Hisatomi, J. Kubota and K. Domen, *Chem. Soc. Rev.*, 2014, **43**, 7520.

40. L. Li, P. Wang, Q. Shao and X. Huang, *Chem. Soc. Rev.*, 2020, **49**, 3072.

41. J. Lv, P. Liu, F. Yang, L. Xing, D. Wang, X. Chen, H. Gao, X. Huang, Y. Lu and G. Wang, *ACS Appl. Mater. Interfaces*, 2020, **12**, 48495.

42. W. Sheng, B. Sun, T. Shi, X. Tan, Z. Peng and G. Liao, *ACS Nano*, 2014, **8**, 7163.

43. A. K. Shah, T. K. Sahu, D. Gogoi, N. R. Peela and M. Qureshi, *J. Power Sources*, 2020, **477**, 229024.

TH-2636_166122040

44. A. K. Shah, D. Gogoi, N. R. Peela and M. Qureshi, *Chem. Commun.*, 2021, **57**, 8027.

45. S. J. Hong, S. Lee, J. S. Jang and J. S. Lee, *Energy Environ. Sci.*, 2011, **4**, 1781.

46. D. Zhang, Y. Cao, S. K. Karuturi, M. Du, M. Liu, C. Xue, R. Chen, P. Wang, J. Zhang, J. Shi, *ACS Appl. Energy Mater.*, 2020, **3**, 4629.

47. S. Chen, J. Li, J. Bai, L. Xia, Y. Zhang, L. Li, Q. Xu and B. Zhou, *Appl. Catal. B*, 2018, **237**, 175.

48. Z. Kang, H. Si, S. Zhang, J. Wu, Y. Sun, Q. Liao, Z. Zhang and Y. Zhang, *Adv. Funct. Mater.*, 2019, **29**, 1808032.

49. H. L. Wu, X. B. Li, C. H. Tung and L. Z. Wu, *Adv. Sci.*, 2018, **5**, 1700684.

50. P. Salvador, *J. Phys. Chem. B*, 2001, **105**, 6128.

51. I. Robel, M. Kuno, P. V. Kamat, *J. Am. Chem. Soc.*, 2007, **129**, 4136.

52. J. Duan, H. Zhang, Q. Tang, B. He, L. Yu, *J. Mater. Chem. A*, 2015, ***3***, 17497.

53. C. Lelii, M. G. Bawendi, P. Biagini, P.-Y. Chen, M. Crucianelli, J. M. D'Arcy, F. De Angelis, P. T. Hammond, R. Po, *J. Mater. Chem. A*, 2014, **2**, 18375.

54. I. Mora-Seró, S. Giménez, F. Fabregat-Santiago, R. Gómez, Q. Shen, T. Toyoda, J. Bisquert, *Acc. Chem. Res.*, 2009, **42**, 1848.

55. G. Wang, X. Yang, F. Qian, J. Z. Zhang, Y. Li, *Nano Lett.*, 2010, **10**, 1088.

56. I. Cesar, K. Sivula, A. Kay, R. Zboril, M. Grätzel, *J. Phys. Chem. C*, 2009, **113**, 772.

57. C. He, X. Wu, J. Shen, P. K. Chu, *Nano Lett.*, 2012, **12**, 1545.

58. C. Liu, J. Sun, J. Tang, P. Yang, *Nano Lett.*, 2012, **12**, 5407.

59. J. Jasieniak, M. Califano, S. E. Watkins, *ACS Nano*, 2011, **5**, 5888.

60. J. A. Turner, J. Manassen, A. J. Nozik, *ACS Symp. Ser.*, 1981, **146**, 253.

61. A. R. Kirmani, G. H. Carey, M. Abdelsamie, B. Yan, D. Cha, L. R. Rollny, X. Cui, E. H. Sargent, A. Amassian, *Adv. Mater.*, 2014, **26**, 4717.

TH-2636_166122040

62. Y. Hou, A. B. Laursen, J. Zhang, G. Zhang, Y. Zhu, X. Wang, S. Dahl, I. Chorkendorff, *Angew. Chem., Int. Ed.,* 2013, **52**, 3621.

63. J. He, H. Lindström, A. Hagfeldt, S.-E. Lindquist, *Sol. Energy Mater. Sol. Cells*, 2000, **62**, 265.

64. B. Seger, A. B. Laursen, P. C. Vesborg, T. Pedersen, O. Hansen, S. Dahl, I. Chorkendorff, *Angew. Chem. Int. Ed.,* 2012, **51**, 9128.

65. C. G. Morales-Guio, S. D. Tilley, H. Vrubel, M. Gratzel, X. Hu, *Nat. Commun.,* 2014, **5**, 3059.

66. T. Kothe, N. Plumere, A. Badura, M. M. Nowaczyk, D. A. Guschin, M. Rogner, W. Schuhmann, *Angew. Chem. Int. Ed.,* 2013, **52**, 14233.

67. U. Sim, T. Y. Yang, J. Moon, J. An, J. Hwang, J. H. Seo, J. Lee, K. Y. Kim, J. Lee, S. Han, B. H. Hong, K. T. Nam, *Energy Environ.Sci.,* 2013, **6**, 3658.

68. J. Cirone, S. R. Ahmed, P. C. Wood and A. Chen, *J. Phys. Chem., C* 2019, **123**, 9183.

69. R. Prasannachandran, T. V. Vineesh, A. Anil, B. Murali Krishna and M. M. Shaijumon, *ACS Nano,* 2018, **12**, 11511.

70. H. Miaoyan, B. Juncao, X. Wei, H. Chao and Z. Ruiqin, *J. Mater. Chem. A,* 2018, **6**, 3602.

71. M. N. Shaddad, P. Arunachalam, J. Labis, M. Hezam and A. M. Al-Mayouf, *Appl. Catal. B*, 2019, **244**, 863.

72. S. Qin, M.-L. Sebasti´an, T. Pengyi, F. Cristina, R. M. Joan, B. Zhaoyong, W. Hui and A. Teresa, *ACS Catal.,* 2018, **8**, 3331.

73. L. Han, S. Dong and E. Wang, *Adv. Mater.,* 2016, **28**, 9266.

74. N. Serpone and A. V. Emeline, *J. Phys. Chem. Lett.,* 2012, **3**, 673.

75. D. Mocatta, G. Cohen, J. Schattner, O. Millo, E. Rabani and U. Banin, *Science,* 2011, **332**, 77.

76. Y. C. Cao, *Science,* 2011, **332**, 48.

TH-2636_166122040

77. X. Yang, A. Wolcott, G. Wang, A. Sobo, R. C. Fitzmorris, F. Qian, J. Z. Zhang and Y. Li, *Nano Lett.*, 2009, **9**, 2331.

78. X. Yang, A. J. Fernandez-Carrion, J. Wang, F. Porcher, F. Fayon, M. Allix and X. Kuang, *Nat. Commun.*, 2018, **9**, 4484.

79. Q. G. Pan, K. R. Yang, G. L. Wang, D. D. Li, J. Sun, B. Yang, Z. Q. Zou, W. B. Hu, K. Wen and H. Yang, *Chem. Eng. J.*, 2019, **372**, 399.

80. Q. Yang, J. Du, J. Li, Y. Wu, Y. Zhou, Y. Yang, D. Yang and H. He, *ACS Appl. Mater. Interfaces*, 2020, **12**, 11625.

81. C. Chen, L. Miao and J. J. Jiang, *Nano Energy*, 2018, **53**, 144.

82. K. Ding, B. Chen, Z. Fang, Y. Zhang and Z. Chen, *Phys. Chem. Chem. Phys.*, 2014, **16**, 13465.

83. X. Zhang, B. Zhang, Z. Zuo, M. Wang and Y. Shen, *J. Mater.Chem. A*, 2015, **3**, 10020.

84. W. J. Jo, H. J. Kang, K.-J. Kong, Y. S. Lee, H. Park, Y. Lee, T. Buonassisi, K. K. Gleason and J. S. Lee, *Proc. Natl. Acad.Sci.*, 2015, **112**, 13774.

85. J. Xie, J. Zhang, S. Li, F. Grote, X. Zhang, H. Zhang, R. Wang, Y. Lei, B. Pan and Y. Xie, *J. Am. Chem. Soc.*, 2013, **135**, 17881.

86. 43 K. Sun, L. Zeng, S. Liu, L. Zhao, H. Zhu, J. Zhao, Z. Liu,D. Cao, Y. Hou, Y. Liu, Y. Pan and C. Liu, *Nano Energy*, 2019, **58,** 862.

87. Y. Liu, Y. Ying, L. Fei, Y. Liu, Q. Hu, G. Zhang, S. Y. Pang, W. Lu, C. L. Mak, X. Luo, L. Zhou, M. Wei and H. Huang, *J. Am. Chem. Soc.*, 2019, **141**, 8136.

88. Z. Mo, H. Xu, Z. Chen, X. She, Y. Song, J. Lian, X. Zhu, P. Yan, Y. Lei, S. Yuan and H. Li, *Appl. Catal. B*, 2019, **241**, 452.

89. Z. Mo, H. Xu, Z. Chen, X. She, Y. Song, J. Lian, X. Zhu, P. Yan, Y. Lei, S. Yuan and H. Li, *Appl. Catal. B*, 2019, **241**, 452.

TH-2636_166122040

90. X. Ren, A. Sangle, S. Zhang, S. Yuan, Y. Zhao, L. Shi, R. L. Z. Hoye, S. Cho, D. Li, J. L. MacManus-Driscoll, *J. Mater. Chem. A*, 2016, **4** 10203.

91. L. G. Li, P. T. Wang, Q. Shao and X. Q. Huang, *Chem. Soc. Rev.*, 2020, **49**, 3072.

92. Y. Fu, C. L. Dong, Z. Zhou, W. Y. Lee, J. Chen, P. Guo, L. Zhao and S. Shen, *Phys. Chem. Chem. Phys.*, 2016, **18**, 3846.

93. M. T. Mayer, C. Du and D. Wang, *J. Am. Chem. Soc.*, 2012, **134**, 12406.

94. M. Marelli, A. Naldoni, A. Minguzzi, M. Allieta, T. Virgili, G. Scavia, S. Recchia, R. Psaro and V. D. Santo, *ACS Appl. Mater. Interfaces*, 2014, **6**, 11997.

95. M. Marelli, A. Naldoni, A. Minguzzi, M. Allieta, T. Virgili, G. Scavia, S. Recchia, R. Psaro and V. D. Santo, *ACS Appl. Mater. Interfaces*, 2014, **6**, 11997.

96. Y. Hou, Z. Wen, S. Cui, X. Guo and J. Chen, *Adv. Mater.*, 2013, **25**, 6291.

97. Y. Liu, L. Liang, C. Xiao, X. Hua, Z. Li, B. Pan and Y. Xie, *Adv. Energy Mater.*, 2016, **6**, 1600437.

98. X. Feng, Y. Chen, Z. Qin, M. Wang and L. Guo, *ACS Appl. Mater. Interfaces*, 2016, **8**, 18089.

99. J. R. McKone, E. L. Warren, M. J. Bierman, S. W. Boettcher, B. S. Brunschwig, N. S. Lewis and H. B. Gray, *Energy Environ. Sci.*, 2011, **4**, 3573.

100. L. Liu, J. Wang, Y. Hou, J. Chen, H. K. Liu, J. Wang and Y. Wu, *Small*, 2016, **12**, 602.

101. J. Zhou, L. Yu, Q. Zhu, C. Huang and Y. Yu, *J. Mater. Chem. A*, 2019, **7**, 18118.

102. K. Keis, C. Bauer, G. Boschloo, A. Hagfeldt, K. Westermark, H. Rensmo, H. Siegbahn, *J. Photochem. Photobiol. A*, 2002, **148**, 57.

103. M. Law, L. E. Greene, J. C. Johnson, R. Saykally, P. D. Yang, *Nat. Mater.*, 2005, **4**, 455.

104. Y. Kuang, G. Feng, P. Li, Y. Bi, Y. Li and X. Sun, *Angew. Chem., Int. Ed.*, 2016, **55**, 693.

TH-2636_166122040

105. Z. Zhuang, Y. Wang, C.Q Xu, S. Liu, C. Chen, Q. Peng, Z. Zhuang, H. Xiao, Y. Pan, S. Lu, R. Yu, W. C. Cheong, X. Cao, K. Wu, K. Sun, Y. Wang, D. Wang, J. Li and Y. Li. *Nature Communications*, 2019, **10**, 4875.

106. J. Li, Y. Qiu, Z. Wei, Q. Lin, Q. Zhang, K. Yan, H. Chen, S. Xiao, Z. Fan and S. Yang, *Energy Environ. Sci.*, 2014, **7**, 3651

107. B. W. Zhang, C. J. Li, G. Yang, K. Huang, J. S. Wu, Z. Li, X. Cao, D. D. Peng, S. J. Hao and Y. Z. Huang, *ACS Appl. Mater. Interfaces*, 2018, **10**, 23807.

108. J. Yang, D. Wang, H. Han and C. Li, *Acc. Chem. Res.* 2013, **46**, 1900.

109. L. Badia-Bou, E. Mas-Marza, P. Rodenas, E. M. Barea, F. Fabregat-Santiago, S. Gimenez, E. Peris and J. Bisquert, *J. Phys. Chem., C* 2013, **117**, 3826.

110. S. D. Tilley, M. Cornuz, K. Sivula and M. Gra¨tzel, *Angew. Chem. Int. Ed.*, 2010, **49**, 6405.

111. F. Lin, D. Wang, Z. Jiang, Y. Ma, J. Li, R. Li and C. Li, *Energy Environ. Sci.*, 2012, **5**, 6400.

112. Y. Surendranath, M. W. Kanan and D. G. Nocera, *J. Am. Chem. Soc.* 2010, **132**, 16501.

113. M. W. Kanan, J. Yano, Y. Surendranath, M. Dinca˘, V. K. Yachandra and D. G. Nocera, *J. Am. Chem. Soc.*, 2010, **132**, 13692.

114. J. G. McAlpin, Y. Surendranath, M. Dinca˘, T. A. Stich, S. A. Stoian, W. H. Casey, D. G. Nocera and R. D. Britt, *J. Am. Chem. Soc.*, 2010, **132**, 6882.

115. A. Kay, I. Cesar and M. Grätzel, *J. Am. Chem. Soc.*, 2006, **128**, 15714.

116. J. Ran, J. Zhang, J. Yu, M. Jaroniec and S. Z. Qiao, *Chem. Soc. Rev.*, 2014, **43**, 7787.

117. X. Chen, Y. Li, X. Pan, D. Cortie, X. Huang and Z. Yi, *Nat. Commun.*, 2016, **7**, 12273.

118. 105 A. Sathish and R. Viswanath, *Catal. Today*, 2007, **129**, 421.

119. L. Yang, D. Zhong, J. Zhang, Z. Yan, S. Ge, P. Du, J. Jiang, D. Sun, X. Wu, Z. Fan, S. Dayeh and B. Xiang, *ACS Nano*, 2014, **8**, 6979.

TH-2636_166122040

120. H. She, P. Yue, X. Ma, J. Huang, L. Wang and Q. Wang, *Appl. Catal. B,* 2020, **263**, 118280.

121. H. Zhang, W. Tian, Y. Li, H. Sun, M. O. Tade and S. Wang, *J. Mater. Chem. A,* 2018, **6**, 24149.

122. R. Chong, B. Wang, C. Su, D. Li, L. Mao, Z. Chang and L. Zhang, *J. Mater. Chem. A,* 2017, **5**, 8583.

123. J. Guo, X. Yang, S. Bai, X. Xiang, R. Luo, J. He and A. Chen, *J. Colloid Interface Sci.,* 2019, **540**, 9.

124. J. Gan, X. Lu, B. B. Rajeeva, R. Menz, Y. Tong and Y. Zheng, *ChemElectroChem,* 2015, **2**, 1385.

125. B. Gao, T. Wang, X. Fan, H. Gong, P. Li, Y. Feng, X. Huang, J. He and J. Ye, *J. Mater. Chem. A,* 2019, **7**, 278.

126. B. Moss, F. S. Hegner, S. Corby, S. Selim, L. Francas, N. Lopez, S. Gimenez, J. R. Galan-Mascaros and J. R. Durrant, *ACS Energy Lett.,* 2019, **4**, 337.

127. F. Malara, A. Minguzzi, M. Marelli, S. Morandi, R. Psaro, V. Dal Santo and A. Naldoni, *ACS Catal.*, 2015, **5**, 5292.

128. W. Zhang, J. Ma, L. Xiong, H.-Y. Jiang and J. Tang, *ACS Appl. Energy Mater.*, 2020, **3**, 5927.

129. C. H. Liu, Y. Xu, H. Luo, W. C. Wang, Q. Liang and Z. D. Chen, *Chem. Eng. J.* 2019, **363**, 23.

130. Y. P. Xie, Z. B. Yu, G. Liu, X. L. Ma and H. M. Cheng, *Energy Environ. Sci.*, 2014, **7**, 1895.

131. D. P. Kumar, J. H. Choi, S. Hong, D. A. Reddy, S. Lee and T. K. Kim, *ACS Sustainable Chem. Eng.*, 2016, **4**, 7158.

132. J. K. Hyun, S. Zhang and L. J. Lauhon, Annu. *Rev. Mater. Res.*, 2013, **43**, 451.

TH-2636_166122040

133. Y. Z. Chen, C. Y. Zhang, X. J. Zhang, X. M. Ou and X. H. Zhang, *Chem. Commun.*, 2013, **49**, 9200.

134. X. Q. Hao, Z. W. Cui, J. Zhou, Y. C. Wang, Y. Hu, Y. Wang and Z. G. Zou, *Nano Energy*, 2018, **52**, 105.

135. J. X. Low, J. G. Yu, M. Jaroniec, S. Wageh and A. A. Al- Ghamdi, *Adv. Mater.*, 2017, **29**, 1601694.

136. W. W. Shi and N. Chopra, *Nanomater. Energy*, 2013, **2**, 158.

137. S. J. Moniz, S. A. Shevlin, D. J. Martin, Z.-X. Guo and J. Tang, *Energy Environ. Sci.*, 2015, **8**, 731.

138. L. Zhu, H. Li, Z. Liu, P. Xia, Y. Xie, D. Xiong, *J. Phys. Chem. C.* 2018, **122**, 9531.

139. Liu, Y.; Zeng, X.; Hu, X.; Hu, J.; Wang, Z.; Yin, Y.; Sun, C.; Zhang, X. *Catal. Today*, 2019, **335**, 243.

140. Jin, J.; Yu, J.; Guo, D.; Cui, C.; Ho,W. *Small*, 2015, **11**, 5262.

141. K. Zhang, B. Jin, C. Park, Y. Cho, X. Song, X. Shi, S. Zhang, W. Kim, H. Zeng, J. H. Park, J. H. *Nat. Commun.*, 2019, **10**, 2001.

142. M. K. Mohanta, T. K. Sahu, D. Gogoi, N. R. Peela, M. Qureshi, *ACS Appl. Energy Mater.*, 2019, **2**, 7457.

143. K. H. Ye, Z. Gu, Wang, J. S. Xiao, Y. Yuan, Y. Zhu, Y. Zhang, W. Mai, Yang, S. *Energy Environ. Sci.*, 2017, **10**, 772.

144. C. Zachäus, F. F. Abdi, L. M. Peter, & R. van de Krol, *Chem. Sci.*, 2017, **8**, 3712.

145. Pham, T. A., Ping, Y. and Galli, G. *Nat. Mater.*, 2017, **16**, 401.

146. Trześniewski, B. J. *et al*. *Energy Environ. Sci.*, 2017, **10**, 1517.

147. T. Li, J. He, B. Peña, and C. P. Berlinguette, *Angew. Chem. Int. Ed.*, 2016, **128**, 1801.

148. Q. Qin, Q. Cai, W. Hong, C. Jian and W. Liu, *Chem. Eng. J.*, 2020, **402**, 126227.

TH-2636_166122040

149. S. Chen, J. H. Li, J. Bai, L. G. Xia, Y. Zhang, L. S. Li, Q. J. Xu and B. X. Zhou, *Appl. Catal. B,* 2018, **237**, 175.

150. K. Zhang, B. Jin, C. Park, Y. Cho, X. Song, X. Shi, S. Zhang, W. Kim, H. Zeng and J. H. Park, *Nat. Commun.,* 2019, **10**, 2001.

भारतीय प्रौद्योगिकी संस्थान गुवाहाटी • Indian Institute of Technology Guwahati •

TH-2636_166122040

CHAPTER 2

Experimental section

This chapter discusses the comprehensive synthetic protocols of the metal oxides and the co-catalysts, which were employed to show (photo)electrochemical water splitting. It also describes instrumentation techniques used in the characterization of the materials. It displays the complete experimental procedure used in (photo)electrochemical characterization of the catalysts. In this chapter, different performance perimeters for photo and electro catalysts are also discussed in detail.

TH-2636_166122040

2.1 INTRODUCTION

This chapter summarised the synthesis and fabrication protocol for metal oxide-based working electrodes for (photo)electrochemical water-splitting. It also describes basic instrumental techniques which were used in the characterization of the materials. The chemicals and materials which were used during the synthesis and fabrication of the working electrode are also listed in the current chapter. The performance parameters which were used to define the performance of the catalysts are also explained in detail.

2.2 REAGENTS AND MATERIALS USED

Bismuth (III) nitrate pentahydrate (98%) (Sigma Aldrich), Copper (II) nitrate trihydrate (95%) (Himedia), Ethanol (TMEDA), Glacial acetic acid (100-99%) (Merck), MilliQ water (18.2 $M\Omega.cm^{-2}$), Hydrazine hydrate (Loba Chemie), Graphite powder (Loba Chemie), Potassium permanganate (Aldrich), Hydrogen peroxide (Merck), Sodium nitrate (Merck), Sulphuric acid (Merck), Hydrogen chloride (Merck), Ammonium metavanadate (Himedia), Citric acid (Merck), Polyvinyl chloride (Sigma Aldrich), Sodium bicarbonate (Himedia), Indium chloride (Sigma Aldrich), Melamine (Sigma Aldrich), Nitric acid (Merck), Cobalt nitrate (Sigma Aldrich), Manganese nitrate (Sigma Aldrich), Ammonium fluoride (Sigma Aldrich), Urea (Sigma Aldrich), Nickel nitrate (Merck), Sodium dihydrogen orthophosphate (Merck), Boron nitride powder (Sigma Aldrich), Cobalt nitrate hexahydrate (Sigma Aldrich), Manganese nitrate tetrahydrate (Sigma Aldrich), Urea (Sigma Aldrich), Acetone (Finar Limited).

2.3 CHARACTERIZATION OF AS-SYNTHESIZED MATERIALS AND (PHOTO)ELECTROCHEMICAL DEVICES

Various analytical techniques were used to characterize all the synthesized materials and fabricated (photo)electrochemical devices. Instrumental tools used in the present studies are listed below:

TH-2636_166122040

(1) Powder X-ray diffraction (PXRD) analysis were done to determine, the crystalline structure and phase purity of all the materials, using, Bruker D2 PHASER X-ray diffractometer with Cu–K_α X-ray generator (λ = 1.54 Å), Rigaku RINT 2500 TTRAX-III, 18 kW power, with Cu–K_α (λ = 1.54 Å) X-ray source and Rigaku SmartLab using Cu K_α (λ = 1.54 Å) as the source with 9kW power.

(2) Micro-Raman spectroscopy analysis was done to determine different modes of vibration present in the sample, using a laser micro-Raman system (Horiba Jobin Vyon, LabRam HR) with 488 nm and 514 nm laser excitation

(3) JASCO Model V–650 and Shimadzu (UV-2600) diffuse reflectance spectrophotometer was used to perform UV-Visible absorption spectra, where $BaSO_4$ was used as reference.

(4) Perkin Elmer (Spectrum-II) instrument with KBr pellet was used to perform Fourier transformed infrared spectroscopic (FT-IR) studies.

(5) Field emission scanning electron microscopic (FESEM) analysis was done to determine the surface morphology of as-synthesized materials using Zeiss (Gemini) and Zeiss (Sigma) instruments, operating at the voltages of 3 kV–10 kV.

(6) Elemental mapping, morphology, d-spacing value, and selected area electron diffraction (SAED) patterns of the samples were determined through, Field emission transmission electron microscopy (FETEM) using JEOL (JEM-2100F) instrument with an operating voltage of 200 kV.

(7) ZETASIZER Nano series (Malvern), Model Nano-ZS90 was used to determine the Zeta potential (magnitude of the surface charge) of as-synthesized material.

TH-2636_166122040

(8) To determine the valance state, elemental composition, and change in the electronic environment around the elements, X-ray photoelectron spectroscopy (XPS) analysis were carried out using ESCALAB Xi+ (Made: Thermo Fisher Scientific Pvt. Ltd., UK) photoelectron spectrometer with a monochromatized Al-K_α ($h\nu$ = 1486.6 eV) source and Thermo Scientific (NEXA surface analysis with micro-focused, 72 W, 12 kV) with Al-K_α ($h\nu$ = 1486.6 eV) as X-ray source. C 1s spectrum (284.77 eV), as reference was used to compensate for the surface charging effect. XPSPEAK 4.1 software was used to fit and deconvolute the data.

(9) Contact angle measurements were performed using a KRUSS Drop Shape Analyzer-DSA25 instrument with an automatic liquid dispenser at ambient temperature.

(10) CHI1120B electrochemical workstation was used to record electrochemical analysis.

(11) Incident photon to current conversion efficiency (IPCE) of photoelectrodes were measured by Newport ORIEL IQE–200 instrument fitted with a 250 W quartz tungsten halogen lamp. Calibrating tungsten halogen lamp by standard Si and Ge diodes.

(12) Electrochemical work station from CH instruments model CHI760D, Inc., Austin, TX and Gamry Instrument model Interface1010 E was used to perform electrochemical impedance spectroscopic (EIS) analyses of the devices.

(13) The gas evolved (to calculate Faradaic yield) was measured by gas chromatography (GC) (Model-7820A, Agilent Technologies).

TH-2636_166122040

2.4 (PHOTO)ELECTROCHEMICAL MEASUREMENTS

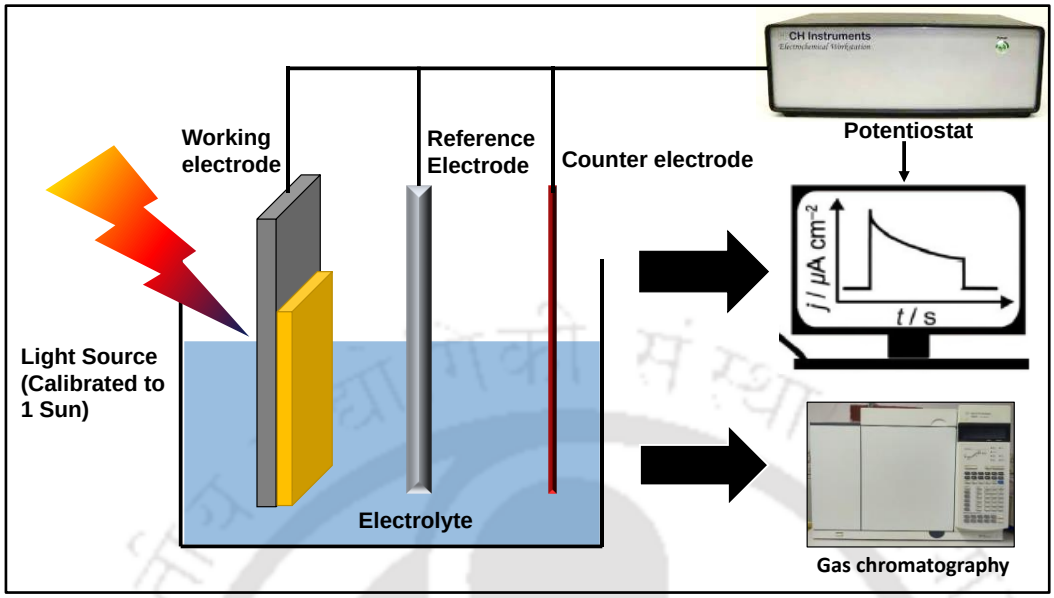

Figure 2.1 Schematic representation showing the experimental setup for (photo)electrochemical water-splitting, where PEC measurements were done in presence of light calibrated to 1 Sun, and the OER process takes place in absence of light, where voltage is applied through potentiostat.

An electrochemical analyser (model-CHI1120B) with a three-electrode system was used to perform (photo)electrochemical measurements. The measurement were done using 0.5 M Na_2SO_4 (pH = 6.8) (**chapter 3 & 4**) and 1 M KOH (pH= 13) (**chapter 5 & 6**) in quartz electrochemical cell (**chapter 3 & 4**) and polypropylene electrochemical cell (**chapter 5 & 6**). To remove any dissolved oxygen present in the electrolyte solution before (photo)electrochemical measurements, the electrolyte solution was purged with nitrogen gas for 30 min. During (photo)electrochemical measurements, Ag/AgCl (**chapter 3, 4 & 5)** and Hg/HgO (**chapter 6**) are used as a reference electrode, as-fabricated electrode used as a working electrode, platinum electrode used as a counter electrode (**chapter 3 &, 4, 5**) and graphitic rod used as a counter electrode (**chapter 6**). Throughout the (photo)electrochemical measurements, working electrodes were covered using araldite polymer, and only the active surface was exposed to the electrolyte for the (photo)electrochemical water-splitting process to

TH-2636_166122040

occur. The 300 W halogen lamp (Osram Sylvania, USA, in **Chapter 3**) and solar simulator (1 Sun, Photo Emission Tech, Inc, Model-300WSS-PC) (**chapter 4**), were used as light source and the intensity light source was adjusted to 100 mW/cm^2. Following **equation (2.1)** was used to convert applied potential from Ag/AgCl into RHE: [1]

$$E_{RHE} = E^{O}_{Ag/AgCl} + 0.059pH + E_{Ag/Agcl} \quad (2.1)$$

E_{RHE} is the potential vs. RHE, $E^{o}_{Ag/AgCl}$ = 0.1976 V at 25 °C, $E_{Ag/AgCl}$ is the potential measured against the Ag/AgCl reference electrode, pH is the pH of electrolyte used. **Equation (2.2)** was used to convert applied potential from Hg/HgO into RHE: [2]

$$E_{RHE} = E^{O}_{Hg/HgO} + 0.059pH + E_{Hg/HgO} \quad (2.2)$$

E_{RHE} is the potential vs. RHE, $E^{O}_{Hg/HgO}$ = 0.098 V at 25 °C, $E_{Hg/HgO}$ is the potential measured against the Hg/HgO reference electrode, pH is the pH of electrolyte used.

Linear sweep voltammetry of the samples was carried out from 0.8 V to 0.0 V vs. RHE at a scan rate of 10 mV s^{-1} (**chapter 3**), from 0.2 V to 1.4 V vs RHE at a scan rate of 10 mV/s (**chapter 4**), 1.0 V to 2.0 V vs RHE, at the scan rate of 1 mV/s (**chapter 5 & 6**). From frequency range 0.1 Hz to 100 kHz, EIS measurements were carried out using an electrochemical work station (Model CHI760D, Inc., Austin, TX). Mott-Schottky plots of each photoelectrode were recorded at a scan rate of 1 kHz under dark conditions scanned from 0.6-2.0 vs. RHE (**chapter 3)** and -0.2 to 1.4 V vs. RHE (**chapter 4**).To determine C_{dl} values and TOF, cyclic voltammetry measurement was done at different scan rates (1-6) mV/sec in the non-faradaic region (0.965 – 1.025 V) vs RHE (**chapter 5 & 6**). **Figure 2.1** shows a schematic representation showing the experimental setup for (photo)electrochemical water-splitting, where PEC measurements were done in presence of light calibrated to 1 Sun and the OER process takes place in absence of light.

2.5 (PHOTO)ELECTROCHEMICAL PERFORMANCE PARAMETERS

The performance of the as-fabricated device for (Photo)electrochemical water-splitting process which determines the goodness of the device are discussed in detail below:

2.5.1 Incident Photon-to-Current Conversion Efficiency (IPCE)

One of the important parameters to assess the performance of a device in PEC water-splitting is, External quantum efficiency (EQE) or Incident photon-to-current conversion efficiency (IPCE). The IPCE is defined as the number of incident photons that are converted to photocurrent by a photoelectrode as a function of wavelength, in general, it determines the light-harvesting efficiency of a photoelectrode. It can be expressed using **equation[3] (2.3)**:

$$\mathrm{IPCE} = 1240 \times \frac{J_{sc}}{\lambda \times P_{mono}(\lambda)} \quad (2.3)$$

Where P_{mono} is the light intensity at each wavelength (λ).

2.5.2 Faradaic Efficiency/Yield

Faradaic yield measurements is one of the most useful method to determine and understand that the gas evolved during the OER and HER process is owing to oxidation and reduction of water respectively, and not due to the probable side reactions/products. Faradaic yield is likely to be the ratio of actual gas (H_2 or O_2) measured experimentally to the amount of gas (H_2 or O_2) calculated theoretically was calculated using **equation (2.4)**[4]

$$Faradaic\ yield = \frac{(amount\ of\ gas\ evolved\ measured\ experimentally)}{(amount\ of\ gas\ \ calculated\ theoretically)} \quad (2.4)$$

The theoretical calculation for the amount of gas evolved was done by using **equation (2.5)**[4]

$$Amount\ of\ gas\ evolved = \frac{(J.t)}{(n.F)} \quad (2.5)$$

TH-2636_166122040

Where J (current density (A/cm^2)), t (time (sec)), n (number of moles charge required to produced one mole of gas, n = 2 for H_2 and n = 4 for O_2) and F (Faraday constant 96485 (C/mol)). The amount of gas that evolved during the water-splitting process was measured through an online gas chromatograph (GC).

2.5.3 Applied Bias Photon-to-Current Efficiency (ABPE)

Applied Bias Photon-to-Current Efficiency (ABPE) is one of the most vital parameters to know the performance of a photoelectrode, under applied bias conditions. As, Solar-to-hydrogen (STH) is defined as chemical energy of the hydrogen produced divided by the solar energy input from sunlight incident on the process, which is only true when applied bias zero between the working electrode and counter electrode during PEC process. So, when an external bias is applied between the electrodes during PEC water-splitting process, the current drawn from the device increases. Thereby under such conditions, ABPE serves as true diagnostics to STH efficiency and presents the correct efficiency of the photoelectrodes under applied external bias conditions. ABPE can be expressed using the **equation (2.6)**[5]

$$\text{ABPE}\ (\%) = \left[\frac{J_{sc}(\text{mA cm}^{-2})\times(1.23-V_b)(V)\times\eta_F}{P_{Total}(\text{mW cm}^{-2})}\right] \quad (2.6)$$

Where P_{Total} is the power input from illumination, J_{SC} is the photocurrent under the applied bias of V_b and η_F is the faradic efficiency.

2.5.4 Tafel Slope

Tafel slope is one of the significant parameters to determine the performance of an electrocatalyst in oxygen evolution reaction (OER). In general, water-splitting requires very high overpotential to get a significant amount of current, so efforts are been made to get higher current density at lower overpotential. Through the Tafel slope value of a catalyst, one can determine its OER kinetic, Tafel slope is expressed by **equation (2.7).**[6]

$$\log(i) = \log(i_o) + \frac{\eta}{b} \quad (2.7)$$

TH-2636_166122040

Current density (i) at corresponding overpotential (η), exchange current density (i_0), and Tafel slope (b). Smaller Tafel slope indicates that with smaller overpotential (η) current density can increase faster and vice-versa.

2.5.5 Turnover Frequency (TOF)

Turnover frequency (TOF) of electrocatalyst is determined to estimate the number of oxygen molecules formed from active sites of the electrocatalyst per unit time, at a given operating potential. Therefore, it can be used in addition to Tafel analysis to obtain more insight into the gas evolution reaction kinetics. The anodic current values were plotted against different scan rates, from the cyclic voltammogram of the catalyst, showing a linear relationship. To determine the TOF of the electrocatalyst for OER activity, the concentration of active sites of the electrocatalysts (mol/cm^2) (N_S) must be quantified first using the **equation (2.8)**[7,8].

$$Slope\left(\frac{J_{anodic}}{Scan\ rate}\right) = n^2F^2AN_S/4RT \quad (2.8)$$

Where n is the number of electrons transferred, T is the absolute temperature and R is the ideal gas constant. Finally, TOF is calculated using the **equation (2.9)** [7,8]

$$TOF = \frac{J \times A}{n \times F \times N_S} \quad (2.9)$$

Herein, J (current density at particular overpotential (A/cm^2)), A (surface area of the electrocatalyst (cm^2)), n (number of electrons transferred to evolve a molecule of O_2), F (Faraday constant (96458 C/mol).

2.6 ELECTROCHEMICAL IMPEDANCE SPECTROSCOPY (EIS) ANALYSIS

In principle, impedance is simply the opposition force to electrical current in a circuit and is measured in the same units as resistance (Ω). As an alternating current (AC) technique, electrochemical impedance spectroscopy (EIS) is capable of distinguishing between resistive and capacitive responses of metal-oxide interfaces based on the frequency dependence of the

TH-2636_166122040

observed current.[9] EIS is one of the universal and powerful modulation techniques and is helpful for further understanding the complex reaction at the electrode surface/interfaces.

2.6.1 Nyquist Plot

Fixed sinusoidal voltage is applied by a potentiostat across a three-electrode cell containing electrolyte solution along with electrode under investigation. EIS experiments are composed of applying a small-amplitude sinusoidal signal to the electrodes at a certain bias and measuring the response of the system to the perturbation. During an EIS experiment, the current density of the electrode is recorded while applying an alternating current signal with different frequencies (usually 0.1 Hz < f < 10^6 Hz) to the system.[10] By EIS characterization, Nyquist plot (real vs. imaginary impedance) can be obtained. In the spectrum, the X-axis is the real impedance (Z', in the unit of Ohms), while the Y-axis represents the imaginary impedance (Z'', in the unit of Ohms). Theoretically, a typical Nyquist plot can be divided into two parts: high-frequency region and low-frequency region, as shown in **Figure 2.2 (a)**. High-frequency region can be observed close to the original point of the plot. In this region, the (photo)electrochemical process is controlled by the rate of charge transfer and the curve exhibits the shape of a semicircle which hints at the existence of an interface. The characteristic semicircle arc arises from the parallel combination of a resistor and capacitor. In the low-frequency region (large impedance, far from the origin), the process is determined by the rate of mass transfer.[11] Sometimes, there is more than one semicircle on the Nyquist plot. It can be ascribed to a multiple-step electron-or charge-transfer process mediated via surface states or reaction intermediates. The shape of the curves could be affected by the intrinsic or electrochemical properties of electrodes, electrolytes, and the conditions of the experiments.

Figure 2.2 (b) shows an equivalent circuit model, where frequency responses were fitted to determine parameters of the Nyquist plot. The simplest equivalent circuit used to model

TH-2636_166122040

metal-oxide interfaces is called a Randles circuit. The parallel combination of charge transfer resistance (R_{ct}) and interfacial capacitance (C_{int}) describes the flow of Faradaic and non-Faradaic current through the interface, respectively. These two elements are represented in parallel to reflect the fact that total current is the sum of Faradaic and non-Faradaic pathways. The R_s term is included in series to account for any and all resistances associated with solution resistance, wires, clips, or other contacts. The simple Randles circuit can be extended to include multiple parallel R||C circuits in series to account for multiple semicircle arcs observed in the Nyquist plot.[9] **Figure 2.2 (b)** considers the inclusion of two parallel R||C circuits.

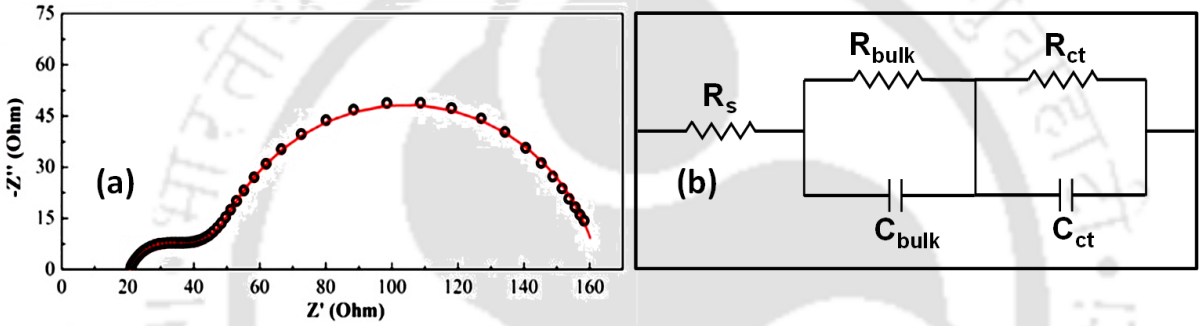

Figure 2.2 (a) A typical Nyquist plot, taken from (Ref. 9), (b) Equivalent circuit used to interpret the EIS data.

2.6.2 Mott-Schottky Plot

Mott−Schottky (M-S) analysis has become widely adopted in many areas to estimate key operational parameters of semiconductor photoelectrodes, namely the flat-band potential (E_F), and the donor concentration (N_d) (for an n-type semiconductor photoanode), or acceptor concentration, (N_a) (for a p-type photocathode).[12] The flat band potential, is the potential at which the electric potential drop between the electrode surface and the bulk is zero. It establishes the position of the semiconductor energy bands with respect to the redox potentials of the electroactive species in the electrolyte. To obtain the value of E_F by M–S measurements, a potentiostat with a three-electrode system, similar to that used for photocurrent measurements, can be used. Then, the M–S equation can be used to obtain the value of E_F after

TH-2636_166122040

obtaining the M–S plots. The flat band (E_F) and carrier density (N_D) of the photoelectrodes can be calculated from the following **formula (2.10):**[13]

$$\frac{1}{C^2} = \frac{2}{A^2 N_D e \varepsilon \varepsilon_0}\left[E - E_{FB} - \frac{kT}{e}\right] \quad (2.10)$$

where C is the capacitance of the semiconductor, A is the surface area of the photoelectrode, N_D is the electron carrier density of semiconductor, e is the fundamental charge constant, ε_0 is the permittivity of the vacuum, ε is the relative permittivity of the semiconductor, E is the applied potential, k is the Boltzmann constant, and T is the temperature. Through the sign of M–S plot slope (negative (p-type) or positive (n-type)), type conductivity in a semiconductor can be determined, shown in **Figure 2.3**.

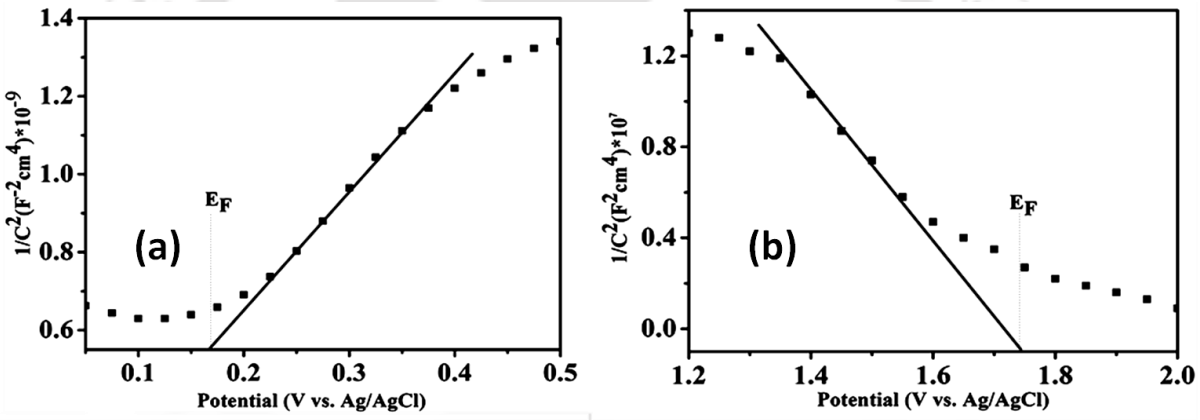

Figure 2.3. Typical Mott-Schottky plot for semiconductor photoanode, showing the nature of conductivity, (a) positive (n-type), (b) negative (p-type). Taken from (Ref. 14).

2.7 REFERENCES

1. S. Hoang, S. W. Guo, N. T. Hahn, A. J. Bard and C. B. Mullins, *Nano Lett.*, 2012, **12**, 26.
2. S. Li, S. Sirisomboonchai, A. Yoshida, X. An, X. Hao, A. Abudula and G. Guan. *J. Mater. Chem. A*, 2018, **6**, 19221.
3. S. Ho-Kimura, S. J. A. Moniz, A. D. Handoko and J. Tang, *J. Mater. Chem. A*, 2014, **2**, 3948.

TH-2636_166122040

4. C. Jiang, S. J. Moniz, A. Wang, T. Zhang and J. Tang, *Chem. Soc. Rev.*, 2017, **46**, 4645.
5. J. H. Kim, D. Hansora, P. Sharma, J.-W. Jang and J. S. Lee, *Chem. Soc. Rev.*, 2019, **48**, 1908.
6. A. Rebekah, E. Ashok Kumar, C. Viswanathan and N. Ponpandian, *Int. J. Hydrogen Energy.*, 2020, **45**, 6391.
7. L. Kumar, M. Chauhan, P. K. Boruah, M. R. Das, S. A. Hashmi and S. Deka, *ACS Appl. Energy Mater.*, 2020, **3**, 6793.
8. X. Zhang, C. Si, X. Guo, R. M. Kong and F. Qu, *J. Mater. Chem. A.*, 2017, **5**, 17211.
9. A. R. C. Bredar, A. L. Chown, A. R. Burton and B. H. Farnum, *ACS Appl. Energy Mater.*, 2020, **3**, 66.
10. K. Sivula, F. Le Formal, M. Gratzel, *ChemSusChem.*, 2011, **4**, 432.
11. A. J. Bard, L. R. Faulkner, J. Leddy and C. G. Zoski, *Electrochemical Methods: Fundamentals and Applications*, Wiley, 1980.
12. A. Hankin, F. Bedoya-Lora, J. Alexander, A. Regoutz and G. Kelsall, *J. Mater. Chem. A*, 2019, **7**, 26162
13. S. P. Berglund, F. F. Abdi, P. Bogdanoff, A. Chemseddine, D. Friedrich and R. van de Krol, *Chem. Mater.*, 2016, **28**, 4231.
14. Y. Feng, C. Liu, J. Chen, H. Che, L. Xiao, W. Gu and W. Shi, *RSC Adv.*, 2016, **6**, 38290.

TH-2636_166122040

CHAPTER 3

RGO-$CuBi_2O_4$ heterojunction as a photocathode for efficient hydrogen evolution reaction

In this chapter, p-type $CuBi_2O_4$ photocathode was fabricated directly over fluorine-doped tin oxide (FTO) through a drop-casting procedure, showing hydrogen evolution reaction (HER) activity. $CuBi_2O_4$ was overlaid with reduced graphene oxide (RGO), and the modified photoelectrode displayed a two-fold higher photocurrent density than its bare counterpart. Herein, different studies on electron lifetime, charge carrier density, and reaction kinetics of the photocathode were conducted to understand the enhancement in the HER performance of $CuBi_2O_4$ when incorporated with the co-catalyst.

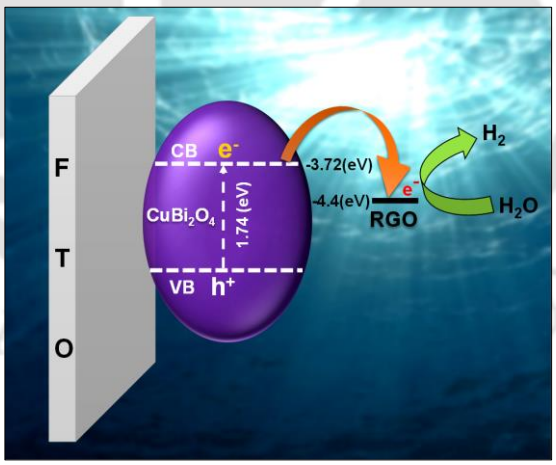

A. K. Shah, et al., **Sustainable Energy Fuels**, 2019, 3, 1554.

TH-2636_166122040

3.1 INTRODUCTION

To use PEC in large-scale hydrogen production, materials must be abundantly available, economically viable, stable, and must have an optimum bandgap to absorb the maximum portion of light present in the solar spectrum. Owing to the above-mentioned properties, p-type semiconducting materials as the core element in PEC has been less studied as compared to widely used n-type semiconducting materials such as ZnO, $BiVO_4$, Fe_2O_3, TiO_2, and WO_3.[1-3] Although, photoelectrochemical water reduction is energetically more favourable as compared to photoelectrochemical water oxidation, finding a suitable material for water reduction is more challenging. The study of p-type semiconductor materials in photoelectrochemical water reduction is limited to Cu_2O, $CuFeO_2$, and $CuGaO_2$.[4,5] However, these materials suffer from the drawback of faster recombination, poor charge separation, very low interfacial charge injection between photocathode and electrolyte interface along with the stability of photocathode. Therefore, finding a suitable p-type photocathode material is very challenging.

Spinel $CuBi_2O_4$, ternary metal oxide, and a p-type semiconductor have a suitable bandgap of around ~ 1.6 eV - 1.8 eV with a maximum predicted theoretical photocurrent density of ~ 19.7 mA/cm^2 .[6,7] Owing to its low bandgap, suitable band positions, positive onset potential, and excellent stability, p-type $CuBi_2O_4$ is considered to be a potential hydrogen-producing material in PEC. However, it suffers from limited charge carrier diffusion length (~ 10-50 nm), very low charge carrier mobility (1.2×10^{-3} $cm^2V^{-1}s^{-1}$), poor charge separation, inefficient interfacial charge injection between $CuBi_2O_4$ and electrolyte, faster recombination of photo-generated excitons prior to photoelectrochemical reduction.[8] Often, efficiency loss is due to the improper Ohmic contact which results in poor charge injection into the collecting electrode. Hence, there is a need to develop a fabrication method, which can enhance Ohmic contact between $CuBi_2O_4$ and transparent conductive substrate to efficiently carry out

 Part of this chapter has been published in **Sustainable Energy Fuels, 2019, 3, 1554**

interfacial charge injection in PEC device. Recent reports show protocols such as electrodeposition, hydrothermal synthesis, drop-casting, spray pyrolysis, and flux-mediated one-pot solution process to improve the yields of photocurrent densities, yet fall short of theoretical photocurrent maxima of $CuBi_2O_4$.[9-13] Among all, *in-situ* growth using drop-casting synthetic procedure is the most efficient and convenient for uniform and stable synthesis of $CuBi_2O_4$ directly over FTO. Drop casting followed by drying and annealing at higher temperature provides good Ohmic contact between $CuBi_2O_4$ and FTO, helping in efficient collection of charges at the interface of FTO and $CuBi_2O_4$. In this procedure, the structure of $CuBi_2O_4$ forms over FTO is through nucleation of $CuBi_2O_4$ nanoparticles, which helps in rapid diffusion of charge carrier towards its surface and increased surface area providing more reaction sites. Apart from reported synthetic protocols, strategies such as heterojunction and co-catalyst modification have been utilized i.e. $AgBr/CuBi_2O_4$, $CuBi_2O_4/BiVO_4$, $CuBi_2O_4/SnO_2$, $CuO/CuBi_2O_4$, $Au/CuBi_2O_4$ to improve the PEC performance.[7,9,14-16] Modifications of $CuBi_2O_4$ discussed above are still not sufficient for efficiently reducing water into hydrogen.

Recent reports show the use of two-dimensional materials such as g- C_3N_4, RGO, MoS_2, etc. as a co-catalyst in photoelectrochemical water-splitting is gaining popularity.[17-19] Two-dimensional materials are known to display remarkable electronic and optical properties along with large specific surface area presenting more number of reaction sites than their bulk counterparts resulting in an enhanced electron-hole pair separation. Among two-dimensional materials, RGO having an sp^2-hybridized carbon atom that acts as an electron sink and electron collector from the surface of semiconducting material is a popular choice for efficient charge separation in a photocatalyst.[20-22] In this report, we have fabricated noble metal-free $CuBi_2O_4$/RGO photocathode by synthesising uniformly distributed $CuBi_2O_4$ directly on FTO through drop-casting procedure and incorporated RGO by spin coating.

TH-2636_166122040

Part of this chapter has been published in **Sustainable Energy Fuels, 2019, 3, 1554**

3.2 EXPERIMENTAL SECTION

3.2.1 Fabrication of $CuBi_2O_4$ Photocathode

Scheme 3.1 displays the step-by-step fabrication procedure of $CuBi_2O_4$ and $CuBi_2O_4$/RGO photocathode. The $CuBi_2O_4$ photocathode was synthesised through a drop-casting procedure where 0.5 mmol of $Bi(NO_3)_3.5H_2O$ in 2.5 ml glacial acetic acid and 0.25 mmol g of $Cu(NO_3)_2.3H_20$ in 10 ml ethanol were stirred in a beaker until they got completely dissolved.[8] After that, individual solutions were mixed together and stirred for 1.5 h to make the precursor solution for $CuBi_2O_4$. 25 µl/cm^2 (FTO area) precursor solution was drop cast onto the surface of FTO and dried in a vacuum oven at 100 ^oC for 1.5 h followed by calcination at 450 ^oC in an ambient atmosphere for 2 h at the ramp rate of 10 ^oC/min.

3.2.2 Synthesis of Reduced Graphene Oxide (RGO)

Graphene Oxide (GO) was synthesized by modified Hummer's method.[22] In a typical synthesis, graphite powder (1 g) and sodium nitrate (0.748 g) were added into concentrated H_2SO_4 (74.8 ml) and kept stirring over 1 h in an ice bath followed by slow addition of $KMnO_4$ (4.5 g). The mixture was kept stirring for another 2 h. The mixture was kept under stirring for 7 days at 35 ^0C. After that, H_2SO_4 (140 ml 5 wt. %) was added to it, and the temperature was raised to 98 ^oC with another 2 h of stirring. The temperature was then brought down to room temperature followed by the addition of H_2O_2 (1.88 ml 48 wt. % aqueous solution) and stirred for 2 h. The precipitate obtained was dissolved in aq. solution of 3 wt. % H_2SO_4/0.5 wt. % H_2O_2 (400 ml) and sonicated for 1 h. The solution mixture was then centrifuged and sonicated to remove impurities and a similar technique was followed with 3 wt. % HCl solution. The obtained product was then dispersed in water and dried in a vacuum oven at 70 ^oC to get GO. Secondly, in a 500 ml RB, GO (200 mg) was sonicated with water (200 ml) until complete dispersion. After which, hydrazine hydrate (1 ml) was added into the solution and heated in an

 Part of this chapter has been published in **Sustainable Energy Fuels, 2019, 3, 1554**

oil bath at 100 °C for 24 h to obtain a black-colored precipitate of RGO. The product was then filtered and washed with methanol and water.

3.2.3 Fabrication of $CuBi_2O_4$/RGO Photocathode

For the synthesis of $CuBi_2O_4$/RGO photocathode, RGO with a concentration of 1.5 mg/ml in DMF was taken and exfoliated by ultra-sonication for 1.5 h, 25 µl/cm^2 (active area) RGO solution was then spin-coated on FTO/$CuBi_2O_4$ surface at 3000 rpm for 30 sec. and the process was repeated again. $CuBi_2O_4$/RGO photoelectrode was heated at 250 °C in an ambient atmosphere for 1 h to finish one complete cycle of RGO deposition over FTO/$CuBi_2O_4$ surface named hereafter $CuBi_2O_4$/RGO-1. Following a similar procedure, other photocathodes with increasing cycles of RGO were fabricated and named $CuBi_2O_4$/RGO-X (X=2-5). After completing the synthesis, all the photocathodes were annealed at 450 °C in an ambient atmosphere for 2 h. The step-by-step fabrication procedure of the photocathode is shown in the figure below.

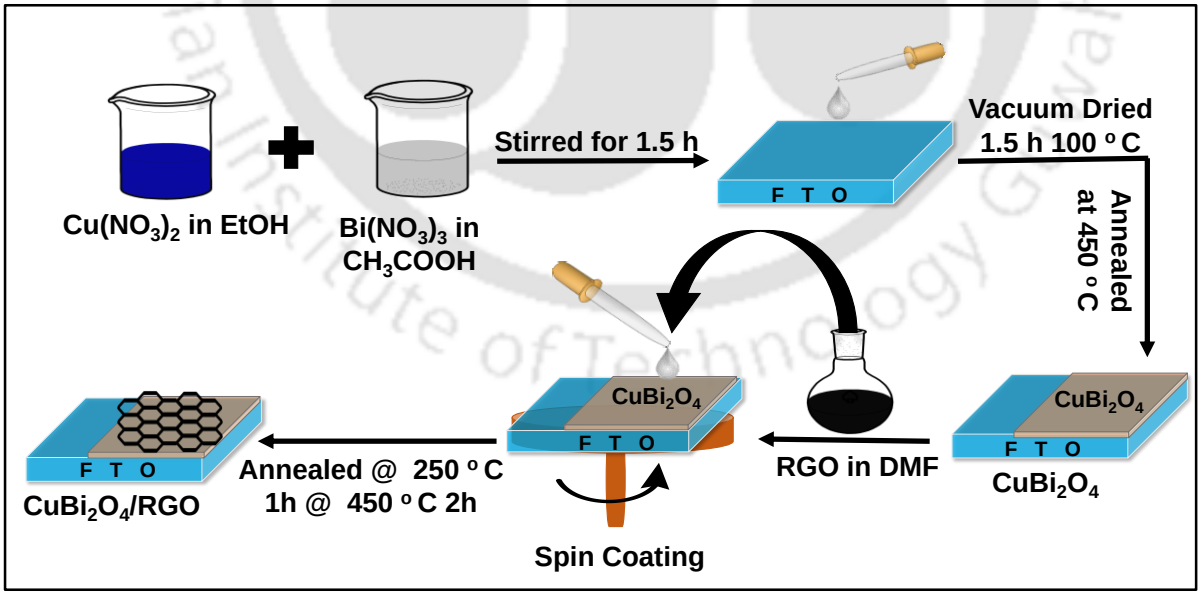

Scheme 3.1. Step-by-step fabrication procedure of $CuBi_2O_4$ and $CuBi_2O_4$/RGO-X (X=2-5) photocathode.

Part of this chapter has been published in **Sustainable Energy Fuels, 2019, 3, 1554**

3.3 RESULTS AND DISCUSSIONS

3.3.1 Powder X-Ray Diffraction (PXRD) Analysis

The crystal structure and phase purity of as-synthesized photocathode materials were determined by powder X-ray diffraction (PXRD) measurements as shown in **Figure 3.1**. **Figure 3.1(a)** shows there is no traceable impurity peak present in the indexed diffractogram, which confirms the formation of the pure tetragonal phase of $CuBi_2O_4$ (JCPDS no. 042-0334). In $CuBi_2O_4$/RGO-4 photocathode, all the corresponding peaks of pristine $CuBi_2O_4$ were present, while peaks corresponding to RGO were absent, which might be due to the amorphous nature of RGO. **Figure 3.1 (b)** shows the PXRD pattern of RGO, the presence of both the planes, (002) and (102) confirms the formation of RGO.[23]

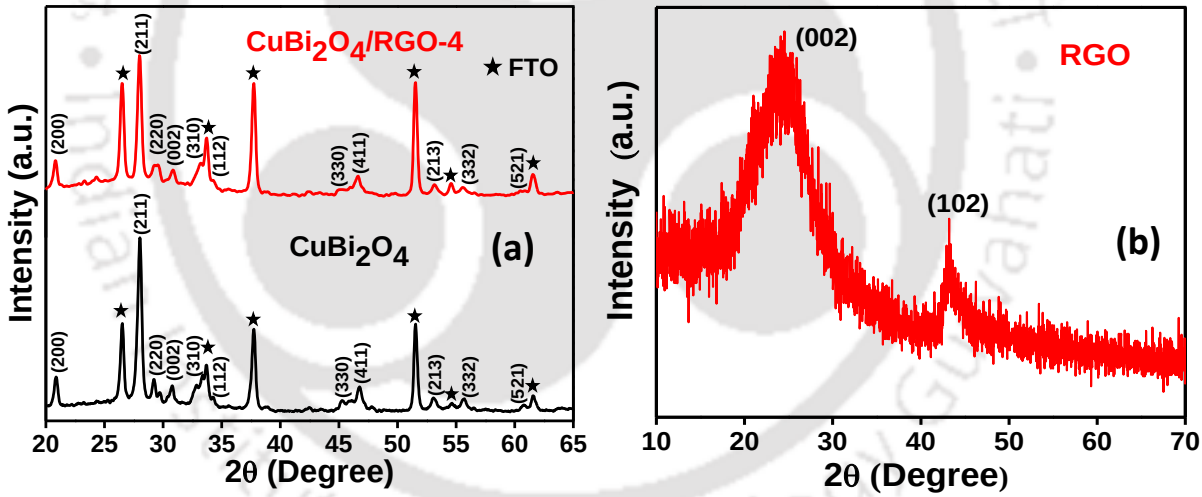

Figure 3.1. Powder X-ray diffraction (PXRD) patterns of (a) $CuBi_2O_4$ and $CuBi_2O_4$/RGO-4, (b) RGO. Perfectly indexed to their crystal planes.

3.3.2 Raman Spectroscopy Analysis

To confirm the formation of composite Raman spectra of pristine $CuBi_2O_4$ and $CuBi_2O_4$/RGO-4 samples were done, shown in **Figure 3.2**.

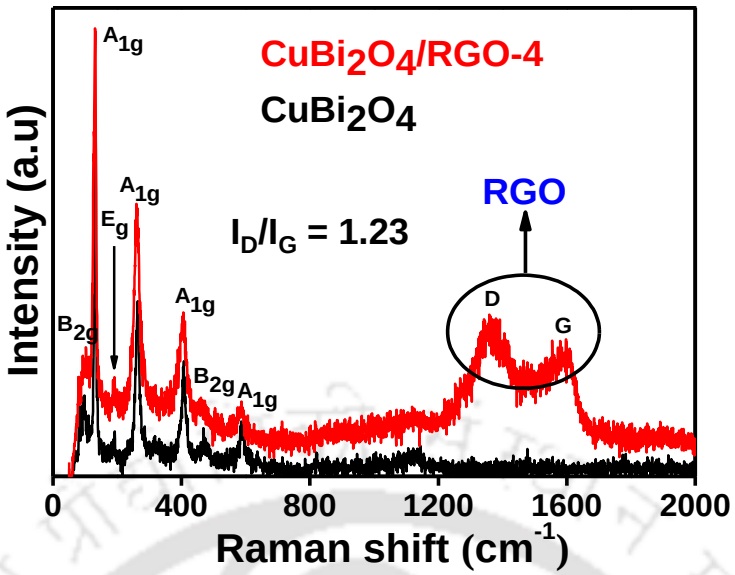

Figure 3.2. Raman Spectra of $CuBi_2O_4$ and $CuBi_2O_4$/RGO-4 photoelectrode. The characteristic D and G band of RGO confirms the presence of RGO in $CuBi_2O_4$/RGO-4.

The peak centred at 92 cm^{-1} corresponds to the B_{2g} in-plane mode of vibration of Bi rhombohedra, whereas, 126 cm^{-1} corresponds to the A_{1g} mode of translational vibration of CuO_4 along the Z-axis. A low intense peak at 185 cm^{-1} indicates the E_g vibrational mode of Cu-Cu. An intense peak at 261 cm^{-1} indicates A_{1g} mode due to opposite rotation of CuO_4 squares and another band at 406 cm^{-1} assigned A_{1g} stretching vibrational mode of Bi-O. The two peaks at 466 cm^{-1} and 588 cm^{-1} represent B_{2g} and A_{1g} bands corresponding to in-plane bond stretching and bond stretching of CuO_4 respectively.[12,24] In the case of $CuBi_2O_4$/RGO-4, characteristic D and G bands for RGO appeared at 1358 cm^{-1} and 1594 cm^{-1}, respectively along with the characteristics bands of $CuBi_2O_4$ confirming the formation of composite.[22]

3.3.3 UV-Visible Spectra Analysis

Figure 3.3 (a) shows the UV-Visible spectra of $CuBi_2O_4$ and $CuBi_2O_4$/RGO-X (X=2-5) photocathode with different numbers of cycles of RGO deposited over $CuBi_2O_4$. It can be seen that the absorbance throughout the visible range gradually increases with the increase in the number of cycles of RGO. The increase in the absorbance is attributed to the presence and

Part of this chapter has been published in **Sustainable Energy Fuels, 2019, 3, 1554**

increase in RGO concentration over the surface of $CuBi_2O_4$. The bandgap of $CuBi_2O_4$ estimated by the Tauc plot was 1.74 (eV), shown in **Figure 3.3 (a)** which is in good agreement with the earlier reports.[6]

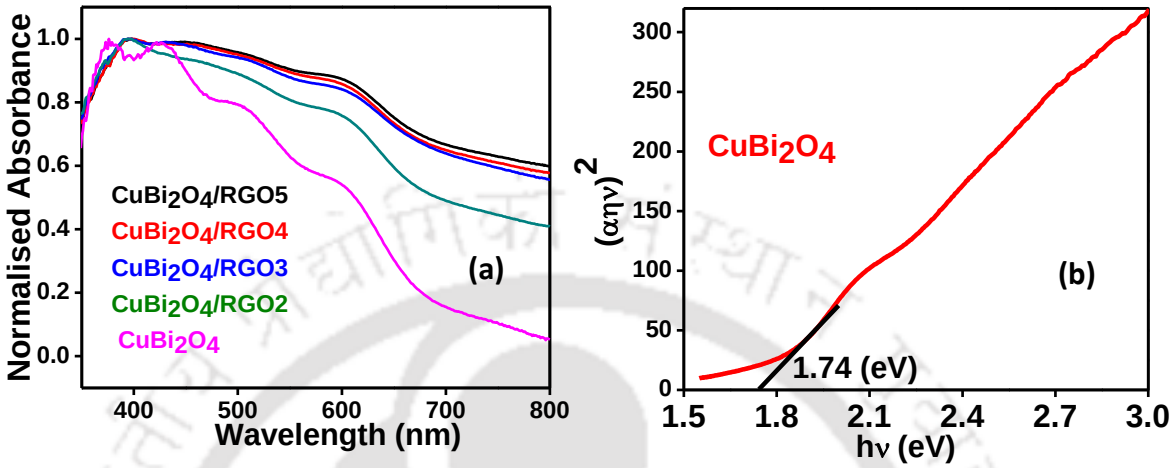

Figure 3.3. (a) UV-Visible diffuse reflectance spectra of $CuBi_2O_4$ and $CuBi_2O_4$/RGO-X photocathodes. (b) Tauc plot shows the estimated bandgap of $CuBi_2O_4$.

3.3.4 Morphological and Structural Analysis

FESEM analysis was carried out in order to know the morphology of $CuBi_2O_4$ and deposition of RGO over it in the modified photocathode, as shown in **Figure 3.4**. The top view FESEM image is shown in **Figure 3.4 (a),** which features homogeneous $CuBi_2O_4$ film over FTO. The FESEM images of $CuBi_2O_4$-RGO-4 (**Figure 3.4 (b)**), depict the homogeneous distribution of reduced graphene oxide on the surface of the $CuBi_2O_4$.

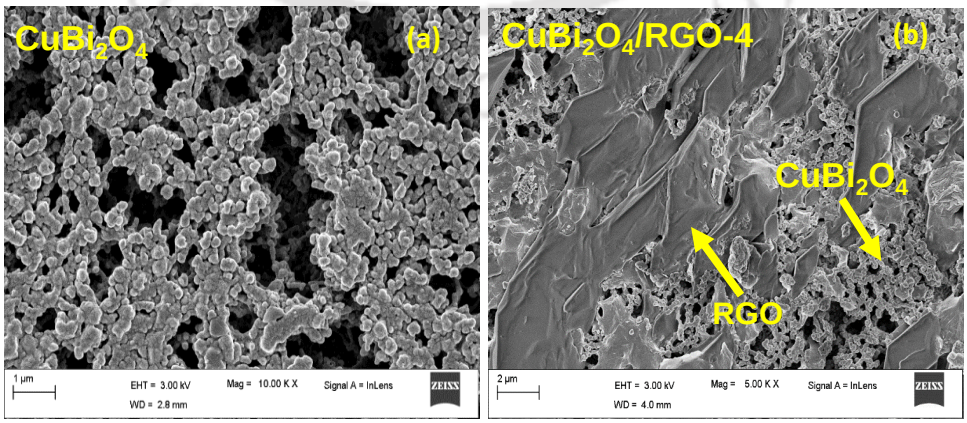

Figure 3.4. Top view FESEM images of uniformly distributed (a) $CuBi_2O_4$, (b) uniform distribution of RGO over $CuBi_2O_4$ in $CuBi_2O_4$/RGO-4.

Figure 3.5 (a) shows the FETEM image of pristine $CuBi_2O_4$ deduced from the films that were studied for PEC evaluation, confirming the formation of $CuBi_2O_4$ structure through nucleation of nanoparticles. As the structure of $CuBi_2O_4$ is formed by a cluster of nanoparticles, it overcomes the poor diffusion length of $CuBi_2O_4$, where, photo excited charge carrier can easily transfer towards the surface without being recombined, improving water reduction efficiency of the photocathode. **Figure 3.5 (b)** shows the HRTEM image of pristine $CuBi_2O_4$. Inset to the **Figure 3.5 (b)** shows, Inverse fast Fourier transformed (IFFT) image displaying the inter-planar d-spacing of 0.36 nm corresponding to (211) lattice plane of $CuBi_2O_4$, indicating the formation of $CuBi_2O_4$.[9] **Figure 3.5 (c)** shows FETEM image of $CuBi_2O_4$/ RGO-4,

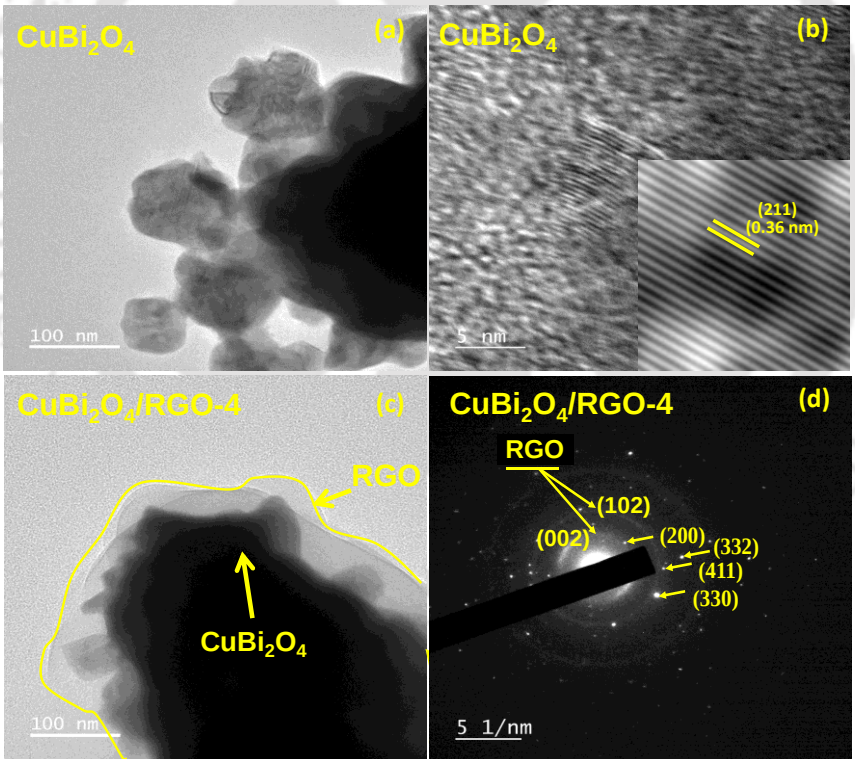

Figure 3.5. (a) FETEM image of $CuBi_2O_4$. (b) HRTEM images of pristine $CuBi_2O_4$. (c) FETEM image of $CuBi_2O_4$/RGO-4. (d) Display Selected Area Electron Diffraction (SAED) pattern of $CuBi_2O_4$/RGO-4.

where RGO is excellently wrapped around $CuBi_2O_4$, showing that there is a very good interfacial contact between RGO and $CuBi_2O_4$.**Figure 3.5 (d)** illustrates the selected area

TH-2636_166122040
Part of this chapter has been published in **Sustainable Energy Fuels, 2019, 3, 1554**

electron diffraction (SAED) pattern of $CuBi_2O_4$/RGO-4, which are assigned to (200), (332), (411), and (330) planes of $CuBi_2O_4$. It supports the Powder X-ray diffraction pattern of $CuBi_2O_4$/RGO-4 confirming purity and crystallinity of $CuBi_2O_4$. Additionally, a characteristic RGO ring was also observed, corresponding to the (002) and (102) crystal plane of RGO sheets confirming the formation of composite.[25, 26]

Figure 3.6 shows the Energy-dispersive X-ray spectroscopy (EDX) mapping of $CuBi_2O_4$/RGO-4. **Figure 3.6** (c-f) indicates the presence of all the elements (Bi, Cu, C, O), and their uniform distribution in the composite.

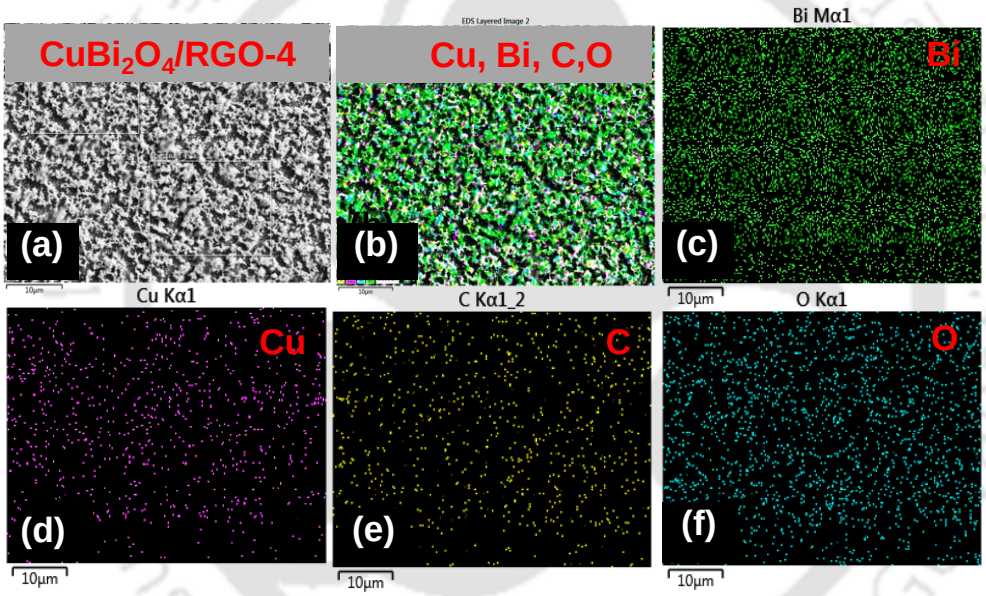

Figure 3.6. FESEM and corresponding Energy-dispersive X-ray spectroscopic (EDX) image of $CuBi_2O_4$/RGO-4, (a, b), Elemental mapping shows uniform distribution of all the elements present in $CuBi_2O_4$/RGO-4 photocathode. (c), (d), (e), (f) Showing uniform distribution of Cu, Bi, C, and O respectively in $CuBi_2O_4$/RGO-4 photocathode.

3.3.5 X-Ray Photoelectron Spectroscopy (XPS) Analysis

To know the elemental composition and chemical state of as prepared $CuBi_2O_4$ and $CuBi_2O_4$/RGO-4 photocathode, XPS analysis was done for both the samples. The presence of corresponding elements was confirmed by XPS survey spectra as shown in **Figure 3.7 (a)**. Bi 4f core-level spectra of $CuBi_2O_4$ and $CuBi_2O_4$/RGO-4 are shown in **Figure 3.7 (b)**. In $CuBi_2O_4$,

the peaks at a binding energy of 158.29 eV and 163.6 eV correspond to $4f_{7/2}$ and $4f_{5/2}$, respectively. In $CuBi_2O_4$/RGO-4, the peaks that appeared at 158.4 eV and 163.7 eV correspond to $4f_{7/2}$ and $4f_{5/2}$, respectively indicates the presence of Bi^{3+} in both the samples. **Figure 3.7 (c)** shows Cu 2p core-level spectra of $CuBi_2O_4$ and $CuBi_2O_4$/RGO-4. Upon deconvolution, Cu 2p peaks of $CuBi_2O_4$ and $CuBi_2O_4$/RGO-4 are fitted into Cu $2p_{3/2}$, Cu $2p_{1/2}$, and three shake-up satellite peaks. The binding energy of 953.43 eV and 940.86 eV in $CuBi_2O_4$, 953.60 eV, and 940.78 eV in $CuBi_2O_4$/RGO-4 correspond to Cu $2p_{1/2}$ and Cu $2p_{3/2}$ respectively.

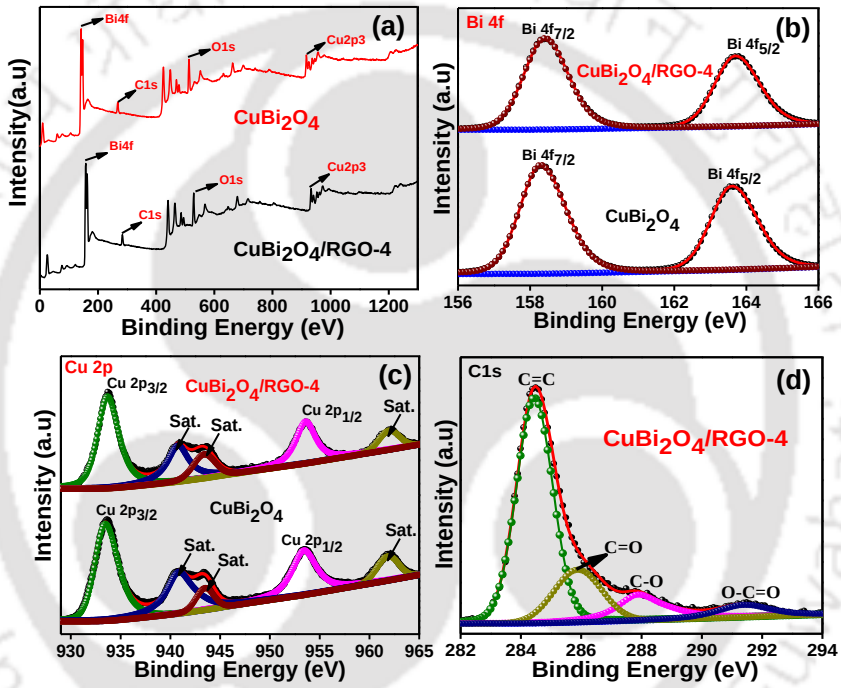

Figure 3.7. XPS (a) Survey spectra. Core-level spectra of (b) Bi 4f, (c) Cu 2p, (d) C1s, showing the presence of Bi^{3+} and Cu^{2+} in $CuBi_2O_4$ and $CuBi_2O_4$/RGO-4.

The presence of Cu $2p_{1/2}$, Cu $2p_{3/2}$, and three shake-up satellite peaks ascertain the presence of Cu^{2+} in both the photocathodes.[27] The asymmetric C1s peak of $CuBi_2O_4$/RGO-4 can be deconvoluted into four peaks shown in **Figure 3.7 (d)**. Peaks at 284.44 eV, 287.89 eV, 285.89 eV, and 291.4 eV, which can be attributed to C=C, C=O, C-O, and O-C=O groups, respectively, confirming the presence of RGO over $CuBi_2O_4$ in the composite.[28]

Part of this chapter has been published in **Sustainable Energy Fuels, 2019, 3, 1554**

In **Figure 3.8 (a, b)**, shift of Bi $4f_{7/2}$ and Cu $2p_{3/2}$ peak in $CuBi_2O_4$/RGO-4 towards higher binding energy as compared to pristine $CuBi_2O_4$, indicates a change in chemical state and/or coordination environment around Bi^{3+} and Cu^{2+} and an indication of good electronic interactions among $CuBi_2O_4$ and RGO interface. Allowing interfacial charge transfer from $CuBi_2O_4$ to RGO through d-π electronic orbital pathway. This shift Bi $4f_{7/2}$ and Cu $2p_{3/2}$ peak to higher binding energy in $CuBi_2O_4$/RGO-4 than pristine $CuBi_2O_4$.[22] In **Figure 3.8 (c)**, de-convolution of the asymmetric O1s XPS core-level spectra of $CuBi_2O_4$ and $CuBi_2O_4$/RGO-4 show peaks at a binding energy of 529.26 eV, 530.75 eV and 529.36 eV, 530.83, 532.33 eV, respectively. The peak at lower binding energy corresponds to lattice oxygen (O_L) in both compounds. The peaks at 530.75 eV and 530.83 are due to oxygen vacancy (O_v) for both samples. An additional peak at 532.33 eV is observed in $CuBi_2O_4$/RGO-4 due to the presence of O−C species suggesting the interaction of RGO with $CuBi_2O_4$.[29]

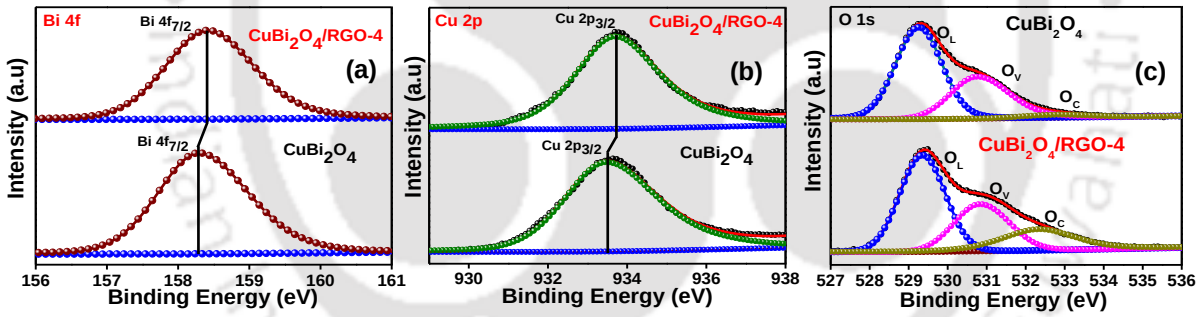

Figure 3.8. XPS core-level spectra of (a) Bi $4f_{7/2}$, (b) Cu $2p_{3/2}$, (c) O 1s, in $CuBi_2O_4$ and $CuBi_2O_4$/RGO-4 photocathode.

3.3.6 Photoelectrochemical Measurements

Figure 3.9 (a) shows linear sweep voltammetry curves for $CuBi_2O_4$ and $CuBi_2O_4$/RGO-X (X = 2-5), where photocurrent measurements were carried under 1 Sun illumination in neutral 0.5 M Na_2SO_4 (pH ~ 6.8) solution. **Figure 3.9 (a)** displays the photocurrent density of pristine $CuBi_2O_4$ to be ~ -0.48 mA/cm^2. Incorporation of RGO over $CuBi_2O_4$ results in a gradual enhancement of photocurrent density and reaches a maximum

value for composition $CuBi_2O_4$/RGO-4, with a value of ~ -0.94 mA/cm^2. Two-fold enhancement in photocurrent density has been achieved for $CuBi_2O_4$/RGO-4 in comparison to pristine $CuBi_2O_4$. There is a gradual increase in current density from $CuBi_2O_4$/RGO-2 to $CuBi_2O_4$/RGO-4 with a sudden drop in current density from $CuBi_2O_4$/RGO-4 to $CuBi_2O_4$/RGO-5, which was due to the possible restacking of RGO, inhibiting penetrations of light into $CuBi_2O_4$. To examine the reusability, $CuBi_2O_4$/RGO-4, and three consecutive linear sweep voltammetry measurements of $CuBi_2O_4$/RGO-4 were carried out, shown in **Figure 3.9 (b)**. The photocurrent density of $CuBi_2O_4$/RGO-4 photocathode in the first two measurements remains constant within the error limits. In the third measurement, we have observed a slight change in the current characteristics, possibly due to the washing and drying of the photocathode leading to some loss of the active material. **Figure 3.9 (c)** shows the photo-response of $CuBi_2O_4$/RGO-4 and $CuBi_2O_4$ photocathode with time, where the light was chopped for ON/OFF on the photocathode at 0 V vs RHE after a 20-second interval. The current densities of the photocathode under illumination are in good agreement with photocathodes in linear sweep voltammetry in **Figure 3.9 (a)**. Upon illumination, the curve of $CuBi_2O_4$/RGO-4 shows constant photocurrent density without any significant decay, whereas $CuBi_2O_4$ shows rapid decay in photocurrent density. Additionally, it was observed that with the incorporation of RGO, there is a substantial increase in the dark current density in the composite. It is well-known fact, that apart from being an effective electron sink, RGO is also known to behave as an electrocatalyst due to its oxygen-containing functional group and catalytic surface active sites for the adsorption of H^+ ions.[30,31] Chronoamperometry measurement has been performed on pristine RGO to evaluate its dark current contribution shown in **Figure 3.9 (d)**.

Part of this chapter has been published in **Sustainable Energy Fuels, 2019, 3, 1554**

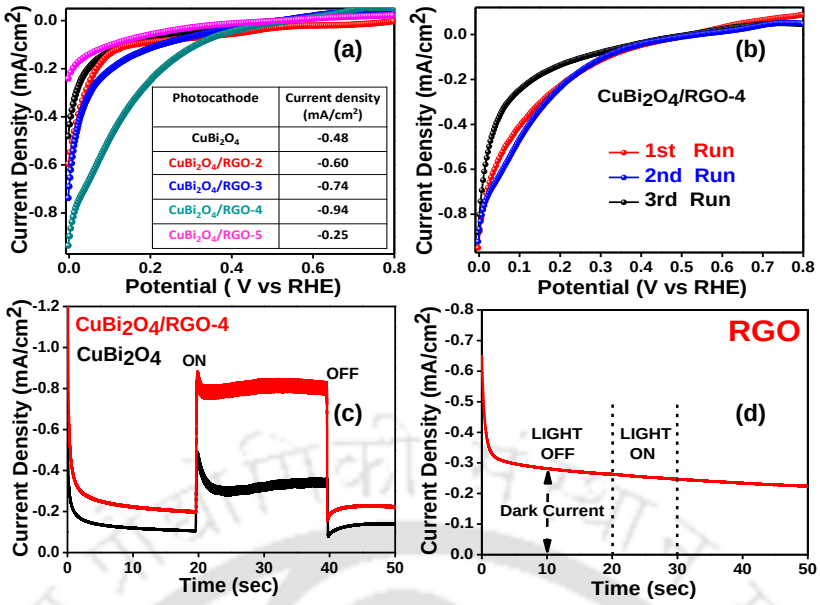

Figure 3.9. (a) Linear sweep voltammetry curves for $CuBi_2O_4$ and $CuBi_2O_4$/RGO-X (X = 2-5). (b) Reusability test for $CuBi_2O_4$/RGO-4. (c) Photocurrent vs. time curve of $CuBi_2O_4$/RGO-4 and $CuBi_2O_4$ photocathode at 0 V vs. RHE with an interval of 20-sec on-off cycles. (d) Chronoamperometry measurement of pristine RGO on FTO at -0.6 V vs Ag/AgCl in neutral 0.5 M Na_2SO_4 (pH ~ 6.8) solution, showing electrochemical behaviour of RGO.

To further verify the improvement in photocurrent density, the IPCE spectra measurement were done, as a function of the wavelength of the incident light, as shown in **Figure 3.10**. It can be seen that $CuBi_2O_4$ modified with RGO showed a substantial increase in IPCE of ~ 64% as compared to pristine $CuBi_2O_4$, which is in good agreement with the J-V curve shown in **Figure 3.9 (a)**. Substantial increase in IPCE value for $CuBi_2O_4$/RGO-4 photocathode can be attributed to the efficient charge separation and charge transfer kinetics by putting RGO over $CuBi_2O_4$.[32, 33] Two dimensional RGO with a very good point of contact with $CuBi_2O_4$ (as can be seen in FETEM analysis) act as a charge sink for collecting electron from $CuBi_2O_4$ and a faster charge transfer owing to high electron mobility as compared to pristine $CuBi_2O_4$ thus reducing the probability of recombination.

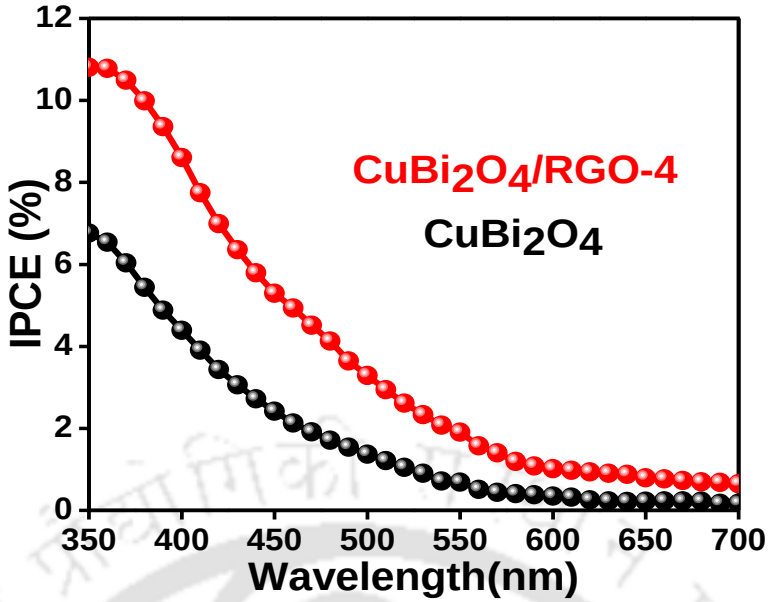

Figure 3.10. Incident Photon-to-Current Conversion Efficiency (IPCE) spectra of $CuBi_2O_4$ and $CuBi_2O_4$/RGO-4.

To gain insights into the electron recombination kinetics of the fabricated PEC devices, transient open-circuit potential (V_{oc}) decay measurements were carried out in 0.5 M Na_2SO_4. V_{oc} is the potential generated at the photoelectrode with respect to the reference electrode when no current was drawn from the circuit. **Figure 3.11 (a)** shows that the photo-voltage generated in $CuBi_2O_4$/RGO-4 is more than the pristine $CuBi_2O_4$, which indicates that there is an increase of charge accumulation at the conduction band of $CuBi_2O_4$/RGO-4 than the pristine $CuBi_2O_4$. Under the open circuit condition, when the light is turned off, the decay in V_{OC} is solely due to the recombination of photo-generated charge carriers. The decay rate of V_{OC} is directly proportional to the rate of recombination. The slower V_{OC} decay furnished by $CuBi_2O_4$/RGO-4 indicates a better charge separation and reduced recombination upon RGO loading. To comprehend the enhanced PEC performance of $CuBi_2O_4$/RGO-4 in comparison to that of $CuBi_2O_4$, the electron lifetime of the two photocathodes was determined through open-circuit potential decay (OCPD) curve in **Figure 3.11 (b)** under the dark conditions using an equation formulated by Zaban.[34-36]

TH-2636_166122040

Part of this chapter has been published in **Sustainable Energy Fuels, 2019, 3, 1554**

$$\tau = -\frac{k_B T}{e} / \left(\frac{dV_{OC}}{dt}\right) \quad (3.1)$$

Where τ is the electron lifetime, k_B is the Boltzmann constant, T is the temperature, e is a charge of an electron. The photoelectron lifetime in $CuBi_2O_4$/RGO-4 is longer than pristine $CuBi_2O_4$. It proves that the addition of RGO over $CuBi_2O_4$ enhances charge separation in $CuBi_2O_4$/RGO-4 photocathode.

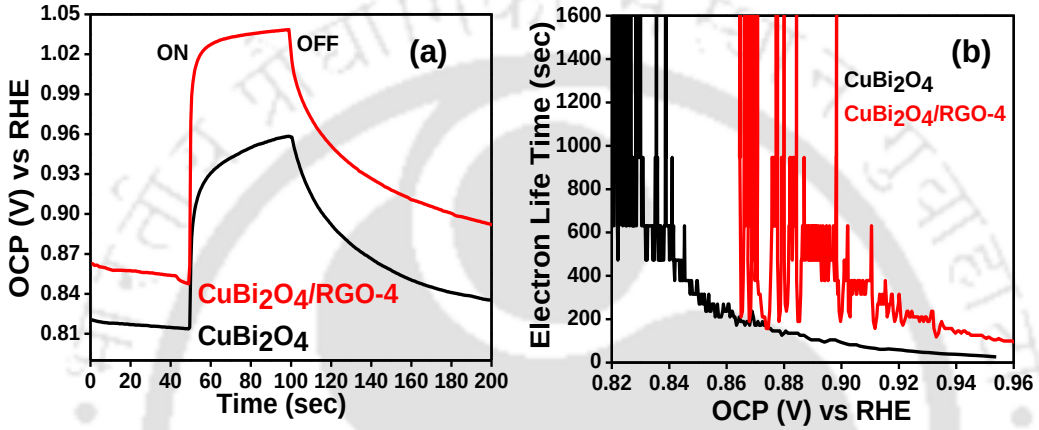

Figure 3.11 (a) Open circuit potential decay curve of $CuBi_2O_4$ and $CuBi_2O_4$/RGO-4. (b) Average Electron lifetime determines from open circuit potential decay.

3.3.7 Electrochemical Impedance Spectroscopy (EIS) Analysis

In order to understand the role of RGO modification over $CuBi_2O_4$, electrochemical impedance measurements were carried out. **Figure 3.12 (a)** shows the Nyquist plot of photocathodes measured at -0.4 V vs Ag/AgCl. The Nyquist plots of both the photocathodes are composed of two semicircles, where the semicircle at the low-frequency region is assigned to the charge transfer resistance at the photocathode/electrolyte interface and the semicircle at the high-frequency region is related to charge transfer resistance inside the bulk.[37-39] Photocathode with smaller diameter of semicircle signifies an efficient charge separation, lower charge transfer resistance as well as the faster interfacial charge transfer kinetics at photocathode/electrolyte. Pristine $CuBi_2O_4$ shows the larger diameter of a semicircle, which

decreases with the introduction of RGO. Incorporating RGO on $CuBi_2O_4$ improves interfacial charge transfer kinetics between photocathode and electrolyte as well as helps in improving the charge separation in $CuBi_2O_4$/RGO-4 photocathode. The Nyquist plot of $CuBi_2O_4$ and $CuBi_2O_4$/RGO-4 photocathode was fitted to an equivalent circuit shown in the inset of **Figure 3.12 (a)**, where R_S is the series resistance; R_{bulk} is the charge transfer resistance inside the bulk of the semiconductor, R_{ct} is charge transfer resistance between photocathode and electrolyte interface. **Table 3.1** shows the fitting values of all the parameters of the equivalent circuit. It can be seen that the R_{bulk} value for $CuBi_2O_4$ significantly decreases from 673.6 **Ω** to 183.7 **Ω**, with the introduction of RGO ($CuBi_2O_4$/RGO-4), indicating an extraction of an electron from $CuBi_2O_4$ to RGO, thereby improving the charge separation efficiency. Decrease in R_{ct} value of $CuBi_2O_4$/RGO-4 as compared to $CuBi_2O_4$, from 4990 **Ω** to 2982 **Ω**, which indicates that there is an enhancement in charge transfer kinetic from $CuBi_2O_4$/RGO-4 photocathode to the electrolyte solution in comparison to pristine $CuBi_2O_4$.

To verify the enhanced charge transportation of $CuBi_2O_4$, upon introduction of RGO, Mott-Schottky analysis was performed. **Figure 3.12 (b)** shows the Mott-Schottky plot for pristine $CuBi_2O_4$ and $CuBi_2O_4$/RGO-4 photocathodes under the dark condition in 0.5 M Na_2SO_4 at an applied frequency of 1 kHz. Negative slopes for both pristine as well as RGO modified photocathode signifies that both $CuBi_2O_4$ and $CuBi_2O_4$/RGO-4 photocathode has p-type conductivity. Charge carrier density of both the photocathodes was obtained from the following formula [6, 40]

$$\frac{1}{C^2} = \frac{2}{A^2 N_D e \varepsilon \varepsilon_0}\left[V - V_{FB} - \frac{kT}{e}\right] \quad (3.2)$$

where C is the capacitance of the semiconductor, A is the area of the photocathode, N_D is the charge carrier density of photocathode, e is the charge of the electron, ε_0 is the permittivity of the vacuum, ε is the dielectric constant of the photocathode (value of ε for $CuBi_2O_4$ is 98)[12], V

Part of this chapter has been published in **Sustainable Energy Fuels, 2019, 3, 1554**

is the applied bias, V_{FB} is the flat-band potential, k is the Boltzmann constant, and T is the temperature. Charge carrier density for $CuBi_2O_4$ and $CuBi_2O_4$/RGO-4 photocathodes were 3.76 x 10^{20} cm^{-3} and 7.92 x 10^{20} cm^{-3} respectively obtained from the slopes of the Mott-Schottky plot. There was a more than two-fold increase in the charge carrier density with the introduction of RGO over $CuBi_2O_4$ as compared to pristine $CuBi_2O_4$ which is in good agreement with the current density of $CuBi_2O_4$ and $CuBi_2O_4$/RGO-4 as shown in **Figure 3.9 (a)**.

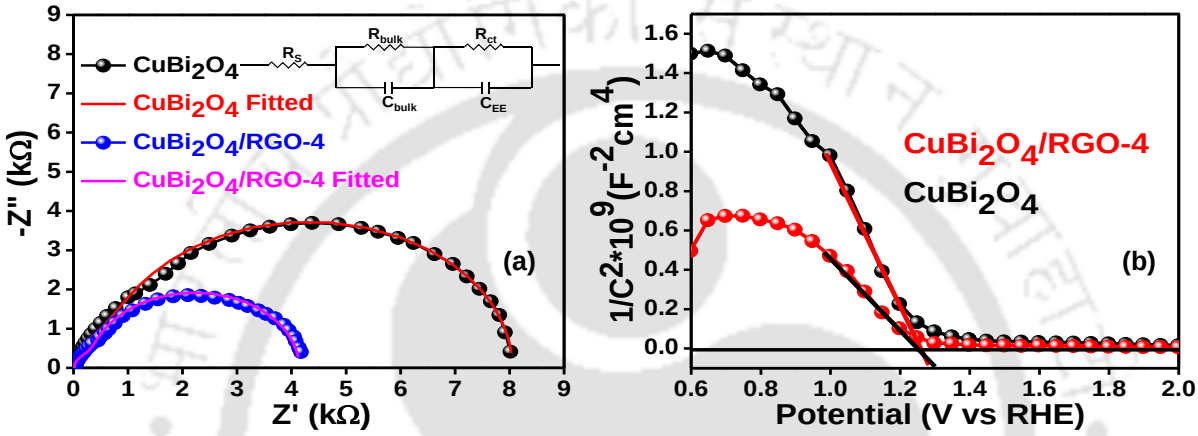

Figure 3.12. (a) The Nyquist plot of $CuBi_2O_4$ and $CuBi_2O_4$/RGO-4 photocathodes, inset of the figure shows the circuit diagram used to fit the obtained data. (b) Mott–Schottky plot of $CuBi_2O_4$ and $CuBi_2O_4$/RGO-4 photocathodes in 0.5 M Na_2SO_4 at 1 kHz.

Table 3.1. Fitting parameter obtained after fitting the Nyquist plot

Photocathode	R_S (Ω)	R_{bulk} (Ω)	R_{ct}(Ω)	Carrier Density (cm^{-3})
$CuBi_2O_4$/RGO-4	15.28	183.7	2982	7.92 X 10^{20}
$CuBi_2O_4$	26.29	673.6	4990	3.76 x 10^{20}

Figure 3.12 shows the Bode phase plot of $CuBi_2O_4$ and $CuBi_2O_4$/RGO-4 using which lifetime of photo-excited electrons can be calculated by using the formula [41]

$$\tau_e = 1/(2\pi f_{max}) \quad (3.3)$$

τ_e is the lifetime of the photo-excited electron, f_{max} is the maximum pick frequency. In **Figure 3.13,** the f_{max} for $CuBi_2O_4$/RGO-4 and $CuBi_2O_4$ is 60.26 and 82.67 and the lifetime of photo-excited electrons was calculated to be 2.6 msec and 1.9 msec respectively. RGO acting as

electron sink suppress electron-hole recombination by rapidly accepting a photo-induced electron from $CuBi_2O_4$ surface, improving electron lifetime.

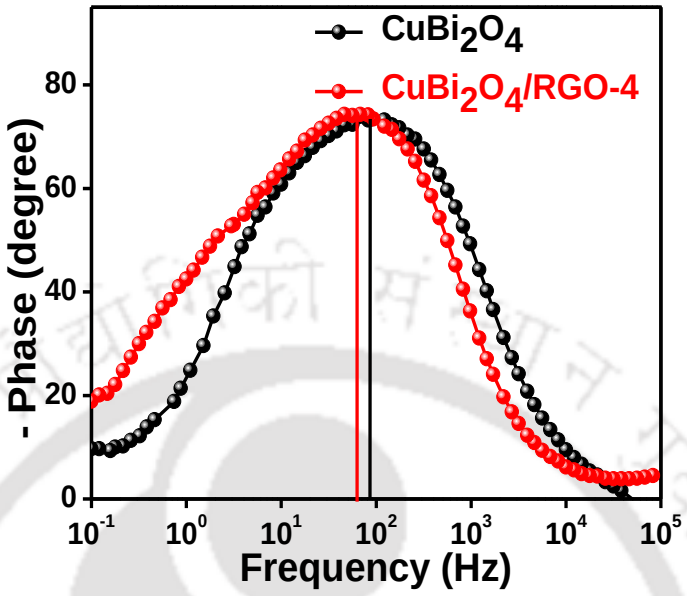

Figure 3.13. Bode phase plot of $CuBi_2O_4$ and $CuBi_2O_4$/RGO-4 showing an enhanced lifetime of photo-excited electrons in $CuBi_2O_4$/RGO-4 then pristine $CuBi_2O_4$.

3.3.8 Stability and Faradaic Yield Measurements

Figure 3.14 (a) shows the amount of hydrogen gas evolved and the corresponding Faradaic efficiency of $CuBi_2O_4$/RGO-4 photocathode. Hydrogen evolved was monitored through online GC, technique at a fixed potential (-0.6 V vs Ag/AgCl) through a chronoamperometry under 1 Sun illumination of light for 1 hour in 0.5 M Na_2SO_4 electrolyte. Faradaic efficiency is the ratio of experimental hydrogen production rate and hydrogen production rate calculated theoretically. Impressive Faradic efficiency of 91.7 % was achieved for $CuBi_2O_4$/RGO-4 photocathode which indicates that the photocurrent generated in the modified electrode in **Figure 3.9 (a)** attributed purely to the water reduction. Apart from the catalytic activity, operational stability is an equally important parameter for practical applications. Therefore, a long-term stability test of each pristine and modified $CuBi_2O_4$/RGO-4 photocathode was carried out under continuous illuminations at 0 V_{RHE}. **Figure 3.14 (b)**

Part of this chapter has been published in **Sustainable Energy Fuels, 2019, 3, 1554**

shows the stability test of both the electrode, it was observed that the photocurrent density of pristine $CuBi_2O_4$ decreased to ~17% till one hour of stability test. While with the incorporation of RGO over $CuBi_2O_4$, $CuBi_2O_4$/RGO-4 shows better stability without any significant decay in photocurrent density.

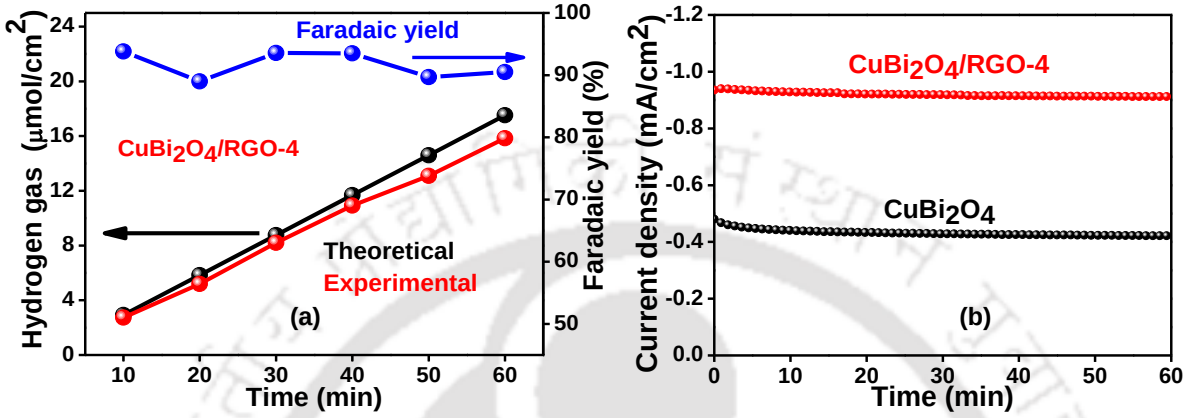

Figure 3.14. (a) Amount of hydrogen gas evolved under 1 Sunlight illumination with time and corresponding faradaic efficiency of $CuBi_2O_4$/RGO-4 photocathode. (b) Operational stability of $CuBi_2O_4$/RGO-4 and pristine $CuBi_2O_4$ photocathodes recorded at 0 V_{RHE} under continuous illumination.

3.3.9 Mechanism for Enhanced HER Performance

Scheme 3.2 shows the mechanism taking place in $CuBi_2O_4$/RGO-4 for enhanced HER performance. Here, when Sunlight was shined over low bandgap pristine $CuBi_2O_4$, the electrons from the valence band are excited to the conduction band. These electrons in the conduction band are used in the reduction of water to produce hydrogen. However, due to the low bandgap of $CuBi_2O_4$, most of the charge carriers generated during the process got recombined, hence reducing the HER performance of pristine $CuBi_2O_4$. To overcome this drawback, $CuBi_2O_4$ overlaid with excellent charge extractor RGO over it. Therefore, in the modified electrode $CuBi_2O_4$/RGO-4, when electrons got generated in $CuBi_2O_4$/RGO-4 upon application of Sunlight, RGO acting as charge sink, immediately extracts electrons from the conduction band of $CuBi_2O_4$. Thereafter, the reduction of water takes place over the RGO surface. The enhancement in photocurrent density can be ascribed to efficient and rapid charge

collection of RGO sheets from $CuBi_2O_4$ before charge carriers get recombined. RGO also boosts charge injection from photocathode to electrolyte solution which results in a higher photoelectrochemical reduction of water. Hence reducing recombination, and increasing charge injection efficiency results in enhanced water reduction efficiency of $CuBi_2O_4$/RGO-4.

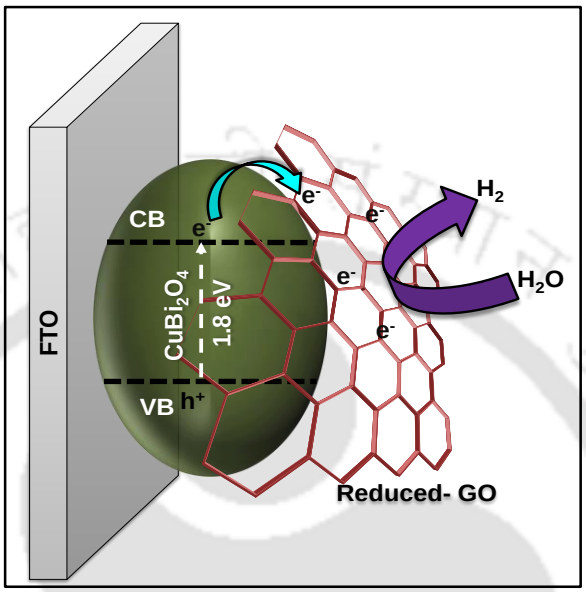

Scheme 3.2. Mechanism taking place in $CuBi_2O_4$/RGO-4 for enhanced HER performance.

3.4 CONCLUSIONS

A noble metal-free, $CuBi_2O_4$ composited with RGO layer was proposed to be an efficient photoelectrochemical water reduction catalyst. A shift in Bi 4f and Cu 2p peaks in XPS spectra indicates an electronic interaction between $CuBi_2O_4$ and RGO. RGO amount has over $CuBi_2O_4$ was optimized using different cycles of spin-coating for obtaining maximum current density in the modified photocathode. A ~2-fold increment in the photocurrent density in $CuBi_2O_4$/RGO-4 in comparison to pristine $CuBi_2O_4$ is a result of efficient charge separation owing to the electronic interactions between $CuBi_2O_4$ and RGO. Impressive Faradaic efficiency of 91.7% is obtained confirming our claim of superior water reduction is the main reason for the enhanced PEC. Further, carrier density for $CuBi_2O_4$ is 3.76 x 10^{20} cm^{-3} and 7.92 x 10^{20} cm^{-}

TH-2636_166122040

Part of this chapter has been published in **Sustainable Energy Fuels, 2019, 3, 1554**

^{3} for $CuBi_2O_4$/RGO-4 from the Mott-Schottky plot confirms the proposed mechanism for the enhanced photoelectrochemical water reduction.

3.4 REFERENCES

1. C. Jiang, S. J. A. Moniz, A. Wang, T. Zhang and J. Tang. *Chem. Soc. Rev.*, 2017, **46**, 4645.
2. Y. Park, K. J. McDonald and K. S. Choi. *Chem. Soc. Rev.*, 2013, **42**, 2321.
3. B. Seger, I. E. Castelli, P. C. K. Vesborg, K.W. Jacobsen, O. Hansen and I. Chorkendorff. *Energy Environ. Sci.*, 2014, **7**, 2397.
4. A. Paracchino, N. Mathews, T. Hisatomi, M. Stefik, S. D. Tilley and M. Grätzel. *Energy Environ. Sci.*, 2012, **5**, 8673.
5. C. G. Read, Y. Park and K. S. Choi. *J. Phys. Chem. Lett.*, 2012, **3**, 1872.
6. S. P. Berglund, F. F. Abdi, P. Bogdanoff, A. Chemseddine, D. Friedrich and R. van de Krol. *Chem. Mater.*, 2016, **28**, 4231.
7. G. Sharma, Z. Zhao, P. Sarker, B. A. Nail, J. Wang, M.N. Huda and F.E. Osterloh. *J. Mater. Chem. A.*, 2016, **4**, 2936.
8. J. Li, M. Griep, Y. Choib and D. Chu. *Chem. Commun.*, 2018, **54**, 3331.
9. D. Cao, N. Nasori, Z. Wang, Y. Mi, L. Wen, Y. Yang, S. Qu, Z. Wang and Y. Lei. *J. Mate. Chem. A.*, 2016, **4**, 8995.
10. L. Zhu, P. Basnet, S. R. Larson, L. P. Jones, J. Y. Howe, R. A. Tripp and Y. Zhao. *ChemistrySelect*, 2016**, 1**, 1518.
11. H. S. Park, C.-Y. Lee and E. Reisner. *Phys. Chem. Chem. Phys.*, 2014, **16**, 22462.
12. F. Wang, W. Septina, A. Chemseddine, F. F. Abdi, D. Friedrich, P. Bogdanoff, R. van de Krol, S. D. Tilley and S. P. Berglund. *J. Am. Chem. Soc.*, 2017, **139**, 15094.
13. Y.-H. Choi, K. D. Yang, D.-H. Kim, K. T. Nam and S.-H. Hong. *Mater. Lett.*, 2017, **188**, 192.

14. F. Guo, W. Shi, H. Wang, M. Han, W. Guan, H. Huang, Y. Liu and Z. Kang. *J. Hazard. Mater.,* 2018, **349**, 111.

15. S. Liu, J. Zhou, Y. Lu and J. Su. *Sol. Energy Mater Sol. Cells,* 2018, **180**, 123.

16. E. Abdelkader, L. Nadjia and B. Ahmed. *J. King Saud Univ. Sci.,* 2015, **27**, 76.

17. M. Faraji, M. Youse, S. Yousefzadeh, M. Zirak, N. Naseri,T. H. Jeon, W. Choi and A. Z. Moshfegh. *Energy Environ.Sci.,* 2019, **12**, 59.

18. T. Su, Q. Shao, Z. Qin, Z. Guo and Zili Wu. *ACS Catal.,* 2018, **8**, 2253.

19. M. Pesci, M. S. Sokolikova, C. Grotta, P. C. Sherrell, F. Reale,K. Sharda, N. Ni, P. Palczynski and C. Mattevi. *ACS Catal.,* 2017, **7**, 4990.

20. A. Iwase, S. Yoshino, T. Takayama, Y. H. Ng, R. Amal and A. Kudo. *J. Am. Chem. Soc.*, 2016, **138**, 10260.

21. J. Zhang, J. Yu, M. Jaroniec and J. Ru Gong. *Nano Lett.,* 2012, **12**, 4584.

22. R. Boppella, S. T. Kochuveedu, H. Kim, M. J. Jeong, F. MarquesMota, J. H. Park and D. H. Kim. *ACS Appl. Mater. Inter.,* 2017, **9**, 7075.

23. S. Park, J. An, J.R. Potts, A. Velamakanni, S. Murali and R.S. Ruoff. *Carbon,* 2011, **49**, 3019.

24. Z. V. Popovic, G. Kliche, M. Cardona and A. Liu. *Phys. Rev. B*, 1990, **41**, 3824.

25. B. Gupta, N. Kumar, K. Panda, V. Kanan, S. Joshi and I. Visoly-Fisher. *scientific Reports*, 2017, **7**, 45030.

26. D. Y.W. Yu, S. K. Batabyal, J. Gun, S. Sladkevich, A. A. Mikhaylov, A. G. Medvedev, V. M. Novotortsev, O. Lev and P. V. Prikhodchenko. *Main Group Met. Chem*., 2015, **38**, 43.

27. D. Kang, J. C. Hill, Y. Park and K.-S. Choi, *Chem. Mater.*, 2016, **28**, 4331.

28. Y. Dai, Y. Sun, J. Yao, D. Ling, Y. Wang, H. Long, X. Wang, B. Lin, T.H. Zeng and Y. Sun. *J. Mater. Chem. A,* 2014, **2**, 1060.

29. C. Wang, D. Meng, J. Sun, J. Memon, Y. Huang and J. Geng, *Adv. Mater. Interfaces*, 2014, **1**, 1300150.

30. J. Li, Z. Zhao, Y. Ma and Y. Qu. *ChemCatChem*, 2017**, 9**, 1554.

31. J. S. Li, Y. Wang, C. H. Liu, S. L. Li, Y. G. Wang, L. Z. Dong, Z. H. Dai, Y. F. Li and Y. Q. Lan. *Nat. Commun.*, 2016, **7**, 11204.

32. Y. R. Lu, P. F. Yin, J. Mao, M. J. Ning, Y. Z. Zhou, C. K. Dong, T. Ling and X. W. Du. *J. Mater. Chem. A*, 2015, **3**, 18521.

33. T. W. Kim and K.-S. Choi. *Science*, 2014, **343**, 990.

34. A. Zaban, M. Greenshtein and J. Bisquert. *ChemPhysChem*, 2003, **4**, 859.

35. Z. Zhang and P. Wang. *Energy Environ. Sci.*, 2012, **5**, 6506.

36. Y. Zhang, B. Tang, Z. Wu, H. Shi, Y. Zhang and G. Zhao. *Green Chem.*, 2016, **18**, 2424.

37. J. Yang, C. X. Bao, T. Yu, Y. F. Hu, W. J. Luo, W. D. Zhu, G. Fu, Z. S. Li, H. Gao, F. M. Li and Z. G. Zou. *ACS Appl. Mater. Inter.*, 2015, **7**, 26482.

38. X.-D. Wang, Y.-F. Xu, B.-X. Chen, N. Zhou, H.-Y. Chen, D.-B. Kuang and C.-Y. Su. *ChemSusChem*, 2016, **9**, 3012.

39. S. Lee, S. Cha, Y. Myung, K. Park, I. H. Kwak, I. S. Kwon, J. Seo, S. A. Lim, E. H. Cha and J. Park. *ACS Appl. Mater. Inter.*, 2018, **10**, 33198.

40. D. Kang, J. C. Hill, Y. Park and K.-S. Choi. *Chem. Mater.*, 2016, **28**, 4331.

41. Y. Yang, R. Xie, Y. Liu, J. Li and W. Li. *Catalysts*, 2015, **5**, 2024.

CHAPTER 4

Surface-engineering decahedral indium doped bismuth vanadate using g-C_3N_4 quantum dots for improved oxygen evolution reaction

Manipulating the properties of semiconductor surfaces for better charge extraction and efficiency forms the basis of the present study. The surface of photocatalysts critically determines the efficiency of water oxidation by providing suitable reaction sites and energetics. In this chapter, we have chosen monoclinic $BiVO_4$ as a model system due to its suitable band structure and stability, making it a promising material for photoelectrochemical water oxidation. An in-situ growth procedure yields $BiVO_4$ photoanode with distinctive morphology. Herein, various studies are done to get insight into the change in the surface and bulk properties of dual modified $BiVO_4$, and their effect on the water oxidation efficiency of the photoanode.

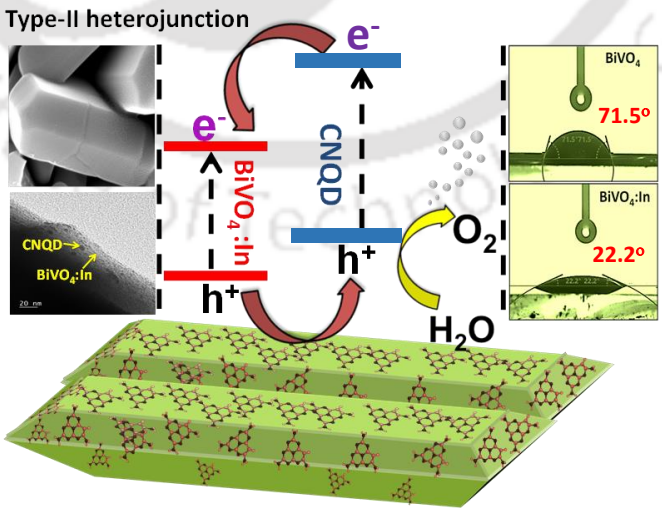

A. K. Shah, et al., **J. Power Sources,** 2020, 477, 229024.

4.1 INTRODUCTION

Ideal photoactive materials for photoelectrochemical (PEC) water splitting must have a suitable bandgap, proper band position, favourable surface energetics, cost-effective, non-toxic, and stability under harsh acidic and basic conditions. Among the popular metal oxides such as TiO_2, ZnO, $BiVO_4$, and WO_3 are used for photoelectrochemical water splitting.[1] $BiVO_4$ has potential due to its optimal bandgap (2.4-2.5 eV) for visible light absorption, suitable band positions, non-toxicity, and abundancy, with a theoretical photocurrent density of up to 7 mA/cm^2.[2,3] Despite its advantages, $BiVO_4$ has few drawbacks such as poor electron mobility, short diffusion length, and sluggish water oxidation kinetics which limits the photoelectrochemical efficacy.[4,5] Various efforts including the formation of a p–n heterojunction ($Cu_2O/BiVO_4$), a co-catalyst approach ($BiVO_4$/RGO/NiFe), combining with other semiconductors ($SnO_2/BiVO_4$), and improving carrier density by doping (Mo-doped $BiVO_4$) has been made to improve the water oxidation efficiency of $BiVO_4$.[6-11] In recent times, more attention has been paid on layered two-dimensional graphitic carbon nitride (g-C_3N_4), and is reported to be a potential photocatalyst owing to its suitable band structure with a bandgap of (2.7-2.8) eV, chemical inertness, cost-effective, and environmental-friendly nature.[12-13] However, bulk g-C_3N_4 has the stacking of polymeric layers resulting in limited surface to volume ratio and rapid recombination of electron and hole pairs. Bulk g-C_3N_4, when used in a heterojunction approach with other photoactive materials, is known to have very few electronic interactions with a coupled semiconductor material, limiting the synergistic movement of charge carriers. Many efforts are made to overcome these challenges, with the main emphasis on breaking bulk g-C_3N_4 into nanostructures such as nanosheets, nanorods, etc.[14,15] In these series, g-C_3N_4 quantum dots show great potential due to their high surface area to volume ratio, better surface kinetics for water oxidation, compared to bulk g-C_3N_4.

TH-2636_166122040

Part of this chapter has been published in **J. Power Sources, 2020, 477, 229024**

Present work emphasized the dual modification of $BiVO_4$, for enhanced PEC water oxidation efficiency by altering its electronic structure, deliberately creating oxygen vacancies to alter the energetics of the surface, facilitating charge transfers, and enhancing the surface reaction kinetics for water oxidation. Herein, indium doped $BiVO_4$ was synthesized directly over FTO, for improved carrier density extraction of $BiVO_4$:In. The ionic radius of In^{3+} is 0.8 ˚A which is similar to the ionic radius of Bi^{3+} (1.03 ˚A) can replace the partial sites of Bi^{3+} in $BiVO_4$.[10] Additionally, for the first time melamine was used as a precursor for low temperature, green hydrothermal synthesis route of g-C_3N_4 quantum dots. Herein, CNQDs facilitate a type – II kind of heterojunction with $BiVO_4$:In thereby enhancing the water oxidation kinetics of ($BiVO_4$:In)-CNQD photoanode.

4.2 EXPERIMENTAL SECTION

4.2.1 Fabrication of $BiVO_4$:In photoanode

Scheme 4.1 represents a step-by-step fabrication procedure of ($BiVO_4$:In)-CNQD photoanode. Monoclinic $BiVO_4$ was synthesized directly over fluorine-doped tin oxide (FTO) by following a two-step synthetic process.[16,17] In the first step, $BiVO_4$ seed layer solution was prepared by dissolving bismuth (III) nitrate pentahydrate (0.81 g), ammonium metavanadate (0.194 g), and citric acid (0.7 g) in 5 ml, 23% nitric acid. Polyvinyl alcohol (0.4 g) in 1.25 ml acetic acid was stirred for 0.5 h in another beaker, later it was added to the above prepared solution and was kept stirring overnight. As the prepared seed-layer solution was then spin-coated over FTO by drop-casting 100 µl (per cm^2 FTO) of precursor solution at 4000 rpm for 50 sec. It was then annealed at 400 ºC (ramp 10 ºC/min) for 4 h in a muffle furnace to form a uniform $BiVO_4$ seed layer over FTO. The second step includes the preparation of a suspension of the $BiVO_4$ precursor solution. Herein, 0.976 g of bismuth (III) nitrate pentahydrate and 0.233 g ammonium metavanadate were dissolved in 50 ml 14 % nitric acid solution in a round bottom

 Part of this chapter has been published in **J. Power Sources, 2020, 477, 229024**

flask. Under vigorous stirring, $NaHCO_3$ was added to the above solution till yellow suspension forms, and the pH of the solution was maintained at pH ~ 1. Seed layer coated FTO was put into a round bottom flask and refluxed at 60 °C for 6 h. The temperature of the reflux was lower down to 40 °C and was kept on reflux for another 6 h. After the reflux, the sample was washed with water and ethanol followed by annealing at 500 °C (ramp 10 °C/min) for 2 h in air. $BiVO_4$:In photoanode was fabricated by following the same procedure mentioned above, dissolving indium chloride (4 at.%, 6 at.%, 7 at.%, 8 at.%) to the suspension of $BiVO_4$ precursor solution.

4.2.2 Synthesis of g-C_3N_4 Quantum Dots (CNQD)

CNQDs were synthesized by a low-temperature hydrothermal process using melamine as a precursor. Herein, 0.5 g of melamine was stirred for 3 h in 35 ml MilliQ water and was put in a 50 ml autoclave maintaining hot air oven at 200 °C for 24 h. A faint yellows transparent g-C_3N_4 quantum dots were obtained and were filtered using a 0.22 μm syringe filter. Dialysis was done to further purify the obtained g-C_3N_4 quantum dots solution.

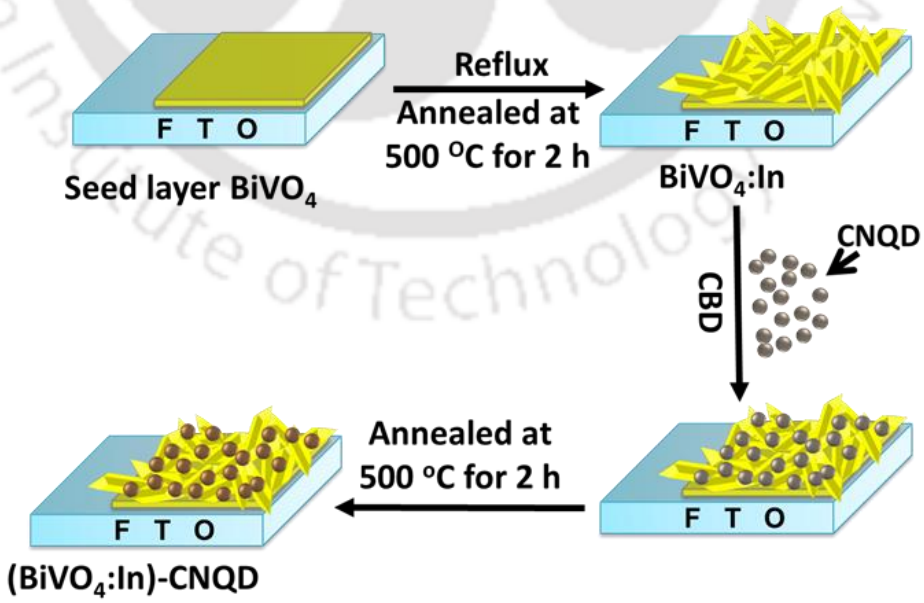

Scheme 4.1. Step-by-step fabrication procedure of ($BiVO_4$:In)-CNQD photoanode.

4.2.3 Fabrication of (BiVO4:In)-CNQD Photoanode

(BiVO4: In)-CNQD photoanode was fabricated by loading CNQDs over in-situ grown BiVO4:In photoanode by chemical bath deposition (CBD) method. In-situ grown BiVO4:In was kept immersed in CNQDs solution for different intervals of time (7 h, 8h, and 9 h). CNQDs loaded BiVO4:In photoanode was further heated at 500 ºC for 2 h to obtain (BiVO4:In)-CNQD photoanode.

4.3 RESULTS AND DISCUSSIONS

4.3.1 Powder X-Ray Diffraction (PXRD) Analysis

Diffraction peaks are indexed in **Figure 4.1 (a)** matches with the monoclinic scheelite phase of BiVO4 (JCPDS No. 14-0688)[18,19] confirming phase purity and crystal structure of as-synthesized BiVO4 photoanode. The diffraction peaks of BiVO4 and (BiVO4:In)-CNQD photoanode are identical, suggesting indium doping doesn't change the phase of BiVO4 after doping.

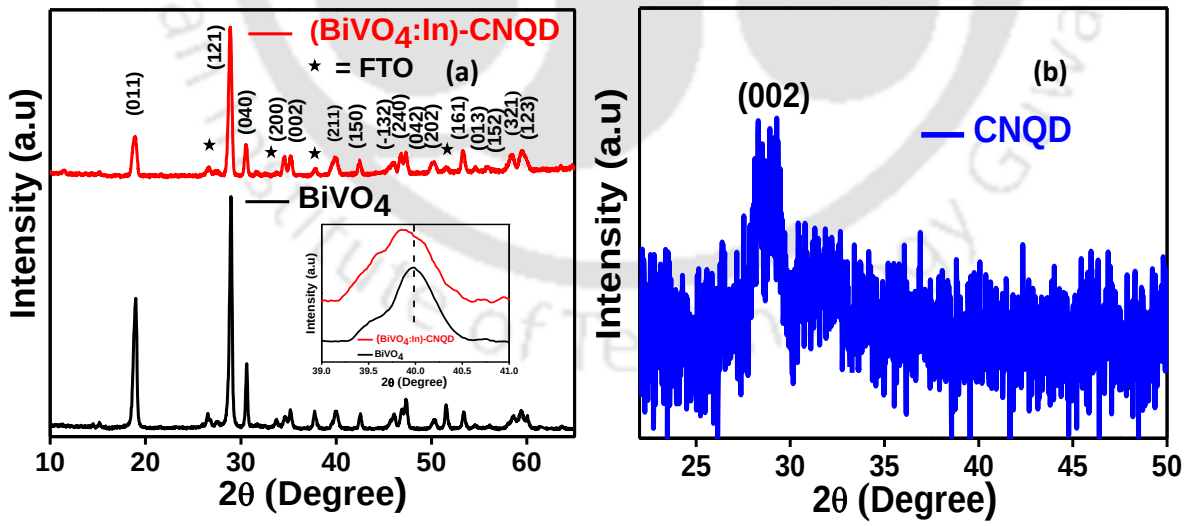

Figure 4.1. (a) Powder X-ray diffraction (PXRD) pattern of BiVO4 and (BiVO4:In)-CNQD photoanodes over FTO. Inset to figure shows a shift in peak position to the lower 2θ value indicative of indium doping into the BiVO4. (b) Powder X-ray diffraction (PXRD) pattern of pristine CNQDs.

 Part of this chapter has been published in **J. Power Sources, 2020, 477, 229024**

The (BiVO4:In)-CNQD photoanode does not show peaks for CNQDs due to very less amount of CNQDs in (BiVO4:In)-CNQD photoanode. Inset in **Figure 4.1 (a)** shows a shift in PXRD peak at (211) plane of (BiVO4:In)-CNQD photoanode towards lower 2θ value in comparison to its pristine counterpart, indicating doping in BiVO4. **Figure 4.1 (b)** shows the powder X-ray diffraction (PXRD) pattern of CNQDs which confirms the formation of CNQDs.[20]

4.3.2 Raman Spectroscopy Analysis

Raman analysis shown in **Figure 4.2** was performed to further confirm the formation and to know doping in BiVO4 photoanode. Highly intense and weak bands at 870 cm^{-1} and 744 cm^{-1} corresponds to symmetric and asymmetric V-O mode of stretching, respectively. The bands at 386 cm^{-1} and 342 cm^{-1} correspond to symmetric and asymmetric bending modes of vibration of VO_4^{3-} tetrahedron. The band at 219 cm^{-1} and 129 cm^{-1} corresponds to external mode, revealing the structural information of BiVO4.[21] Raman spectrum of both BiVO4 and BiVO4:In photoanode in **Figure 4.2** look identical; however, highly intense peak at ~870 cm^{-1} shows a shift towards higher wave number indicates doping in BiVO4.

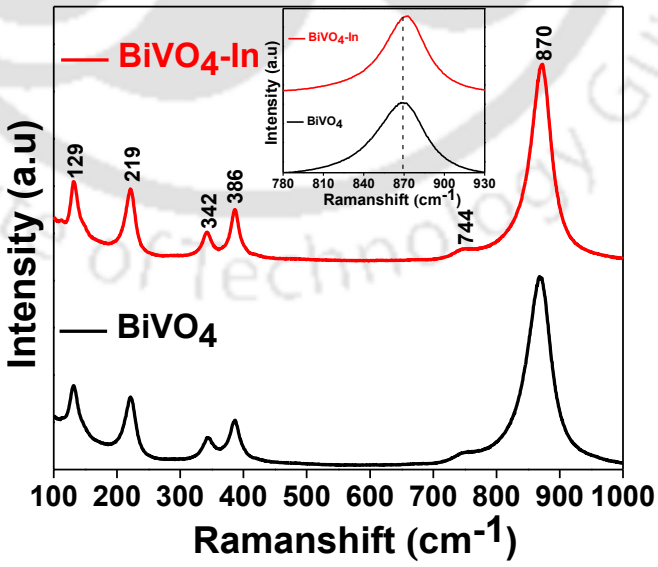

Figure 4.2. Raman spectra of BiVO4 and BiVO4:In photoanodes where the high intense band (~870) shows a shift towards higher Raman shift (shown in the inset).

Part of this chapter has been published in **J. Power Sources, 2020, 477, 229024**

4.3.3 UV-Visible Spectra Analysis

A UV-visible diffuse reflectance spectrum was used to study the optical properties of various prepared photoanodes. **Figure 4.3. (a)** shows the absorption curve of ($BiVO_4$:In)-CNQD photoanode, which remains unchanged to that of pristine $BiVO_4$ with an absorption edge at ~530 nm. To further check the formation of CNQDs, UV-visible spectra of CNQDs and bulk g-C_3N_4 were recorded as shown in **Figure 4.3 (b)**. The blue shift of the CNQDs curve in comparison to bulk g-C_3N_4 is due to quantum confinement in CNQDs indicating the formation of quantum dots.

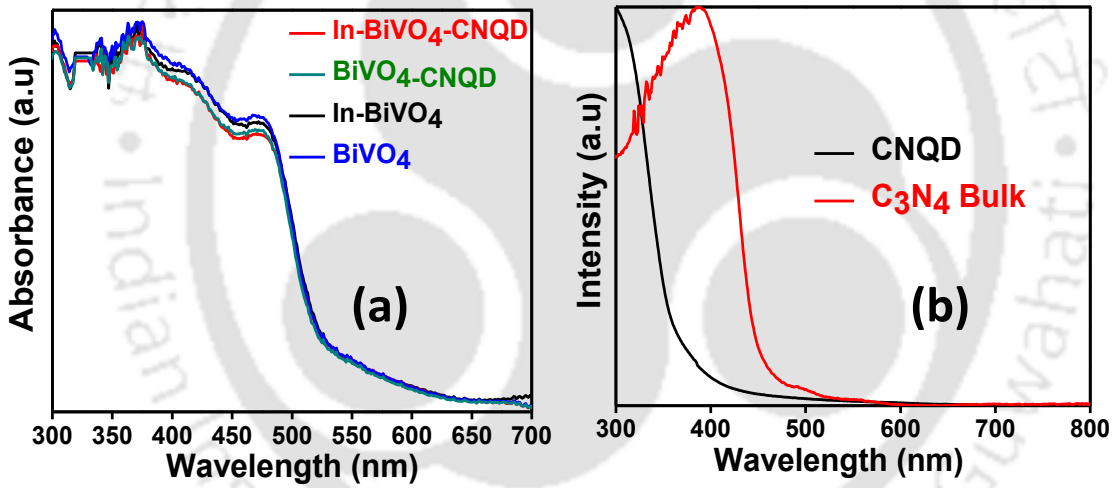

Figure 4.3. (a) UV-visible diffuse reflectance spectra of $BiVO_4$ and $BiVO_4$ modified photoanodes. (b) UV-visible spectra of CNQDs and bulk C_3N_4.

4.3.4 Photoluminescence (PL) Spectra

Further to check the stability of as-synthesized CNQDs Photoluminescence (PL) spectra of CNQDs were recorded (shown in **Figure 4.4**) just after synthesis and after 7 days of synthesis. There was not much change in PL intensity of CNQDs even after 7 days of synthesis, suggesting hydrothermally synthesized CNQDs using melamine as a precursor is very stable.

 Part of this chapter has been published in **J. Power Sources, 2020, 477, 229024**

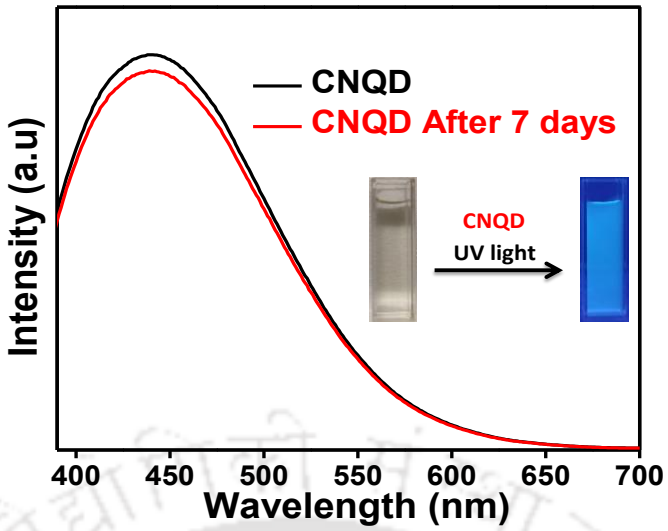

Figure 4.4. Photoluminescence (PL) spectra of CNQDs just after synthesis and after 7 days of storage. Inset in the figure shows CNQD displays strong blue fluorescence when illuminated with UV light.

4.3.5 Morphological and Structural Analysis

Figure 4.5 (a) shows the FESEM image of the seed layer over which crystals of $BiVO_4$ were grown. **Figure 4.5 (b)** shows the decahedron shaped pristine $BiVO_4$ photoanode grown over the seed layer. **Figure 4.5 (c)** shows the morphological features of $BiVO_4$:In coupled with g-C_3N_4 quantum dots.

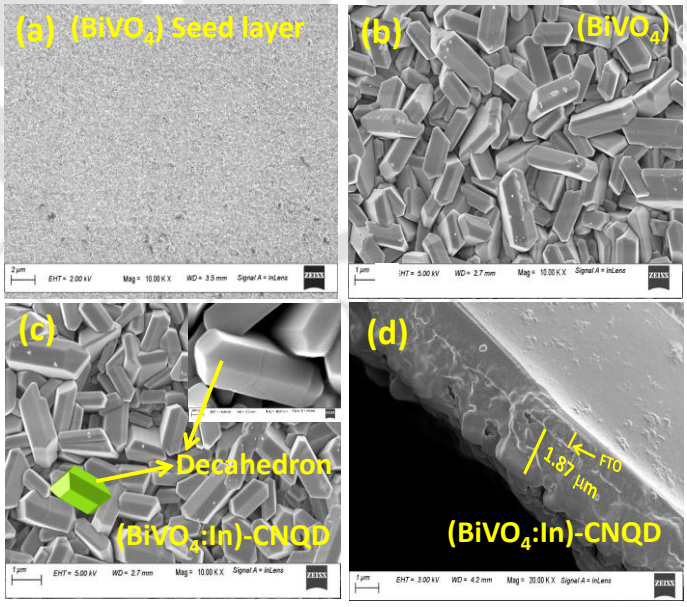

Figure 4.5 (a) FESEM image of $BiVO_4$ seed layer deposited uniformly over FTO through the spin coating. (b) FESEM image of pristine $BiVO_4$ photoanode. (c) FESEM image of decahedron shaped ($BiVO_4$:In)-CNQD

Part of this chapter has been published in **J. Power Sources, 2020, 477, 229024**

photoanode, it includes the representative graphic of decahedron shaped $BiVO_4$:In. (d) Cross-sectional FESEM image of ($BiVO_4$:In)-CNQD photoanode displaying thickness (~1.87μm) of the film formed over FTO.

Decahedron shaped $BiVO_4$:In showing facets, which provides higher surface area for the maximum deposition of catalyst for efficient water oxidation. FESEM image of pristine $BiVO_4$ and ($BiVO_4$:In)-CNQD photoanode in **Figure 4.5 (b)** and **Figure 4.5 (c)** respectively shows that with indium doping there was no significant change in morphology of $BiVO_4$ photoanode. The cross-sectional FESEM image in **Figure 4.5 (d)** shows that ($BiVO_4$:In)-CNQD photoanode has a film thickness of ~1.87μm formed over FTO.

Figure 4.6 (a) shows a FETEM image of a pristine $BiVO_4$ photoanode. **Figure 4.6 (b)** shows the FETEM image of well-distributed CNQDs with a uniform particle size of ~ 4 nm. **Figure 4.6 (c)** shows the FETEM image of ($BiVO_4$:In)-CNQD where CNQDs are well embedded on the surface of ($BiVO_4$:In), making good electronic interaction between $BiVO_4$:In and CNQDs which is distinguishable from pristine $BiVO_4$ photoanode as shown in **Figure 4.6 (a)**. The HRTEM image of ($BiVO_4$:In)-CNQD in **Figure 4.6 (d)** shows different lattice spacing of 0.29 nm and 0.33 nm which corresponds to (040) and (002) crystal plane of $BiVO_4$ and CNQDs, respectively, confirming loading of CNQDs over indium doped $BiVO_4$:In.[22,23]

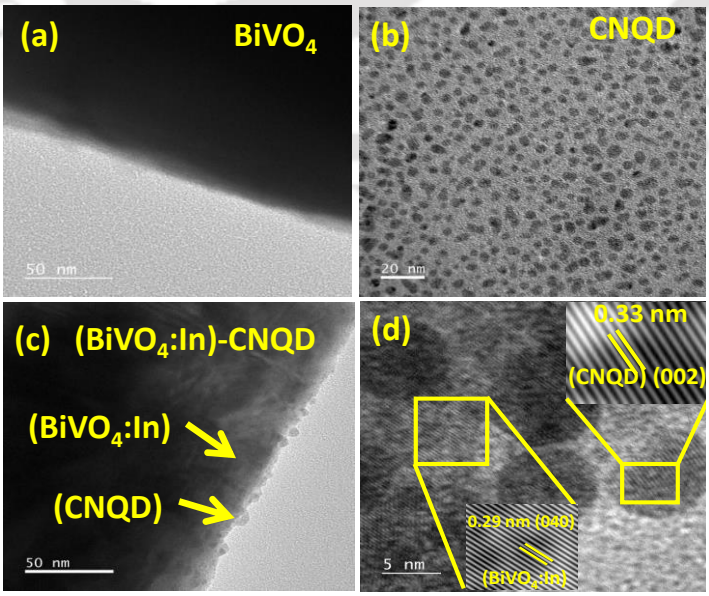

 Part of this chapter has been published in **J. Power Sources, 2020, 477, 229024**

Figure 4.6 (a) FETEM image of pristine $BiVO_4$ photoanode. (b) FETEM image of CNQDs. (c) FETEM image of ($BiVO_4$:In)-CNQD photoanode. (d) HRTEM image of ($BiVO_4$:In)-CNQD showing (040) and (002) crystal plane of $BiVO_4$ and CNQDs, respectively.

To further confirm the presence and uniform distribution of all the elements present, FETEM-EDX elemental mapping of ($BiVO_4$:In)-CNQD photoanode (**Figure 4.7 (a-f)**) was conducted. Elemental mapping shows that the elements Bi, V, O, In, C and N are uniformly distributed throughout the ($BiVO_4$:In)-CNQD photoanode.

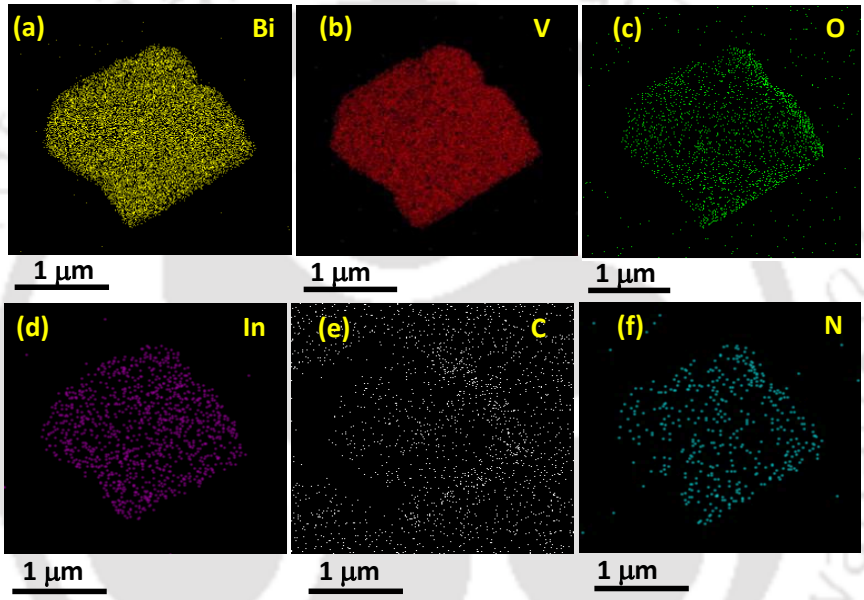

Figure 4.7 (a-f) shows uniform distribution of Bi, V, O, In, C, and N respectively in ($BiVO_4$:In)-CNQD photoanode.

4.3.6 FTIR Spectra Analysis

To further confirm formation and interaction between CNQD and $BiVO_4$:In in ($BiVO_4$:In)-CNQD, FTIR of pristine $BiVO_4$, CNQDs and ($BiVO_4$:In)-CNQD were performed as shown in **Figure 4.8**. A peak at 477cm^{-1} corresponds to symmetric bending of VO_4^{3-} while peaks at 816 cm^{-1} and 735 cm^{-1} corresponds to symmetric and asymmetric stretching of VO_4^{3-} which are clearly visible in $BiVO_4$. Inset in **Figure 4.8** shows FTIR spectra of CNQDs and ($BiVO_4$:In)-CNQD. Peaks at 1541 cm^{-1}, 1470 cm^{-1}, 1320 cm^{-1}, 1262 cm^{-1} correspond to symmetric stretching vibration mode of CN bond and CN heterocycles for CNQDs.[2,3] In

Part of this chapter has been published in **J. Power Sources, 2020, 477, 229024**

(BiVO4:In)-CNQD photoanode, there is a shift in CNQDs peaks from 1471 cm^{-1} to 1464 cm^{-1} towards lower frequency, which may be due to the weakening of CN bond indicating good interaction between CNQDs and BiVO4:In.

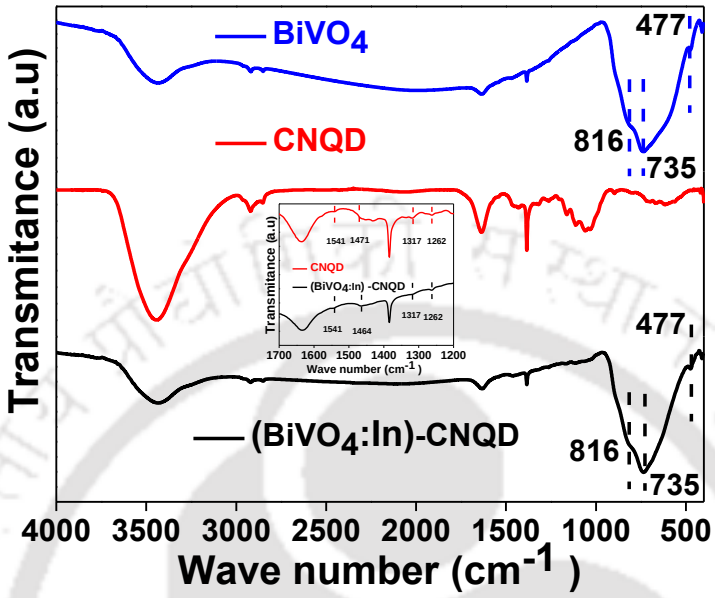

Figure 4.8. FTIR spectra of pristine $BiVO_4$, CNQDs and $BiVO_4$ modified photoanodes. The inset shows a shift in the FTIR peak of CNQDs in (BiVO4:In)-CNQD.

4.3.7 X-Ray Photoelectron Spectroscopy (XPS)

To find the electronic structural changes by virtue of chemical state and elemental composition of as-synthesized $BiVO_4$ and (BiVO4:In)-CNQD photoanode, XPS analysis was performed. The presence of corresponding elements was confirmed by the XPS survey spectra, as shown in **Figure 4.9 (a)**. Bi 4f core-level spectra of $BiVO_4$ and (BiVO4:In)-CNQD photoanodes are shown in **Figure 4.9 (b)**. Peaks at a binding energy of 159.08 eV and 164.37 eV correspond to Bi - $4f_{7/2}$ and $4f_{5/2}$ respectively of pristine $BiVO_4$, while for (BiVO4:In)-CNQD photoanode, Bi - $4f_{7/2}$ and $4f_{5/2}$ peaks appear at binding energy 158.77 eV and 164.07 eV. The presence of Bi - $4f_{7/2}$ and $4f_{5/2}$ peaks confirms the presence of Bi^{3+} in $BiVO_4$ and (BiVO4:In)-CNQD photoanodes.[24] A shift in Bi - $4f_{7/2}$ and $4f_{5/2}$ peaks of (BiVO4:In)-CNQD compared to pristine $BiVO_4$ photoanode is indicative of a change of electronic structure around Bi, suggests that the doping in the A-site of $BiVO_4$ in (BiVO4:In)-CNQD photoanode. **Figure**

Part of this chapter has been published in **J. Power Sources, 2020, 477, 229024**

4.9 (c) shows V 2p core-level spectra of $BiVO_4$ and ($BiVO_4$:In)-CNQD photoanode, peaks at binding energy 516.5 eV and 523.7 eV corresponds to V $2p_{1/2}$ and V $2p_{3/2}$ of $BiVO_4$, while peaks at 516.4 eV and 523.6 eV corresponds to V $2p_{1/2}$ and V $2p_{3/2}$ of ($BiVO_4$:In)-CNQD photoanode. The presence of V $2p_{1/2}$ and V $2p_{3/2}$ peaks in $BiVO_4$ and ($BiVO_4$:In)-CNQD photoanode establishes the presence of V^{5+}.[25] Insignificant shift in both the peaks in ($BiVO_4$:In)-CNQD in comparison to pristine $BiVO_4$ might be due to no or little change in the electronic environment around B sites of $BiVO_4$ in ($BiVO_4$:In)-CNQD photoanode. **Figure 4.9 (d)** shows C1s XPS spectra of ($BiVO_4$:In)-CNQD and CNQDs. Peaks at 284.61 eV, 286.22 eV, and 288.17 eV attributed to C=C, C-OH, and C-N=C of CNQDS, while peaks at 284.78 eV, 285.81 eV, and 289.11 eV attributed to C=C, C-OH and C-N=C of ($BiVO_4$:In)-CNQD photoanode.[26]

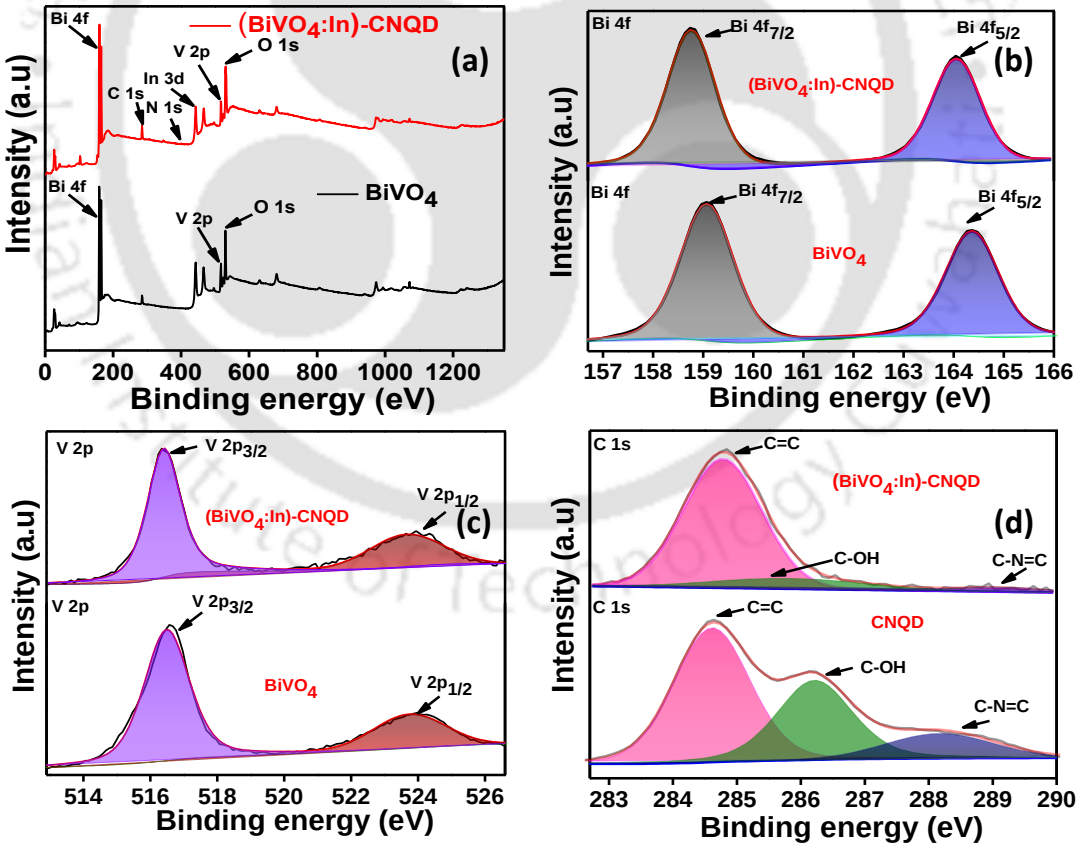

Figure 4.9. (a) Survey spectra of ($BiVO_4$:In)-CNQD and pristine $BiVO_4$ photoanodes. XPS spectra of (b) Bi 4f for pristine $BiVO_4$ and ($BiVO_4$:In)-CNQD photoanodes, (c) V 2p $BiVO_4$ and ($BiVO_4$:In)-CNQD photoanodes, (d) C 1s XPS spectra of ($BiVO_4$:In)-CNQD photoanode and CNQDs.

Part of this chapter has been published in **J. Power Sources, 2020, 477, 229024**

In **Figure 4.10 (a)**, peak at a binding energy of 445.22 eV corresponds to In $3d_{5/2}$ of In 3d in $BiVO_4$:In photoanode, while the peak at a binding energy of 445.87 eV corresponds to In $3d_{5/2}$ (shown in **Figure 4.10 (b)**) of ($BiVO_4$:In)-CNQD photoanode. The presence of In $3d_{5/2}$ and In $3d_{3/2}$ peaks confirms doping in $BiVO_4$:In and ($BiVO_4$:In)-CNQD photoanodes.[27] Shift in In $3d_{5/2}$ peak of ($BiVO_4$:In)-CNQD photoanode towards higher binding energy photoanode is due to the interaction of CNQD and $BiVO_4$:In. N 1s XPS spectra of ($BiVO_4$:In)-CNQD and CNQDs, peaks at binding energy 399.1 eV, 399.6 eV, 401.4 eV corresponds to C=N, N-(C)3 and N-H peaks of CNQDs, respectively, while peaks at 399.4 eV and 400.4 eV Corresponds to C=N and N-(C)3 respectively of ($BiVO_4$:In)-CNQD photoanode, shown in **Figure 4.10 (c)**.[28] Presence of C=C, C-OH, and C-N=C peaks in C 1s spectra of ($BiVO_4$:In)-CNQD photoanode (shown in **Figure 4.9 (d)**), while presence of C=N and N-(C)3 peaks in N 1s spectra of ($BiVO_4$:In)-CNQD photoanode shown in **Figure 4.10 (c)** confirms the loading of CNQD in ($BiVO_4$:In)-CNQD photoanode.[28,29]

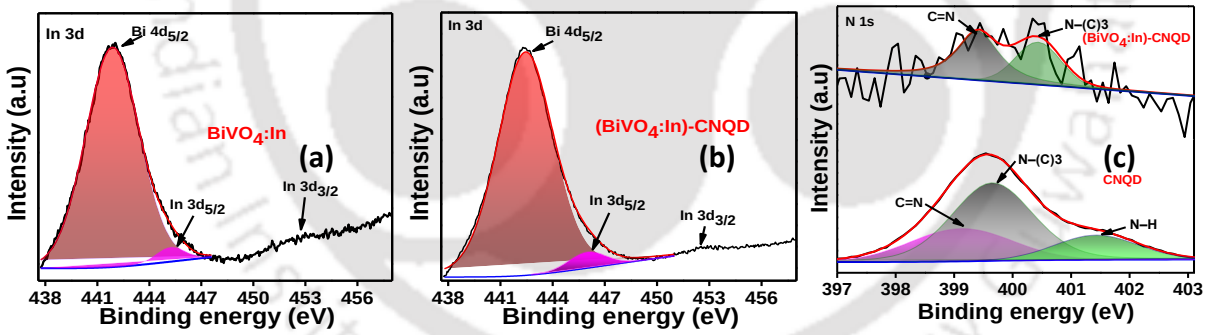

Figure 4.10. XPS spectra of (a) In 3d for $BiVO_4$:In photoanode, (b) In 3d for ($BiVO_4$:In)-CNQD photoanode. (c) N 1s for CNQDs and ($BiVO_4$:In)-CNQD photoanode.

4.3.8 Wettability Test of the Photoanodes

XPS analysis of O1s spectra of pristine $BiVO_4$ and $BiVO_4$:In photoanodes were shown in **Figure 4.11 (a)** and **Figure 4.11 (d)**.[30] With indium doping, there is an enhancement in oxygen vacancy (O_V) peak in $BiVO_4$:In photoanode. This enhanced feature can also be seen in O1s spectra of ($BiVO_4$:In)-CNQD photoanode (**Figure 4.11 (g)**), confirming that indium

doping in $BiVO_4$ favours the formation of oxygen vacancies in $BiVO_4$.[31-33] Further stronger adsorbed oxygen (O_A) signature was observed in O 1s spectra of both $BiVO_4$:In and ($BiVO_4$:In)-CNQD Photoanodes, while O_A peak was minimal in O1s spectra of pristine $BiVO_4$ photoanode. The above observations in the photoanodes provide an increased wettability of $BiVO_4$ with oxygen vacancies through indium doping.[34-36] Zeta potential values for pristine $BiVO_4$ and $BiVO_4$:In were found to be -16.6 mV, -26.4 mV respectively shown in **Figure 4.11 (b)** and **Figure 4.11 (e)**. **Figure 4.11 (h)** shows the Zeta potential value of ($BiVO_4$:In)-CNQD Photoanode measured to be -30.7 mV, which implies a more polar surface, leading to stronger adsorption of water molecules over $BiVO_4$ with indium doping compared to pristine $BiVO_4$ photoanode.[35]

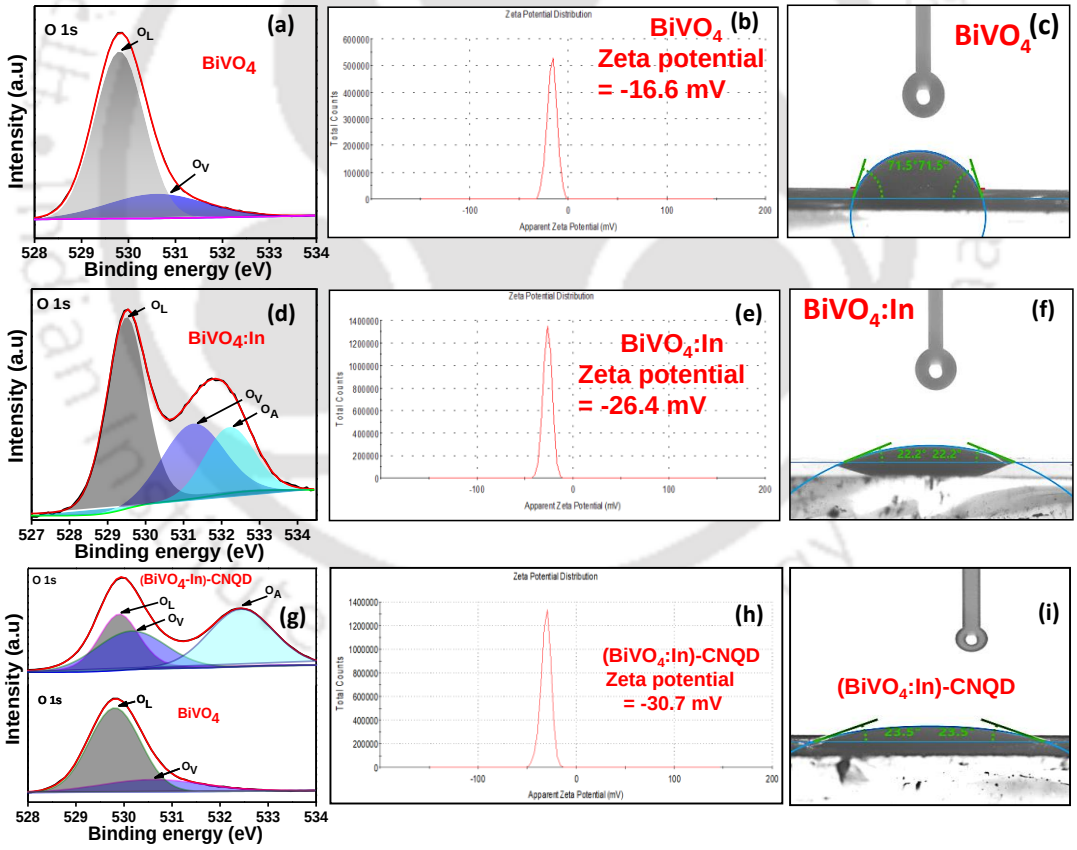

Figure 4.11. O 1s (O_L=lattice Oxygen, O_V= Oxygen vacancy, O_A= Adsorbed Oxygen) XPS spectra of (a, d, g) pristine $BiVO_4$, $BiVO_4$:In, ($BiVO_4$:In)-CNQD, respectively. Zeta potential measurement of (b, e, h) pristine $BiVO_4$, $BiVO_4$:In, ($BiVO_4$:In)-CNQD, respectively. Contact angle measurement of (c, f, i) pristine $BiVO_4$, $BiVO_4$:In, ($BiVO_4$:In)-CNQD, respectively.

To further confirm the enhanced wettability of In doped $BiVO_4$, contact angle measurements of $BiVO_4$ and $BiVO_4$:In were performed, as shown in **Figure 4.11 (c) and Figure 4.11 (f),** respectively. The contact angle value for pristine $BiVO_4$ and $BiVO_4$:In photoanodes were found to be 71.5° and 22.2°, respectively, confirming the degree of interaction between $BiVO_4$:In photoanode and water compared to pristine $BiVO_4$ photoanode. The ($BiVO_4$:In)-CNQD photoanode (shown in **Figure 4.11 (i)**) displayed a contact angle value of 23.5°.[35-36]

4.3.9. Type –II Heterojunction Between ($BiVO_4$:In)-CNQD and CNQD

In order to know the valence-band position of $BiVO_4$:In and CNQD, X-ray photoelectron spectroscopy (XPS) valence-band spectra analysis was done. **Figure 4.12. (a)** shows the valence band for $BiVO_4$:In and CNQD, and were calculated to be 2.7 eV and 1.91 eV, respectively. The conduction band of $BiVO_4$:In and CNQD were calculated using **equation 4.1** [37]

$$E_g = E_{cb} - E_{vb} \quad (4.1)$$

where E_g is the bandgap E_{cb} is the conduction band and E_{vb} is the valence band. The bandgap of $BiVO_4$:In was calculated to be ~2.44 eV from the UV-visible diffuse reflectance spectrum shown in **Figure 4.3 (a)** and bandgap of CNQDs (3.33 eV) obtained from **Figure 4.3 (b)**. Using equation (3), the E_{cb} of $BiVO_4$:In and CNQD were calculated to be 0.26 eV and -1.42 eV, respectively. Based on the band alignments calculated from the valence-band spectra analysis, a band energy diagram is proposed as shown in **Figure 4.12 (a)**. When light was illuminated upon ($BiVO_4$:In)-CNQD photoanode, excitons got generated in both $BiVO_4$:In and CNQDs of the composite, holes from the valance band of $BiVO_4$:In transfers to the valance band of CNQDs and the hot electrons from the conduction band of CNQDs transfers to the conduction band of $BiVO_4$:In, establishing a type-II heterojunction between $BiVO_4$:In and CNQDs. Thus the synergistic movement of charge carrier occurs between $BiVO_4$:In and CNQDs.[38,39]

 Part of this chapter has been published in **J. Power Sources, 2020, 477, 229024**

Subsequently, the oxidation of water takes place at the valance band of CNQDs to produce oxygen.

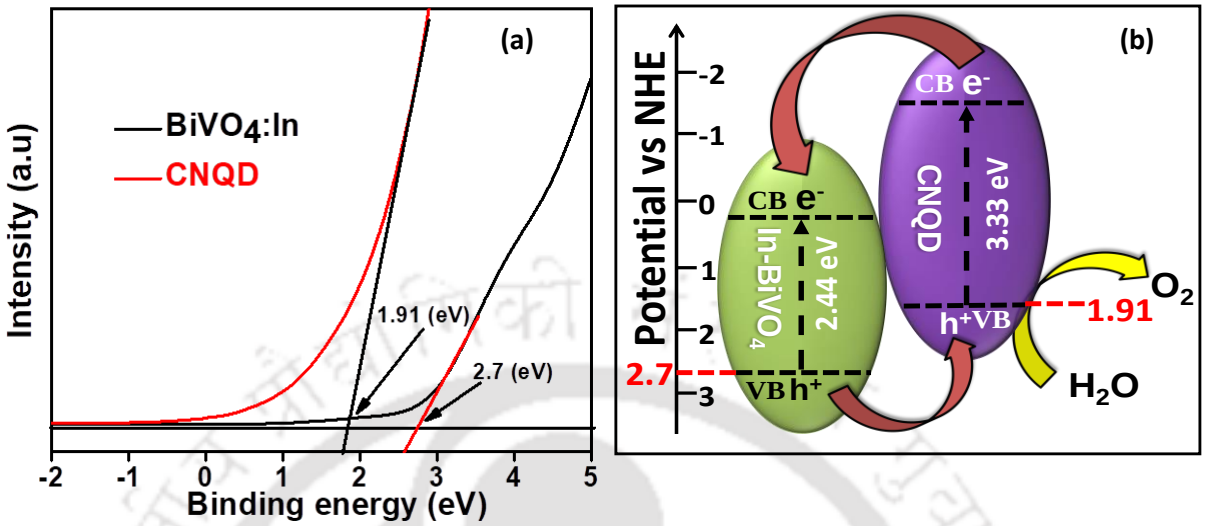

Figure 4.12. (a) X-ray photoelectron spectroscopy (XPS) valence-band spectra analysis $BiVO_4$:In photoanode and CNQDs. (b) Schematic representation of type –II heterojunction between ($BiVO_4$:In and CNQD with proper band position (bandgap = eV).

4.3.10 Photoelectrochemical Measurements

PEC performance of pristine $BiVO_4$ and the modified photoanodes are characterized by linear sweep voltammetry (LSV) under 1 Sun illumination at a scan rate of 10mV/sec in 0.5 M Na_2SO_4 shown in **Figure 4.13 (a)**. The photocurrent density of pristine $BiVO_4$ at 1.23 V was found to be ~0.64 mA/cm^2. Observed low photocurrent density value of pristine $BiVO_4$ photoanode is due to it its inherent poor electron mobility, reduced charge separation, and unavailability of charge carriers for the surface oxidation. To overcome the above drawbacks, the electronic structure of $BiVO_4$ was tuned by doping indium in $BiVO_4$. Photocurrent density of $BiVO_4$:In was optimized at various indium concentrations (at. %), as shown in **Figure 4.13 (b)**. The optimized photocurrent density of CNQDs loaded $BiVO_4$ (with different sensitization times) was recorded for $BiVO_4$-CNQD photoanode with a photocurrent density of ~1.26 mA/cm^2 as shown in **Figure 4.13. (c)**. In addition to ~4 fold increase in photocurrent density, ($BiVO_4$:In)-CNQD photoanode displays a notable cathodic shift in water oxidation onset

Part of this chapter has been published in **J. Power Sources, 2020, 477, 229024**

potential of 136 mV vs RHE as compared to its pristine counterpart. It was found that 7 at. % doped $BiVO_4$:In photoanode shows the highest photocurrent density of ~1.70 mA/cm^2. To further improve the photocurrent density, CNQDs were loaded over $BiVO_4$:In forming a type-II heterojunction, which exhibited an impressive photocurrent density of ~2.42 mA/cm^2 for ($BiVO_4$:In)-CNQD photoanode. Optimization of ($BiVO_4$:In)-CNQD photoanode was done by loading CNQDs using chemical bath deposition over $BiVO_4$:In photoanode for different time intervals, as shown in **Figure 4.13 (d)**. Enhancement in the photocurrent density with dual modification in ($BiVO_4$:In)-CNQD photoanode was ascribed to the creation of oxygen vacancy with indium doping, which enhances the availability of charge carrier density at the surface and improved charge separation in ($BiVO_4$:In)-CNQD. Hydrophilic nature with indium doping and creation of type-II heterojunction between $BiVO_4$:In and CNQD further contributes to the photoelectrochemical water oxidation efficiency of ($BiVO_4$:In)-CNQD photoanode.

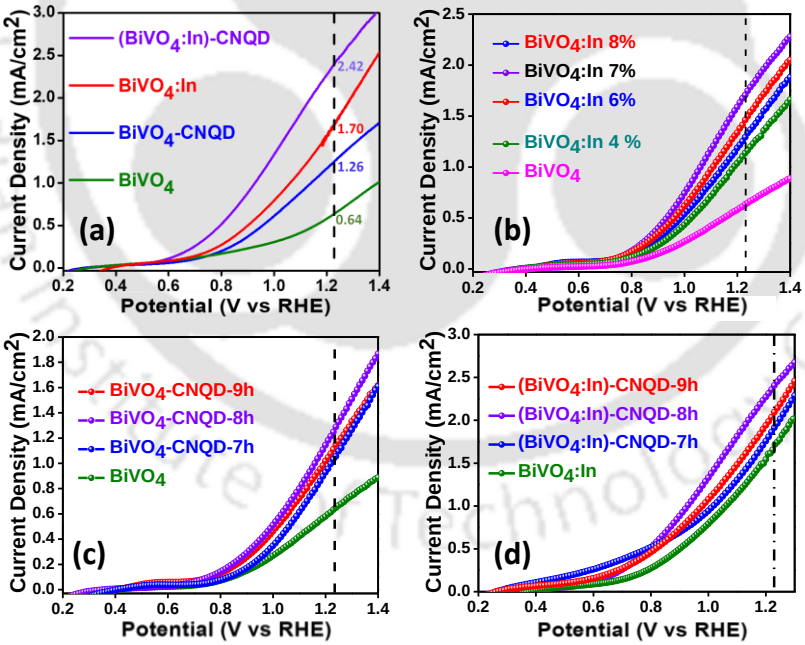

Figure 4.13. (a) Linear sweep voltammetry curve (LSV) of pristine $BiVO_4$ and all modified photoanodes under 1 Sun illumination at a scan rate of 10mV/sec in 0.5 M Na_2SO_4. (b) Linear sweep voltammetry curves for $BiVO_4$:In photoanode with different 'In' content (at%). (c) Linear sweep voltammetry curves of CNQDs loaded $BiVO_4$ for the different time intervals. (d) Optimization of ($BiVO_4$:In)-CNQD photoanode was done by loading CNQDs using chemical bath deposition (at room temperature) over $BiVO_4$:In photoanode for different time intervals.

To further understand the effect of dual modification in $BiVO_4$, incident photon-to-electron conversion efficiency (IPCE) measurements of photoanodes were done, as shown in **Figure 4.14**. An IPCE value of ~45% obtained for ($BiVO_4$:In)-CNQD photoanode while for pristine $BiVO_4$ photoanode only ~11% was of IPCE was recorded. There was a ~four-fold enhancement in IPCE value for ($BiVO_4$:In)-CNQD photoanode in comparison to pristine $BiVO_4$ photoanode, which is in good agreement to photocurrent density of ($BiVO_4$:In)-CNQD and pristine $BiVO_4$ photoanodes shown in **Figure 4.13 (a)**. An increase in IPCE value is attributed to increasing charge carrier density at the surface with indium doping and enhancement in charge separation between $BiVO_4$:In and CNQDs in ($BiVO_4$:In)-CNQD photoanode.

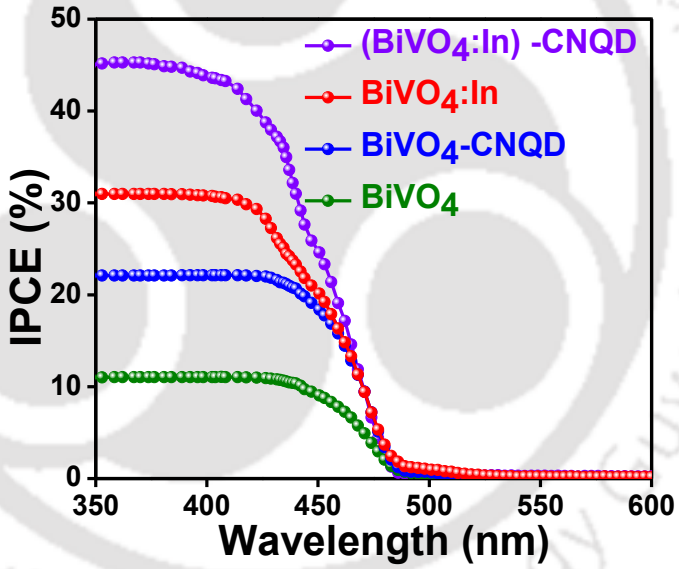

Figure 4.14. Incident photon-to-electron conversion efficiency (IPCE) spectra of $BiVO_4$ and all the modified photoanodes.

To further understand the light response of $BiVO_4$ and the modified photoanodes, chronoamperometry measurement was performed at a potential of 1.23 V vs RHE. The OFF condition did not show any significant dark current, while a steep rise in the photocurrent density is observed on illumination (ON condition), as shown in **Figure 4.15 (a)**. Upon illumination, pristine $BiVO_4$ photoanode shows a sharp anodic spike compared to the dual

modified (BiVO4:In)-CNQD photoanode, suggesting an improved charge separation kinetics in the modified photoanode by virtue of indium doping and enhanced charge separation due to type-II charge transfers across the coupled semiconductors.[40] Photocurrent density of all the photoanodes are in good agreement with the photocurrent values shown in **Figure 4.13 (a)**. To examine the reusability of (BiVO4:In)-CNQD, three consecutive linear sweep voltammetry measurements of (BiVO4:In)-CNQD were carried out, shown in **Figure 4.15 (b)**. The three consecutive measurements of (BiVO4:In)-CNQD confirms the reproducibility of the modified photoelectrode.

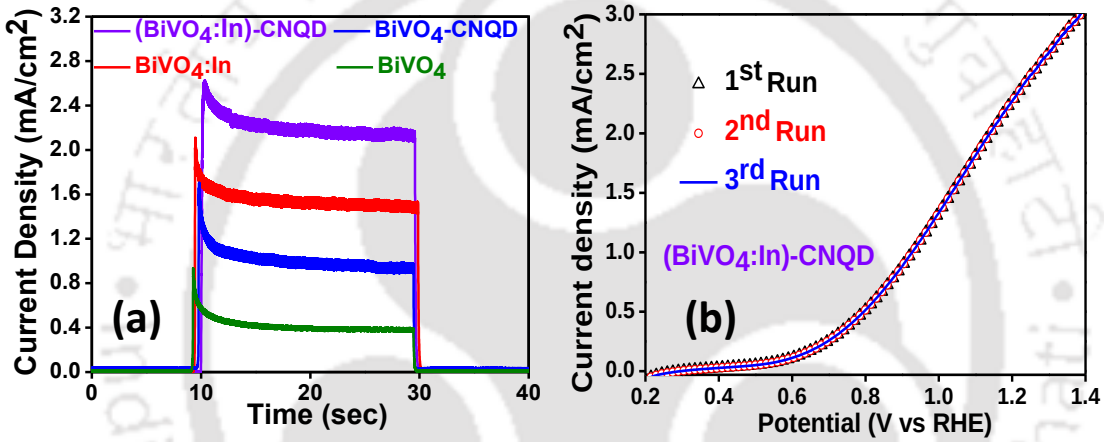

Figure 4.15. Photocurrent vs. time curve of BiVO4 and all the modified photoanodes at 1.23 V vs RHE. (b) Reusability test for (BiVO4:In)-CNQD.

Applied bias photon-to-current efficiency (ABPE) is used to represent the photo-response of a photoanode material under an applied bias, calculated (**Figure 4.16 (a)**) from J-V curve (**Figure 4.13 (a)**) using **equation 4.1** [41]

$$ABPE = \frac{J(1.23 - V_b)}{P_{light}} \quad (4.1)$$

J is the photocurrent density of the photoanodes at specific applied potential, V_b is the applied potential (V vs RHE), P_{light} is the incident power density of light (mW/cm^2). Maximum ABPE obtains for (BiVO4:In)-CNQD photoanode is ~0.34% (at 0.96 V vs RHE) which is ~5 fold higher than pristine BiVO4 photoanode (~0.062% at 1.02 V vs RHE).

Charge separation efficiency calculations were done in pristine $BiVO_4$ and the modified photoanodes in 0.1 M Na_2SO_3 and 0.5 M Na_2SO_4 electrolyte solution, as shown in **Figure 4.16 (b)**. It was calculated using the following **equation 4.2**

$$\eta_{sep} = \frac{J_{Na_2SO_3}}{J_{abs}} \tag{4.2}$$

where η_{sep} charge separation efficiency; $J_{Na_2SO_3}$ is the photocurrent density obtained using scavenger, and J_{abs} is photocurrent density after the complete conversion of absorbed photons.[42]The charge separation efficiency for (BiVO4:In)-CNQD, BiVO4:In, BiVO4-CNQD, and $BiVO_4$ photoanodes was found to be 46%, 37%, 25%, and 14% respectively confirming the enhancement in charge separation with the creation of oxygen vacancies by indium doping and CNQD loading in (BiVO4:In)-CNQD photoanode.

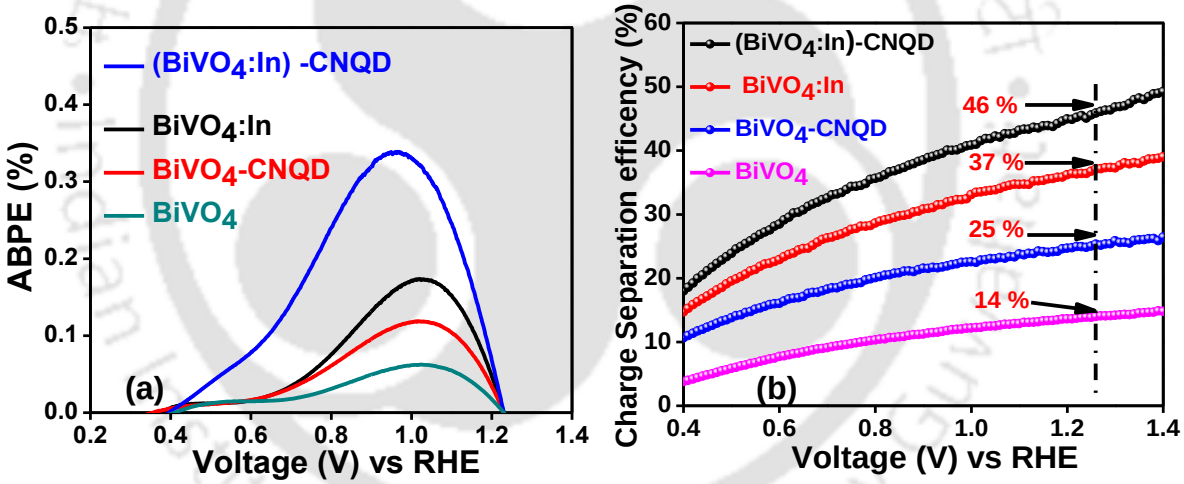

Figure 4.16. (a) Applied bias photon-to-current conversion efficiency (ABPE) curve of $BiVO_4$ and modified photoanodes. (b) Charge separation efficiency of $BiVO_4$ and all the modified photoanodes.

4.3.11 Electrochemical Impedance Spectroscopy (EIS) Analysis

Electrochemical impedance spectroscopy (EIS) measurements were done to understand the charge transfer resistance from bulk to the surface and at the semiconductor-electrolyte interface. **Figure 4.17 (a)** shows the Nyquist plot of each photoanode, under 1 Sun illumination at 1.23 V vs RHE in 0.5 M Na_2SO_4. Each curve consists of two semicircles, wherein a high-

frequency region corresponds to the charge transfer resistance inside the bulk (R_{bulk}) while the semicircle at the lower frequency region is assigned to charge transfer resistance at photoanode - electrolyte interface (R_{ct}). The diameter of the semicircle for ($BiVO_4$:In)-CNQD photoanode is smaller than the semicircle of pristine $BiVO_4$ photoanode indicating that with indium doping and CNQDs loading, there is an enhancement in charge separation in bulk inducing the faster charge transfer kinetics at photoanode ($BiVO_4$:In)-CNQD and electrolyte interface. To further confirm, the Nyquist plot of all the photoanodes were fitted to an equivalent circuit shown in the inset to **Figure 4.17 (a),** where R_s is the series resistance, C_{bulk} is the capacitance due to space charge region, C_{EE} is the capacitance due to the proposed Helmholtz layer.[43-44] **Table 4.1** shows the parameters deduced from the equivalent circuit. R_{bulk} for ($BiVO_4$:In)-CNQD photoanode was found to be 109.8 Ω while for pristine $BiVO_4$ photoanode it was 769.2 Ω, indicating an enhancement in the charge separation inside the bulk by indium doping and through the facilitated transport of charge carriers between $BiVO_4$:In and CNQDs in ($BiVO_4$:In)-CNQD photoanode. Similarly, the R_{ct} value decreases from 5116 Ω to 1109 Ω for ($BiVO_4$:In)-CNQD photoanode in comparison to pristine $BiVO_4$, representing an enhancement in charge transfer kinetics at ($BiVO_4$:In)-CNQD - electrolyte interface.

To check the change in charge carrier density, Mott-Schottky analysis was done, as shown in **Figure 4.17 (b)**. The slopes of all the photoanodes are positive, indicating that the electrons are the major charge carrier.[45,46] Charge Carrier density of the photoanodes were calculated by using **equation 4.3**

$$\frac{1}{C^2} = \frac{2}{A^2 N_D e \varepsilon \varepsilon_0}\left[V - V_{FB} - \frac{kT}{e}\right] \quad (4.3)$$

where V is the applied bias, A is the area of the photoanode, V_{FB} is the flat-band potential, N_D is the charge carrier density of photoanode, e is the charge of the electron, ε_0 is the permittivity in a vacuum, k is the Boltzmann constant, ε is the dielectric constant of the photoanode, C is

 Part of this chapter has been published in **J. Power Sources, 2020, 477, 229024**

the capacitance of the photoanode and T is the temperature. Charge carrier density of ($BiVO_4$:In)-CNQD photoanode was calculated to be 7.7 X 10^{20} (cm^{-3}), while for pristine $BiVO_4$, it was found to be only 1.36 X 10^{20} (cm^{-3}). There was a 5.5 fold enhancement in N_D value for ($BiVO_4$:In)-CNQD photoanode compare to the pristine $BiVO_4$ photoanode, which is in good agreement with the photocurrent density shown in **Figure 4.13 (a)**. The fitting parameter and carrier density of all the photoanode is shown in **Table 4.1.**

Table 4.1. Fitting parameter and carrier density of all the photoanode.

Photoanode	R_S (Ω)	R_{bulk} (Ω)	R_{ct}(Ω)	Carrier Density (cm^{-3})
($BiVO_4$:In)-CNQD	**15.0**	**109.8**	**1109**	**7.7 X 10^{20}**
$BiVO_4$:In	15.22	144.8	2070	4.47 X 10^{20}
BiVO4-CNQD	17.8	346.6	2321	2.20 X 10^{20}
$BiVO_4$	19.69	769.2	5166	1.36 X 10^{20}

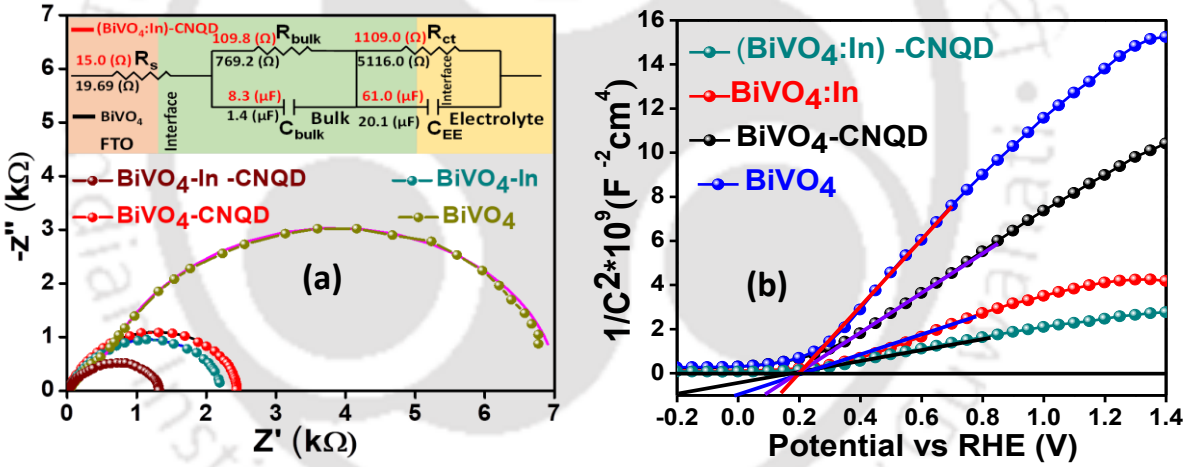

Figure 4.17. (a) Nyquist plot of all the photoanodes under 1 Sun illumination, inset shows the equivalent circuit used for fitting all the photoanode. (b) Mott−Schottky plot of $BiVO_4$ and modified photoanodes.

4.3.12 Stability and Faradaic Yield Measurements

To confirm that the current generated by ($BiVO_4$:In)-CNQD photoanode is solely due to the oxidation of water, Faradaic yields calculation was done, as shown in **Figure 4.18 (a)**. Here, chronoamperometry measurement of ($BiVO_4$:In)-CNQD photoanode was done in 0.5 M Na_2SO_4 at an applied potential of 1.23 V vs RHE under 1 Sun illumination of light for 1 h, and the gas was monitored through an online GC. A Faradaic yield of ~90% was obtained for

Part of this chapter has been published in **J. Power Sources, 2020, 477, 229024**

oxygen evaluation by (BiVO4:In)-CNQD photoanode, which confirms that the photocurrent value observed in **Figure 4.13 (a),** is purely due to water oxidation. **Figure 4.18 (a)**. also shows the amount of oxygen and hydrogen gas evolved by photoelectrochemical water splitting activity of (BiVO4:In)-CNQD photoanode. **Figure 4.18 (b)** shows the stability test of (BiVO4: In)-CNQD and pristine BiVO4 photoanode at an applied potential of 1.23 V vs RHE. After two hours of illumination, there was a ~4% decrease in photocurrent density of (BiVO4: In)-CNQD photoanode, while ~26% decrease in photocurrent density was observed for pristine BiVO4 photoanode. CNQDs, which have more resistance toward photo-corrosion, improve the stability of the photoanode.

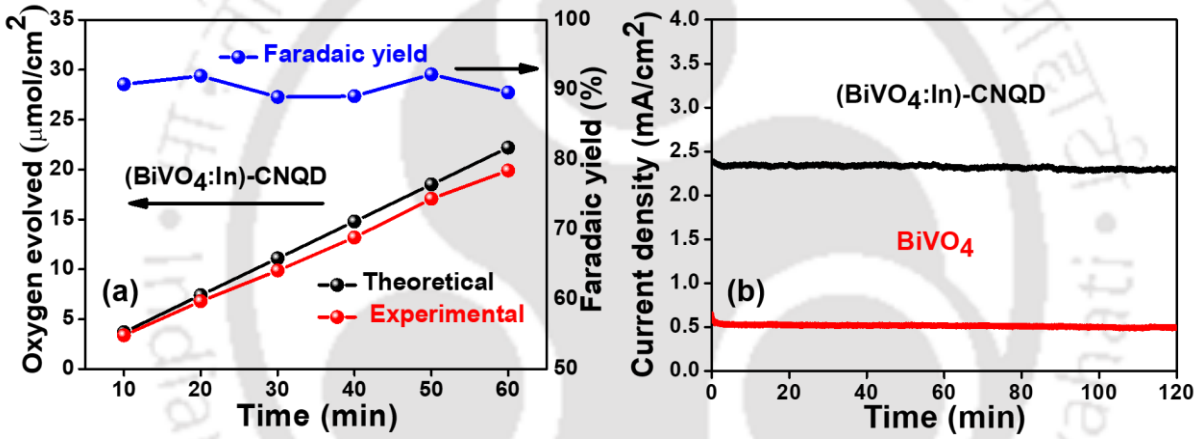

Figure 4.18. (a) Faradaic efficiency of (BiVO4:In)-CNQD photoanode and amount of gas evolved. (b) Stability of (BiVO4:In)-CNQD and pristine BiVO4 photoanode under 1 Sun illumination of light at an applied potential of 1.23 V vs RHE taking 0.5 M Na_2SO_4 as an electrolyte.

4.4 CONCLUSIONS

In summary, melamine was used for the first time for low-temperature green synthesis of CNQDs. Indium-doped BiVO4 with decahedron morphology was synthesis directly over FTO and CNQDs was incorporated to form type II heterojunction for enhanced water oxidation efficiency of (BiVO4:In)-CNQD photoanode. Indium doping induces oxygen vacancy in BiVO4, which improves surface kinetics, enhances the charge injection efficacy, thereby increasing the carrier density. It is also observed that indium doping makes the surface more

 Part of this chapter has been published in **J. Power Sources, 2020, 477, 229024**

hydrophilic, resulting in enhanced water oxidation efficiency. Dual modification of $BiVO_4$ shows an excellent photocurrent density of ~2.42 mA/cm^2 in the neutral medium with a solar to hydrogen conversion of 2.66% ascribed to an enhanced carrier density, efficient charge separation, and faster interfacial charge transport. Charge carrier density of 7.7 X 10^{20} cm^{-3} was achieved for ($BiVO_4$:In)-CNQD and 136 mV cathodic shift in on-set potential was achieved for ($BiVO_4$:In)-CNQD photoanode then the pristine $BiVO_4$ photoanode. Faradaic efficiency of ~90% was obtained for ($BiVO_4$:In)-CNQD photoanode proving ($BiVO_4$:In)-CNQD photoanode is stable and photocurrent generated is only due to the effect of illumination of light. The present work depicts that with doping and quantum dot loading, the water oxidation efficiency of $BiVO_4$ can be enhanced significantly.

4.5 REFERENCES

1. J. Joy, J. Mathew, S. C. George. *Int. J. Hydrogen Energy*, 2018, **43**, 4804.
2. J. K. Cooper, S. Gul, F. M. Toma, L. Chen, P.-A. Glans, J. Guo, J. W. Ager, J. Yano, I. D. Sharp. *Chem. Mater.*, 2014, **26**, 5365.
3. B. Lamm, B. J. Trze´sniewski, H. D¨oscher, W. A. Smith, M. Stek. *ACS Energy Lett.*, 2018, **3**,112.
4. H. Ullah, A.A. Tahir, T.K. Mallick. *Appl. Catal., B*, 2018, **224**, 895.
5. C. Zachaus, F. F. Abdi, L. M. Peter, R. van de Krol. *Chem. Sci.*, 2017, **8**, 3712.
6. S. Bai, J. Liu, M. Cui, R. Luo, J. He, A. Chen. *Dalton Trans.*, 2018, **47**, 6763.
7. X. Han, Y. Wei, J. Su, Y. Zhao. *ACS Sustainable Chem. Eng.*, 2018, **6**, 14695.
8. J. Liu, J. Li, M. Shao, M. Wei. *J. Mater. Chem. A*, 2019, **7**, 6327.
9. H. Jung, S.Y. Chae, H. Kim, B.K. Min, Y.J. Hwang. *Catal. Commun.*, 2016, **75**, 18.

10. X. Zhong, H. He, M. Yang, G. Ke, Z. Zhao, F. Dong, B. Wang, Y. Chen, X. Shi, Y. Zhou. *J. Mater. Chem. A*, 2018, **6**, 10456.

11. Z. Wang, S. Huang, Z. Jian, J. Yin, Z. Fei, Y. Zhang. *Res. Chem. Intermed.*, 2016, **42**, 4147.

12. Y. Wang, J. Sun, J. Li, X. Zhao. *Langmuir*, 2017, **33**, 4694.

13. H. Li, F. Zhao, J. Zhang, L. Luo, X. Xiao, Y. Huang, H. Ji, Y. Tong. *Mater. Chem. Front.*, 2017, **1**, 338.

14. S. D. Sun, X. F. Gou, S. S. Tao, J. Cui, J. Li, Q. Yang, S. H. Liang, Z. M. Yang. *Mater. Chem. Front.*, 2019, **3**, 597.

15. X. Y. Zhao, Y. Zhang, Y. N. Zhao, H. Q. Tan, Z. Zhao, H. F. Shi, E. B. Wang, Y. G. Li. *Dalton Trans.*, 2019, **48**, 6484.

16. Y. Zhao, R. G. Li, L. C. Mu, C. Li. *Cryst. Growth Des.*, 2017, **17**, 2923.

17. Y. Zhu, J. Ren, X. Yang, G. Chang, Y. Bu, G. Wei, W. Han, D. Yang. *J. Mater. Chem. A* 2017, **5**, 9952.

18. M. Huang, J. Bian, W. Xiong, C. Huang, R. Zhang. *J. Mater. Chem. A*, 2018, **6**, 3602.

19. C. Regmi, Y. K. Kshetri, T.-H. Kim, R. P. Pandey, S. W. Lee. *Mol. Catal.*, 2017, **432**, 220.

20. Zhan, Y.; Liu, Z.; Liu, Q.; Huang, D.; Wei, Y.; Hu, Y.; Lian, X.; Hu, C. *New J. Chem.*, 2017, **41**, 3930.

21. C. Regmi, Y. K. Kshetri, T.-H. Kim, R. P. Pandey, S. W. Lee. *Mol. Catal.*, 2017, **432**, 220.

22. F. Qiao, J. Wang, S. Ai, L. Li. *Sens. Actuators, B,* 2015, **216**, 418.

23. V. I. Merupo, S. Velumani, K. Ordon, N. Errien, J. Szade. *CrystEngComm*, 2015, **17**, 3366.

24. Z. Y. Jiang, Y. Y. Liu, T. Jing, B. B. Huang, X. Y. Zhang, X. Y. Qin, Y. Dai, M. H. Whangbo, *J. Phys. Chem., C*, 2016, **120**, 2058.

25. S. S. Mali, G. R. Park, H. Kim, H. H. Kim, J. V. Patil, C. K. Hong. *Nanoscale Adv*., 2019, **1**, 799.

26. X. Zhang, C. Jia, Y. Xue, P. Yang. *RSC Adv.*, 2017, **7**, 43888.

27. H. B. Li, Z. J. Yang, J. N. Zhang, Y. C. Huang, H. B. Ji, Y. X. Tong. *Appl. Surf. Sci.*, 2017, **423**, 1188.

28. Z. Y. Zhang, K. C. Liu, Z. Q. Feng, Y. N. Bao, B. Dong. *Sci. Rep.*, 2016, **6**, 19221.

29. Y. Tana, Z. Shua, J. Zhoua, T. Lib, W. Wanga, Z. Zhaoa. *Applied Catalysis B: Environmental*, 2018, **230**, 260.

30. F. M. Chang, S. Brahma, J. H. Huang, Z. Z. Wu, K. Y. Lo. *Sci. Rep.*, 2019, **9**, 905.

31. A. Sarkar, G. G. Khan. *Nanoscale*, 2019, **11**, 3414.

32. A. Roldan, M. Boronat, A. Corma, F. Illas. *Phys. Chem. C*, 2010, **114**, 6511.

33. M. Xu, P. Da, H. Wu, D. Zhao, G. Zheng. *Nano Lett.*, 2012, **12**, 1503.

34. X. Zhao, J. Hu, X. Yao, S. Chen, Z. Chen. *ACS Appl. Energy Mater.*, 2018, **1**, 3410.

35. Q. Yang, J. Du, J. Li, Y. Wu, Y. Zhou, Y. Yang, D. Yang, H. He. *ACS Appl. Mater. Interfaces*, 2020, **10**, 11625.

36. Y. Liu, Y. Yang, Q. Liu, Y. Li, J. Lin, W. Li, Li, J. *J. Colloid Interface Sci.*, 2018, **512**, 86.

37. C. J. Shi, X. L. Dong, J. W. Wang, X. Y. Wang, H. C. Maand, X. F. Zhang. *RSC Adv.*, 2017, **7**, 26717.

38. S. K. Pilli, T. G. Deutsch, T. E. Furtak, L. D. Brown, J. A. Turner, A. M. Herring. *Phys. Chem. Chem. Phys.* 2013, **15**, 3273.

39. X. An, T. Li, B. Wen, J. Tang, Z. Hu, L. Liu, J. Qu, C. Huang, H. Liu. *Adv. Energy Mater.*, 2016, **6**, 1502268.

40. P. Qiu, H. Yang, L. Yang, Q. Wang, L. Ge. *Electrochim. Acta*, 2018, **266**, 431.

41. S. Wang, T. He, J. H. Yun, Y. Hu, M. Xiao, A. Du, L. Wang. *Adv. Funct. Mater.*, 2018, **28**, 1802685.

42. X. Zhao, J. Hu, B. Wu, A. Banerjee, S. Chakraborty, J. Feng, Z. Zhao, S. Chen, R. Ahuja, T. C. Sum, et al. *J. Mater. Chem. A*, 2018, **6**, 16965.

43. J. Yang, C. X. Bao, T. Yu, Y. F. Hu, W. J. Luo, W. D. Zhu, G. Fu, Z. S. Li, H. Gao, F. M. Li, Z. G. Zou. *ACS Appl. Mater. Interfaces*, 2015, **7**, 26482.

44. Z. Xu, H. Wang, Y. Wen, W. Li, C. Sun, Y. He, Z. Shi, L. Pei, Y. Chen, S. Yan, Z. Zou. *ACS Appl. Mater. Interfaces*, 2018, **10**, 3624.

45. K. M. Alam, P. Kumar, P. Kar, U. K. Thakur, S. Zeng, K. Cui, K. Shankar. *Nanoscale Adv.*, 2019, **1**, 1460.

46. S. Feng, T. Wang, B. Liu, C. Hu, L. Li, Z.-J. Zhao, J. L. Gong. *Angew. Chem. Int. Ed.*, 2020, **59**, 2044.

CHAPTER 5

Hollow cuboidal $MnCo_2O_4$/nickel phosphate heterojunction: A promising oxygen evolution reaction electrocatalyst

This chapter shows the growth of hierarchical morphologies of complex metal oxides directly onto the substrate. Herein, it reports unique hollow-cuboidal $MnCo_2O_4$ (h-MCO) morphology that offers insights into the efficient charge-transfers and surface kinetics for oxygen evolution reaction. The h-MCO coupled nickel phosphate under alkaline conditions outperforms the benchmark catalyst RuO_2. High stability, low cost, and green synthesis procedure mark h-MCO/NiPi as one of the futuristic catalysts to be used in industrial applications.

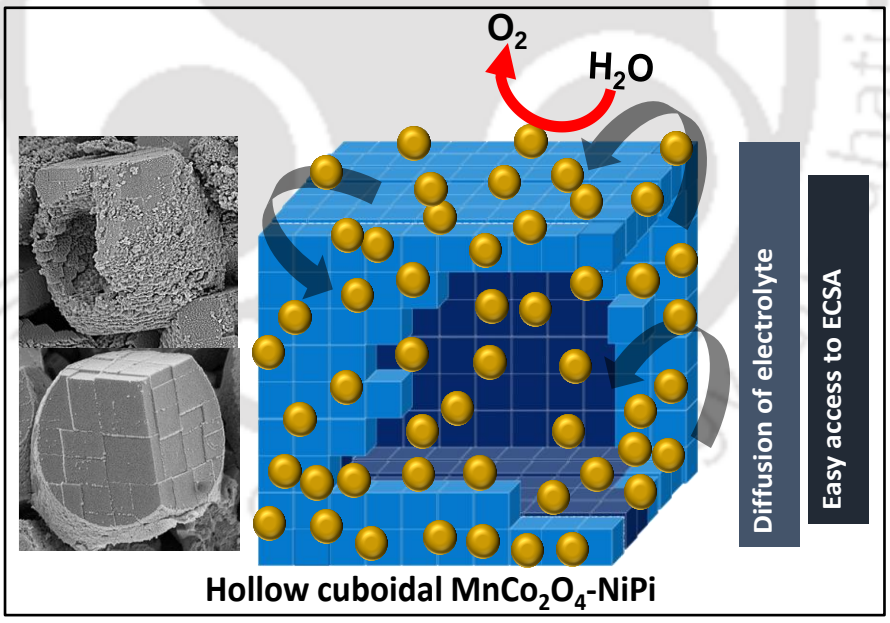

A. K. Shah, et al., **Chem. Commun.,** 2021, 57, 8027.

5.1 INTRODUCTION

The electrocatalytic water splitting technique is gaining popularity due to its great potential to fulfill future green and sustainable energy demands.[1] Material containing noble metals such as RuO_2 and IrO_2 show excellent results for oxygen evolution reaction (OER) in alkaline and acidic conditions[2,3]. However, due to high cost and scarcity, commercial implementation of these materials becomes economically inviable. Different strategies, such as doping and morphological tuning, are attempted to modify the existing materials such as metal sulphides, metal oxides, metal phosphides to improve the OER.[4-6] However, they underperform when compared to the precious metal counterparts reported.[7]

$MnCo_2O_4$, a stable spinel oxide, is gaining popularity in OER, due to its low cost, eco-friendliness, tunable morphological features, and high stability in alkaline medium. Previous reports show the use of Mn and Co based catalysts for OER. However, binary metal oxides such as $MnCo_2O_4$ show better conductivity than unitary MnO_2 and Co_3O_4 apart from their exceptional stability under alkaline conditions.[8] To date, the use of spinel $MnCo_2O_4$ showing OER activity is sparse in the literature.[9-11] One of the major drawbacks of $MnCo_2O_4$ is its high charge transfer resistance at the electrode-electrolyte interface, which affects its OER activity. The above-mentioned drawbacks can be addressed through morphological and surface modification of $MnCo_2O_4$. Popular metal phosphates such as $Ni_3(PO_4)_2$ (NiPi) and $Co_3(PO_4)_2$ (CoPi) are used as catalysts in electrochemical water oxidation.[12, 13] However NiPi is preferred compared to CoPi due to its stability in harsh pH conditions and rapid redox process ($Ni^{2+} \leftrightarrow Ni^{3+}$) which helps in achieving higher reaction kinetics.[13] Phosphate group in NiPi also facilitates the adsorption, thereby enhancing OER activity of $MnCo_2O_4$ composite.[14]

Part of this chapter has been published in **Chem. Commun.,** 2021,57, 8027

Recent efforts towards increasing the number of active sites in $MnCo_2O_4$ are by its morphological tuning. The $MnCo_2O_4$ with proper morphology can become an excellent candidate for electrocatalytic water splitting.[15,16] However, reported literature on $MnCo_2O_4$ mainly focuses on synthesizing it in powder form through the hydrothermal procedure, which was later drop-casted over glassy carbon.[16,17] Recent reports on the synthesis of $MnCo_2O_4$ over nickel foam and titanium mesh reported good efficacy, but due to its high price and issues of reusability under harsh alkaline conditions, are not deemed suitable for commercial implementation.[10,18]

In the present manuscript, we intended to overcome the substrate deposition issues by growing the hollow cuboidal structures of $MnCo_2O_4$ directly onto the FTO substrate. We have utilized a green and simple synthetic route involving hydrothermal conditions to grow hollow cuboidal structures using urea and NH_4F to achieve high-quality and stable films for OER performance. Further, to overcome the poor charge transfer kinetics of h-MCO, we have electrodeposited nickel phosphate over the h-MCO surface. Surface modification of h-MCO improves the overpotential required for OER activity apart from improving the charge transfer kinetics and turnover frequency in h-MCO/NiPi. As synthesized h-MCO/NiPi anode displays excellent long-term stability in alkaline conditions and shows good OER activity for its use in large-scale application to meet the future energy demand.

5.2 EXPERIMENTAL SECTION

5.2.1 Synthesis and Fabrication Protocol of h-MCO

Step-by-step fabrication of h-MCO/NiPi electrode is shown in **Scheme 5.1**. The h-MCO was synthesized over FTO through a hydrothermal route.[18] $Mn(NO_3)_2.4H_2O$ (2 mmol), $Co(NO_3)_2.6H_2O$ (4 mmol), urea (1.44 g), and NH_4F (0.37 g), were dissolved in 70 ml deionized water, and the solution was kept under stirring for 2 h. FTO in a teflon vessel was kept facing

Part of this chapter has been published in **Chem. Commun.,** 2021,57, 8027

up in a 100 ml teflon-lined autoclave. The area of FTO exposed to the solution was controlled by putting polyimide tape over the FTO which can sustain very high temperature and pH. Only 1 x 1 cm^2 of FTO was kept exposed to the solution. The above solution mixture was then transferred into the autoclave and kept in an oven at 150 °C for 24 h. The pink-colored film was formed over FTO and was washed with deionized water and ethanol. After drying at 100 °C, it was transferred to a muffle furnace and calcined at 450 °C for 3 h to form black-colored hallow cuboidal $MnCo_2O_4$.

5.2.2 Deposition of NiPi Over h-MCO (h-MCO/NiPi)

NiPi layer was deposited over h-MCO through the electrodeposition technique.[19] In a typical synthetic procedure $Ni(NO_3)_2.6H_2O$ (3 mmol) and $NaH_2PO_4.H_2O$ (2 mmol) were dissolved in 300 ml 1:1 (v/v) water and ethanol mixture solution and the solution was kept stirring for 1 h. The three electrode cell (Ag/AgCl as a reference, Pt as a counter, and FTO/ h-MCO as a working electrode) was used for deposition of NiPi layer over h-MCO. Cyclic voltammetry was performed at the scan rate of 10 mV/sec within the voltage range of -1.2 V to 0.4 V for different number cycles. The sample was then washed with deionized water followed by drying overnight at 100 °C.

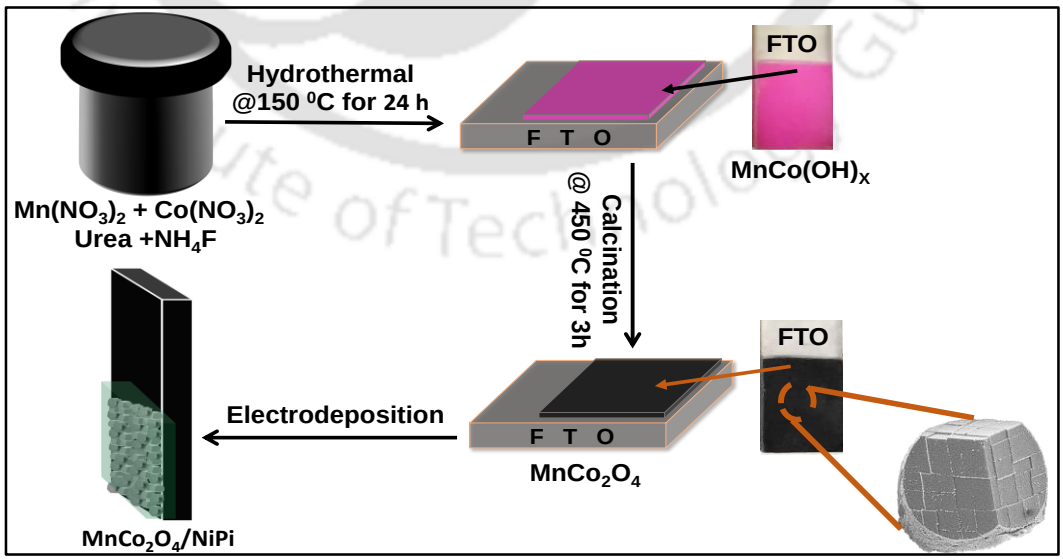

Scheme 5.1 Step-by-step procedure for the green and cost-effective fabrication of h-MCO/NiPi electrode directly over FTO.

 Part of this chapter has been published in **Chem. Commun.,** 2021,57, 8027

5.3 RESULTS AND DISCUSSION

5.3.1 Powder X-Ray Diffraction (PXRD) Analysis

To confirm the formation and purity of the respective catalysts powder X-ray diffraction (PXRD) analysis was done. **Figure 5.1** shows the PXRD pattern of h-MCO, NiPi, and h-MCO/NiPi electrodes.[20,21] Diffraction peaks of h-MCO were indexed to the corresponding (hkl) planes, confirming the formation of h-MCO, with no detectable impurity (JCPDS Card No - 00-023-1237). PXRD of NiPi, shows a broad peak in the range, 2Θ (15-40) confirming the formation and amorphous NiPi. In the PXRD pattern of h-MCO/NiPi, all the peaks of h-MCO were indexed. Due to the amorphous nature of NiPi, the diffraction peak of NiPi is not detectable in the composite.

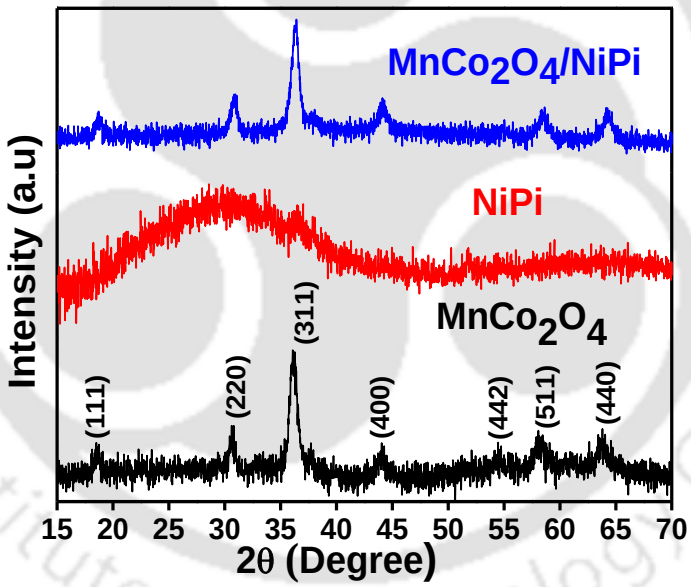

Figure 5.1. Powder X-ray diffraction (PXRD) patterns of spinel h-MCO, amorphous NiPi, and h-MCO/NiPi electrodes reveal the formation and purity of the respective catalysts.

5.3.2 Raman Spectroscopy Analysis

To confirm the formation of composite, Raman spectra of h-MCO, NiPi, and h-MCO/NiPi were recorded, shown in Figure **5.2**. Raman bands at 186 cm^{-1}, 476 cm^{-1}, 522 cm^{-1}, and 675 cm^{-1} correspond to F_{2g}, E_g, F_{2g}, and A_{1g} modes of spinel h-MCO, respectively. In the Raman spectrum of NiPi, a single band was observed at 920 cm^{-1}, corresponding to symmetric

Part of this chapter has been published in **Chem. Commun.,** 2021,57, 8027

O−P−O vibrational stretching mode which indicates the formation of (PO_4^{3-}). The band at 951 cm^{-1} for h-MCO/NiPi composite, confirms the presence of PO_4^{3-} in h-MCO/NiPi catalyst, a shift in PO_4^{3-} towards higher binding energy indicates an electronic interaction between h-MCO and NiPi in h-MCO/NiPi.[22,23]

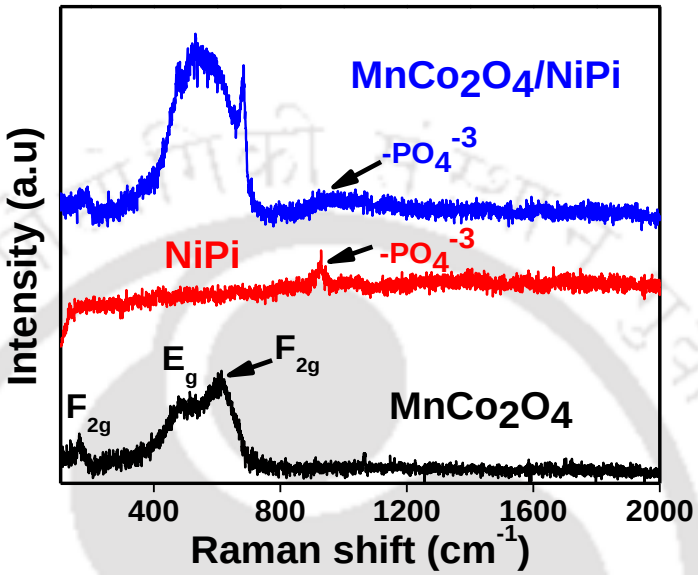

Figure 5.2. Laser Raman spectra of spinel h-MCO, NiPi, and h-MCO/NiPi, confirm the formation of electrocatalysts. A shift in PO_4^{3-} towards higher binding energy indicates a good electronic interaction among h-MCO and NiPi in h-MCO/NiPi composite. Signature symmetric O−P−O vibrational stretching mode in the bare and the composite is indicative of nickel phosphate presence.

5.3.3 Morphological and Structural Analysis

The Field emission scanning electron microscopy (FESEM) images (**Figure 5.3 (a,b)**) show h-MCO grown directly over FTO substrate. Inset to **Figure 5.3 (a)** shows the magnified image of h-MCO. The hollow cuboidal structure provides the more exposed active surface area with better accessibility of electrochemically active sites to the electrolyte ensuring adequate contact between electrolyte and h-MCO for the redox process to happen. **Figure 5.3 (b)** shows the magnified image of the cuboidal side of the hollow cuboidal structure, suggesting that the hollow cuboidal structure was formed by the integration of blocks, which maintains good electrical contact and provides structural stability in h-MCO. To show the deposition and good

contact between h-MCO and the substrate, we have performed a cross-sectional FESEM of the h-MCO/NiPi. As can be seen from **Figure 5.3 (c),** there is nice growth of the h-MCO onto the substrate which leads to better ohmic contact during the electrocatalytic measurements.

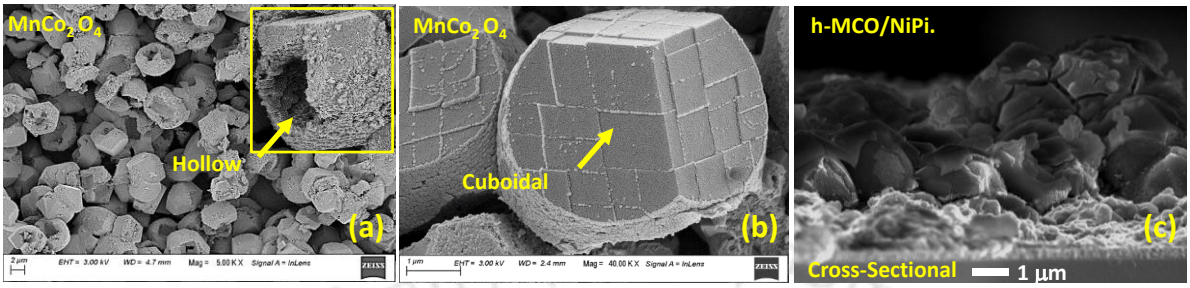

Figure 5.3. (a, b) FESEM images of h-MCO. (c) Cross-sectional FESEM image of the composite.

The high-resolution transmission electron microscopy (HRTEM) image of h-MCO is shown in **Figure 5.4. (a)**. The *d*- spacing of lattice fringes was calculated to be 0.47 nm, which matches well with the (111) crystalline plane of h-MCO as shown in **Figure 5.1**. **Figure 5.4. (b)** shows the Field emission transmission electron microscope (FETEM) image of the composite h-MCO/NiPi, which confirms the electrodeposited layer of NiPi over h-MCO in the composite.

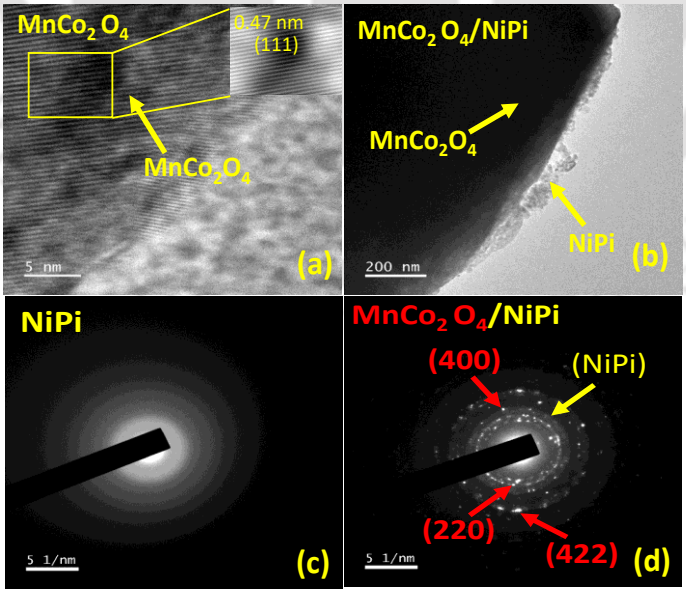

Figure 5.4. (a) HRTEM image of h-MCO. (b) FETEM image of h-MCO/NiPi. Selected area electron diffraction (SAED) patterns of (c) NiPi, (d) h-MCO/NiPi.

 Part of this chapter has been published in **Chem. Commun.,** 2021,57, 8027

To further confirm the formation NiPi and the composite, we have performed a selected area electron diffraction (SAED) analysis. **Figure 5.4 (c)** shows the characteristic amorphous nickel phosphate ring, confirming the formation of amorphous NiPi. SAED pattern of h-MCO/NiPi is shown in **Figure 5.4 (d)**, which were assigned to the (220), (400), and (422) planes of h-MCO. Additionally, a characteristic NiPi ring was also observed confirming the formation of the composite.

To confirm the presence and uniform distribution of all the elements in the composite, FESEM energy-dispersive X-ray spectroscopic (EDX) elemental mapping analysis of h-MCO/NiPi was done. **Figure 5.5 (a-f)** confirms the presence and uniform distribution of all the elements present in the composite.

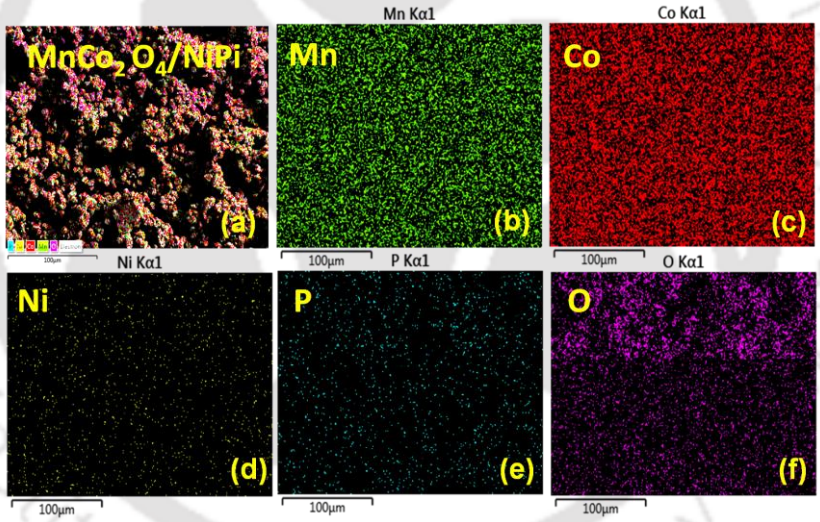

Figure 5.5. (a-f) FESEM energy-dispersive X-ray spectroscopic (EDX) elemental mapping image of h-MCO/NiPi. Elemental mapping shows the uniform distribution of each element present in h-MCO/NiPi throughout the composite.

5.3.4 FTIR Spectra Analysis

Fourier-transform infrared (FTIR) spectroscopy measurement was performed to determine the formation of NiPi and the composite, shown in **Figure 5.6**. The presence of two strong bands at 560 cm^{-1} and 640 cm^{-1} was attributed to the vibrational bending modes of Mn-O and Co-O in the spinel $MnCo_2O_4$, respectively.[24] In the FTIR spectra of NiPi, vibrational

bands of PO_4^{-3} anion are observed around 1035 cm^{-1}, 1112 cm^{-1} indicating the formation of NiPi.[25] Further in the FTIR spectra of h-MCO/NiPi, vibrational bending modes of manganese oxide and cobalt oxide of spinel $MnCo_2O_4$ and vibrational bands of PO_4^{-3} anion were observed, which confirms the formation of the composite.

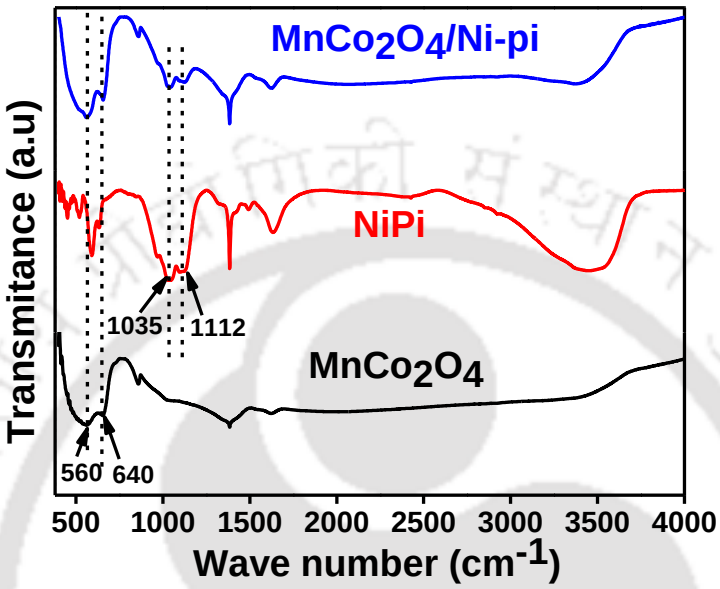

Figure 5.6. Fourier-transform infrared (FTIR) spectra of h-MCO/NiPi, h-MCO, and NiPi.

5.3.5 X-Ray Photoelectron Spectroscopy (XPS) Analysis

To investigate the chemical composition and change in the electronic structure environment around the elements, X-ray photoelectron spectroscopy (XPS) measurements were carried out. The survey spectra in **Figure 5.7 (a)**, confirm the presence of all the elements in $MnCo_2O_4$/NiPi, $MnCo_2O_4$, and NiPi electrodes. **Figure 5.7 (b)** shows the Mn 2p core level spectra of h-MCO/NiPi and bare h-MCO. Peaks at binding energy 641.36 eV and 652.27 eV corresponds to ($2p_{3/2}$ and $2p_{1/2}$) of Mn^{2+} and peaks at 643.22 eV and 654.35 eV corresponds to ($2p_{3/2}$ and $2p_{1/2}$) of Mn^{3+}. De-convoluted peaks of bare h-MCO at 640.90 eV and 652.14 eV corresponds to ($2p_{3/2}$ and $2p_{1/2}$) of Mn^{2+}, peaks at 642.59 eV and 654.22 eV corresponds to ($2p_{3/2}$ and $2p_{1/2}$) of Mn^{3+}, whereas, peaks at binding energies 646.15 eV and 645.64 eV were assigned to satellite peaks corresponding to Mn 2p of h-MCO/NiPi and bare h-MCO, respectively.[26,18] Shift in the peak position towards higher binding energy in the composite is

TH-2636_166122040
Part of this chapter has been published in **Chem. Commun.,** 2021,57, 8027

observed compared to its bare counterpart, which indicates a good electronic interaction among h-MCO and NiPi in the modified electrode. **Figure 5.7 (c)** shows the Co 2p core level spectra of h-MCO/NiPi and h-MCO, peaks at 780.22 eV and 795.67 eV corresponds ($2p_{3/2}$ and $2p_{1/2}$) to Co^{2+}, and the peaks at 783.22 eV and 797.88 eV corresponds to ($2p_{3/2}$ and $2p_{1/2}$) of Co^{3+} of h-MCO/NiPi electrode. Two peaks at binding energies 787.48 eV and 803.30 eV are the satellite peaks of Co 2p h-MCO/NiPi electrode. Similarly, peaks at 780.19 eV and 795.42 eV corresponds to Co^{2+} and the peaks at 782.26 eV and 797.7 eV corresponds to Co^{3+} of h-MCO electrode. [18, 27,28] The two peaks at 786.66 eV and 803.15 eV are the satellite peaks of Co 2p in h-MCO. **Figure 5.7 (d)** shows the core level spectra of Ni 2p with peaks at 856.71 eV and 875.02 eV corresponds to $2p_{3/2}$ and $2p_{1/2}$ respectively, in h-MCO/NiPi and peaks at 856.32 and 874.38 eV corresponds to $2p_{3/2}$ and $2p_{1/2}$, respectively, in NiPi, confirming the presence of nickel in Ni^{2+} state in both the catalysts. Peaks at 862.41 eV and 881.08 eV corresponds to the satellite peaks of Ni^{2+} $2p_{3/2}$ and Ni^{2+} $2p_{1/2}$, respectively, in h-MCO/NiPi, and peaks at 861.74 eV and 880.36 eV corresponds to the satellite peaks of Ni^{2+} $2p_{3/2}$ and Ni^{2+} $2p_{1/2}$, respectively, in NiPi.[29] **Figure 5.7 (e)** shows the core level XPS spectra of P 2p for h-MCO/NiPi and NiPi, it de-convoluted to give $2p_{3/2}$ and $2p_{1/2}$ peaks at 133.25 eV and 134.10 eV in the composite, and at binding energies 133.12 eV and 134.07 eV in the bare NiPi electrode. It confirms the presence of phosphorus in phosphate form in both electrodes.[28] **Figure 5.7 (f)** shows O 1s core level spectra of bare h-MCO, NiPi, and h-MCO/NiPi catalysts. Peaks at binding energies 529.86 eV, 531.28 eV, and 532.27 eV corresponds to lattice oxygen (O_L (metal-oxygen), oxygen vacancy (O_V) and adsorbed oxygen ($O_{ads.}$) respectively of bare h-MCO. Peaks at binding energies 530.79 eV and 532.28 eV corresponds to O_L (Ni-O) and $O_{ads.}$ respectively of NiPi. Peaks at binding energies 530.54 eV, 531.00 eV, 531.56 eV and 532.28 eV corresponds to O_L(metal-oxygen), O_L(Ni-O), O_V and $O_{ads.}$ respectively, of h-MCO/NiPi.[29,30]

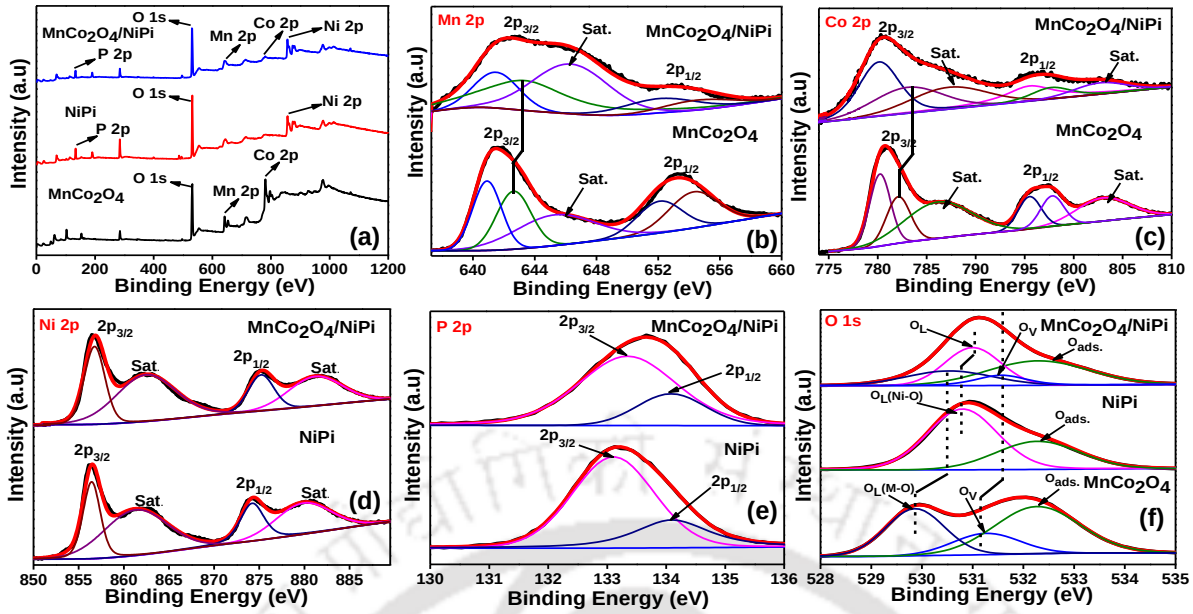

Figure 5.7. (**a**) XPS survey spectra of h-MCO/NiPi, pristine NiPi, and h-MCO. Core level XPS spectra (b) Mn 2p, (c) Co 2p, of h-MCO/NiPi and h-MCO. Core level XPS spectra (d) Ni 2p of $MnCo_2O_4$/NiPi and bare NiPi. (e) P 2p core level spectra of h-MCO/NiPi, and NiPi. (f) O 1s core level spectra of h-MCO/NiPi, NiPi, and h-MCO.

5.3.6 Atomic Absorption Spectroscopy

Atomic absorption spectroscopy (AAS) measurement was done to quantify the amount of h-MCO and NiPi loading in the h-MCO/NiPi electrode. In a typical experiment, 1x1 cm^2 of h-MCO/NiPi electrode was digested in 7ml aqua regia (1:3, HNO_3:HCl) and 2 ml of sample solution was further diluted to 10 ml in deionized water. The sample solution was then filtered (using 0.22 μm syringe filter) and AAS measurement was done to determine the amount of h-MCO and NiPi loading in the composite, shown in **Table 5.1**.

Table 5.1. Showing amount of H-MCO and NiPi loaded in the modified electrode h-MCO/NiPi.

Electrocatalyst	Mass Loading (mg/cm^2)
h-MCO	1.26
NiPi	0.12

5.3.7 Electrochemical Measurements

1.26 mg/cm^2 and 0.12 mg/cm^2 of h-MCO and NiPi respectively, were loaded in h-MCO/NiPi which was determined through Atomic absorption spectroscopy (AAS)

Part of this chapter has been published in **Chem. Commun.,** 2021,57, 8027

measurement. **Figure 5.8 (a)** shows the polarization curves of bare h-MCO, NiPi, RuO_2 and h-MCO/NiPi electrodes displaying their respective OER behaviours. The linear sweep voltammetry (LSV) measurements were done at a scan rate of 1mV/sec and the performance of each electrode was investigated by measuring the overpotential to drive current density to 10mA/cm^2 (η_{10}). In **Figure 5.8 (a),** the η_{10} for bare h-MCO was found to be 380 mV, while for bare nickel phosphate, η_{10} was found to be 330 mV. When h-MCO was modified with electrodeposited NiPi, the η_{10} value improved to an efficient 230 mV. When compared with the benchmark catalyst RuO_2 **(**(η_{10}) = 290 mV**),** under similar experimental conditions, the modified h-MCO/NiPi electrode shows 60 mV improved overpotential value. **Figure 5.8 (b)** shows the optimised LSV curves of h-MCO/NiPi electrode at different cyclic voltammetry cycles of electrodeposited NiPi over h-MCO. h-MCO/NiPi electrode with five voltammetry cycles showing the best OER activity. To examine the reproducibility of the modified electrode, three consecutive linear sweep voltammetry measurement of the same h-MCO/NiPi electrode was carried out. The three consecutive measurements of h-MCO/NiPi, shown in **Figure 5.8 (c)** confirm the reproducibility of OER activity by the modified electrode.

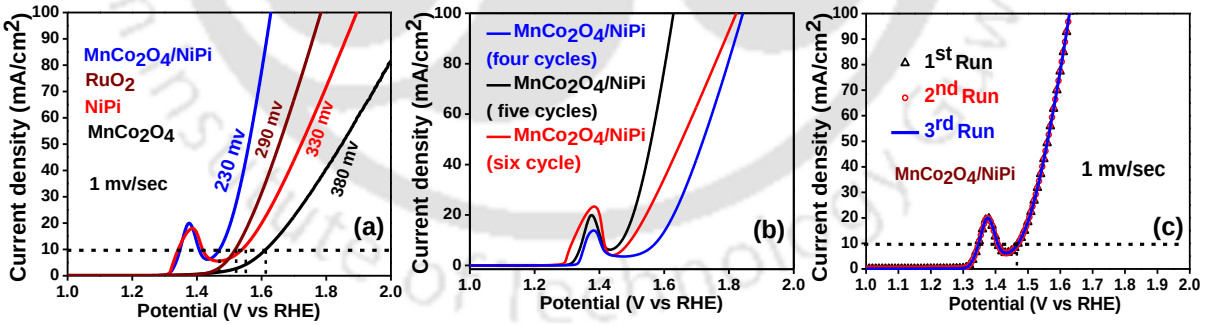

Figure 5.8. (a) Linear sweep voltammetry (LSV) plot of h-MCO/NiPi, h-MCO, NiPi, and RuO_2 respectively. (b) Shows the optimized current density of $MnCo_2O_4$/NiPi electrode due to oxygen evolution reaction activity (OER), $MnCo_2O_4$/NiPi electrode with five cyclic voltammetry cycles is the most efficient electrode for activity among all. (c) Reproducibility test of $MnCo_2O_4$/NiPi.

To further understand the OER kinetics during the oxygen evolution, Tafel slopes of the components were calculated from the LSV curve (**Figure 5.8 (a)**) of respective

electrocatalysts as shown in **Figure 5.9 (a)**. The Tafel slope for h-MCO/NiPi electrode was calculated to be 57 mV/dec, while for bare h-MCO it was calculated to be 203 mV/dec, an indication of faster surface kinetics with nickel phosphate modification[11]. It is noteworthy to mention that the reported composite is having faster kinetics compared to the benchmark RuO_2 catalyst, which shows a Tafel value of 78 mV/dec. To determine the change in charge transfer resistance (R_{ct}) of h-MCO with deposition of NiPi over h-MCO, electrochemical impedance spectroscopy measurements were done at 1.6 V vs RHE. R_{ct} value calculated for h-MCO/NiPi from Nyquist plot (**Figure 5.9 (b)**) was 4.43 Ω, while for the bare h-MCO and bare NiPi the values were 22.38 Ω and 6.58 Ω respectively. Hence it is clear that with the deposition of NiPi over h-MCO, lower R_{ct} is observed, which results in faster charge transfer at the h-MCO/NiPi and electrolyte interface.[31]

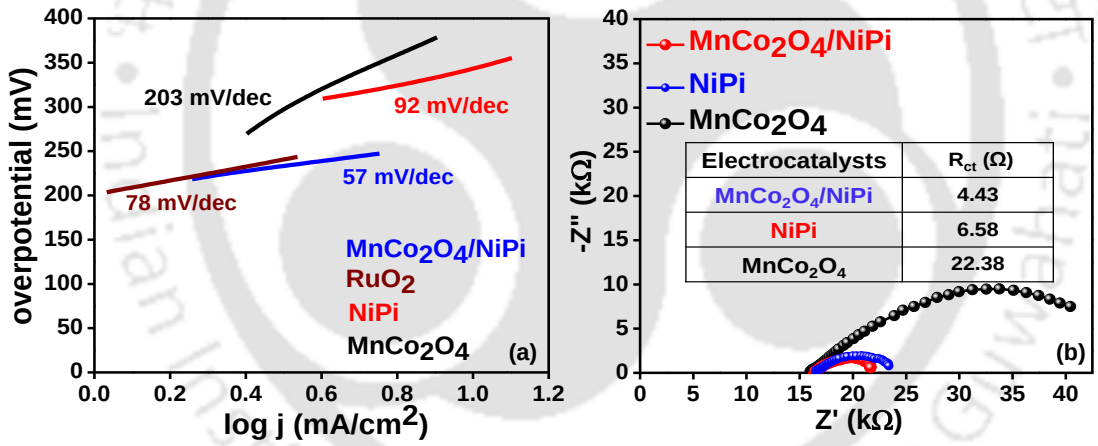

Figure 5.9. (a) Tafel plots, of h-MCO/NiPi, h-MCO, NiPi, and RuO_2 respectively. (b) Nyquist plot of h-MCO/NiPi, h-MCO, and NiPi.

To determine the change in the oxidation state of metals present in the electrocatalyst on the application of a potential across the electrodes, cyclic voltammetry measurement (CV) was done. **Figure 5.10 (a)** shows, on the application of a potential across bare h-MCO, Co^{2+} is being oxidised to Co^{3+} and Mn^{3+} to Mn^{4+} and vice-versa. **Figure 5.10 (b)** shows the cyclic voltammetry of the h-MCO/NiPi electrode, which shows the formation of the redox couple Ni^{2+}/ Ni^{3+}.

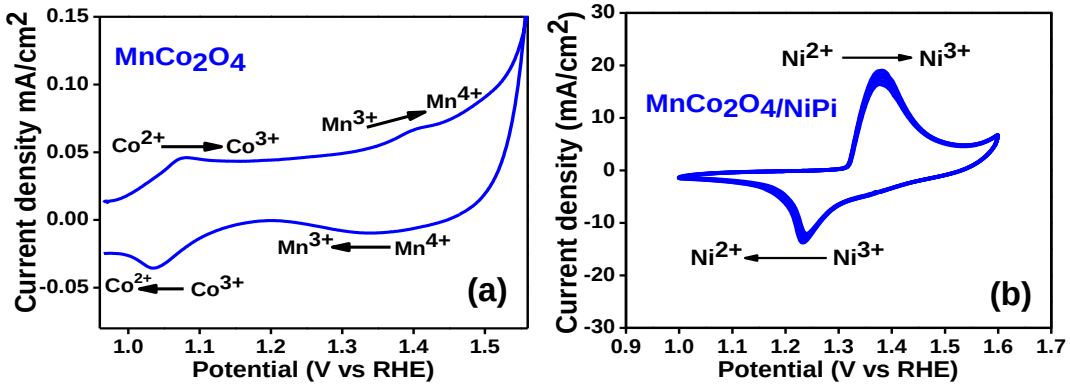

Figure 5.10 (a) Cyclic voltammogram showing (Co^{2+}/ Mn^{3+} ↔ Co^{3+}/Mn^{4+}) redox cycle in bare h-MCO. (b) Cyclic voltammogram showing (Ni^{2+} ↔ Ni^{3+}) redox process.

To determine the electrochemical active surface area (ECSA), which is indicative of the number of electrochemically active sites in an electrocatalyst, cyclic voltammetry measurements of h-MCO and h-MCO/NiPi electrodes were done (shown in **Figure 5.11 (a, b)**) in range of 0.0 - 0.06 V vs Ag/AgCl (non-faradic range), and also away from metal cations redox features (**Figure 5.10 (a, b)**) at different scan rates of 1-6 mV/sec.

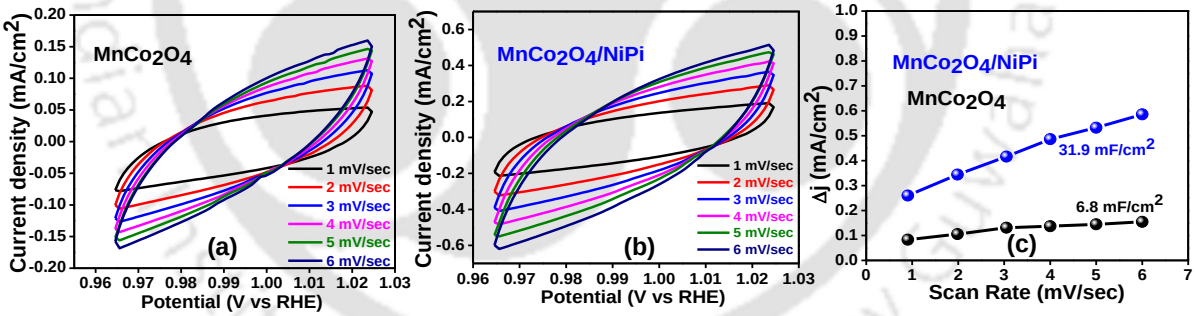

Figure 5.11. Cyclic voltammetry plots at different scan rates under alkaline conditions in a three electrode electrochemical cell in a non-faradaic region of the respective catalysts (a) Bare h-MCO, (b) h-MCO/NiPi composite. (c) C_{dl} plot of h-MCO/NiPi and bare h-MCO.

Double layer capacitance (C_{dl}), which gives a direct estimate of ECSA value, was calculated from the plot of the difference in current density (j_{anode} - $j_{cathode}$ at 1.0 V vs RHE) of h-MCO/NiPi and h-MCO electrodes against the scan rate, where C_{dl} is equal to half of the slope value. The C_{dl} value (**Figure 5.11 (c**) for h-MCO/NiPi electrode was calculated to be 31.9

mF/cm^2 while for bare h-MCO it was found to be 6.8 mF/cm^2.[32] The modified catalyst, h-MCO/NiPi shows a ~4-fold increase in C_{dl} value confirms enhancement in electrocatalytic activity of the modified catalyst.

To further understand the intrinsic activity of the electrocatalyst, turnover frequency (TOF) was evaluated as shown in **Figure 5.12**.[32,33] It determines the number of oxygen molecules formed from the active sites of the catalyst per unit time, the turnover frequency (TOF) was calculated at an operating potential of 1.53 V vs RHE. But to determine the TOF for OER, first, the concentration of active sites (N_S) needs to be quantified. The oxidation current in a CV measurement of the redox species was plotted against different scan rates, where they show a linear relationship, the slope of which can be calculated using **equation 5.1**.

$$\text{Slope}\left(\frac{J_{anodic}}{Scan\ rate}\right) = n^2F^2AN_S/4RT \qquad (5.1)$$

Where n, R, and T are the number of electrons transferred, ideal gas constant, and absolute temperature, respectively.

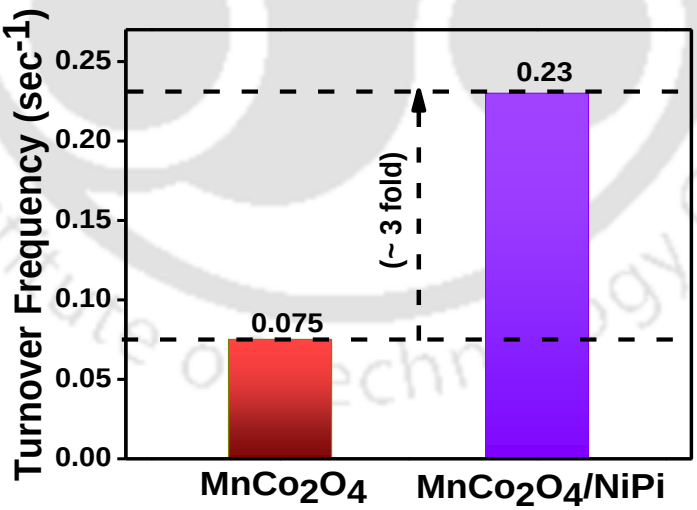

Figure 5.12. Turnover frequency (TOF) calculations show ~3-fold enhancement in TOF of h-MCO/NiPi in comparison to its bare counterpart, h-MCO.

TOF then can be calculated using **equation 5.2**.

$$\text{TOF} = \frac{J \times A}{n \times F \times N_S} \qquad (5.2)$$

where J, A, n, F, and N_S are, the current density at particular overpotential (A/cm^2), the surface area of the electrocatalyst (cm^2), number of electrons transferred to evolve a molecule of O_2, Faraday constant (96458 C/mol), and concentration of active sites of the electrocatalysts (mol/cm^2). The surface modified h-MCO/NiPi electrode shows a ~3-fold enhancement in TOF (0.23/sec) than its bare counterpart h-MCO (0.075/sec), which is due to faster OER activity, and faster charge transfer at the working electrode and electrolyte interface.

5.3.8 Faradaic Yield and Stability Measurements

To understand, whether the gas evolved during the process is solely due to water oxidation and not due to the possible side reactions/products, Faradaic yield measurements were performed. **Figure 5.13 (a)** shows the Faradaic yield of the h-MCO/NiPi electrode along with the amount of gas evolved during the electrocatalytic process.[34] Faradaic yield measurements were performed chronoamperometrically in 1 M KOH at an applied potential of 1.46 V vs RHE for 2 h and the gas evolved was monitored through an online-GC. The Faradaic yield was calculated using **equation 5.3** along with the amount of gas evolved (calculated using **equation 5.4**) during the electrocatalytic process. The equation to calculate the Faradaic yield is

$$\text{Faradaic yield} = \frac{(\text{amount of gas evolved measured experimentally})}{(\text{amount of gas calculated theoretically})} \quad (5.3)$$

The amount of gas evolved was calculated using the formula

$$Amount\ of\ gas\ evolved = \frac{(J.t)}{(n.F)} \quad (5.4)$$

Where J is the current density (A/cm^2), t is the time (sec), n is the number of moles charge required to produce one mole of gas, and F is the Faraday constant 96485(C (eN_A)). The faradic yield of ~98% was obtained for h-MCO/NiPi electrocatalyst, which confirms that the current density obtained in **Figure 5.8 (a)** is solely due to the OER activity of the catalyst.

 Part of this chapter has been published in **Chem. Commun.,** 2021,57, 8027

Another critical parameter to validate the goodness of electrochemical performance is operational stability. **Figure 5.13 (b)** displays the stability tests for both composite h-MCO/NiPi and bare h-MCO electrodes at 1.6 V vs RHE in 1 M KOH solution. h-MCO/NiPi maintains its electrocatalytic activity till 30 h, without any significant decay in current density. Inset in **Figure 5.13 (b)** shows the LSV curve of the h-MCO/NiPi electrode before and after the stability test, illustrating no significant loss of activity, confirming the stability of the electrodes.

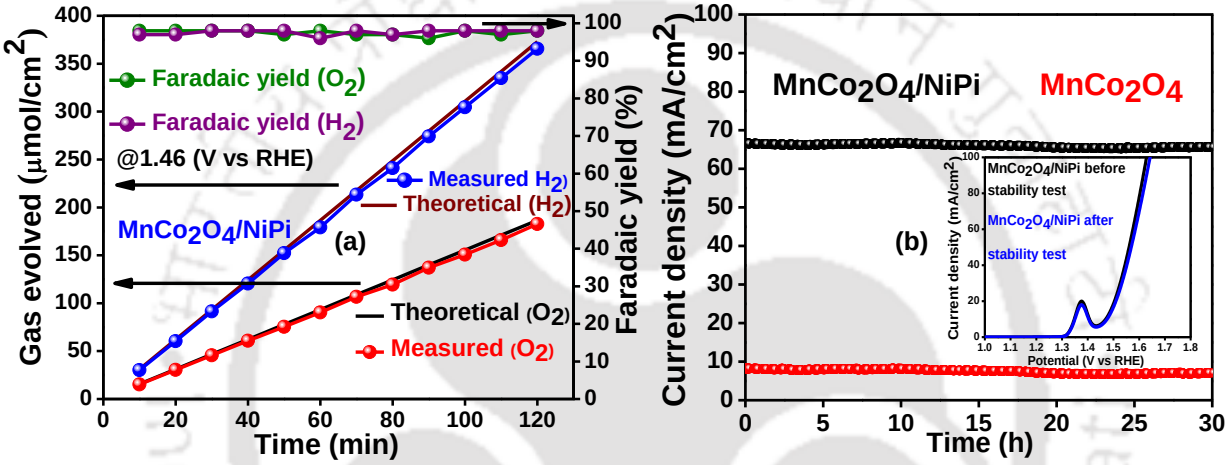

Figure 5.13. (a) The faradaic yield of h-MCO/NiPi and the amount of gases evolved. (b) Stability test of h-MCO/NiPi and bare h-MCO electrodes.

Further to check the stability, 1000 cycles of CV measurement for h-MCO/NiPi and h-MCO were done at the scan rate of 10 mV/sec in the non-faradaic region (0.0 - 0.06 V vs Ag/AgCl), as shown in **Figure 5.14 (a, b). Figure 5.14 (c, d)** shows the current density of the h-MCO/NiPi and bare h-MCO measured before and after 1000 cycles of CV, which displays the insignificant change in current density confirming the stability of both the electrodes.

TH-2636_166122040

Part of this chapter has been published in **Chem. Commun.**, 2021,57, 8027

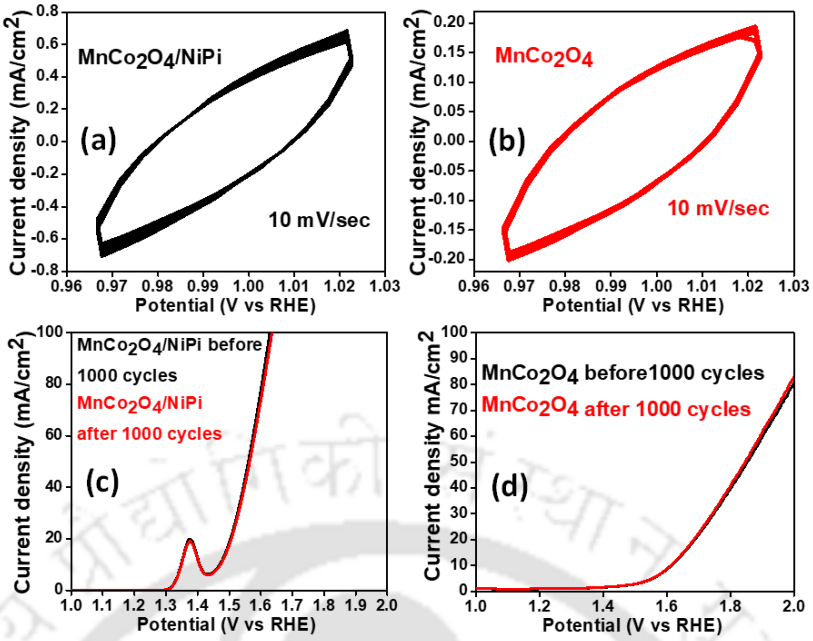

Figure 5.14. To check the stability of the $MnCo_2O_4$/NiPi catalyst and its bare counterpart. (a, b) 1000 cycles of cyclic voltammetry of $MnCo_2O_4$ and $MnCo_2O_4$/NiPi at the scene rate of 10 mV/sec in a non-faradic region. (c, d) The current density of composite $MnCo_2O_4$/NiPi and bare $MnCo_2O_4$ measured before and after 1000 cycles of CV displays a very insignificant change in current density which confirms the stability of both the electrodes.

5.3.9 Possible Mechanism

To further understand the enhanced OER activity in the surface modified electrode, a probable mechanistic pathway along with their electronic configurations has been proposed, as shown in **Scheme 5.2**. On application of a potential across the pristine h-MCO working electrode, the electrons and holes get generated, where the electrons move towards the FTO and h-MCO interface and the holes in the h-MCO move toward its surface, oxidising Co^{2+} to Co^{3+} and Mn^{3+} to Mn^{4+}. The Co^{3+} and Mn^{4+} ions at the active sites oxidises water to produce O_2 molecules at the h-MCO surface. The Co^{3+} and Mn^{4+} ions, by gaining electrons generated during the water oxidation process, reduce back to Co^{2+} and Mn^{3+} ions. In the h-MCO/NiPi electrode, where h-MCO coupled with NiPi, a material known for its faster surface kinetics for water oxidation helps in regenerating the original oxidation states of cobalt and manganese. Co^{3+} and Mn^{4+} ions generated in h-MCO transfer holes to Ni^{2+}, oxidising them to Ni^{3+}, thereby

reducing themself back to Co^{2+} and Mn^{3+} ions. In the composite, oxidation of water takes place at NiPi surface, reducing Ni^{3+} ions back to Ni^{2+}. The cyclic voltammetry in **Figure 5.10 (a)** and **Figure 5.10 (b)** supports the redox cycles taking place in the above-discussed mechanism. In **Figure 5.10 (a)**, on the application of potential, Co^{2+} is being oxidised to Co^{3+} and Mn^{3+} to Mn^{4+} and vice-versa. **Figure 5.10 (b)** shows the cyclic voltammetry of the h-MCO/NiPi electrode where the formation of the redox couple Ni^{2+} / Ni^{3+} is confirmed.

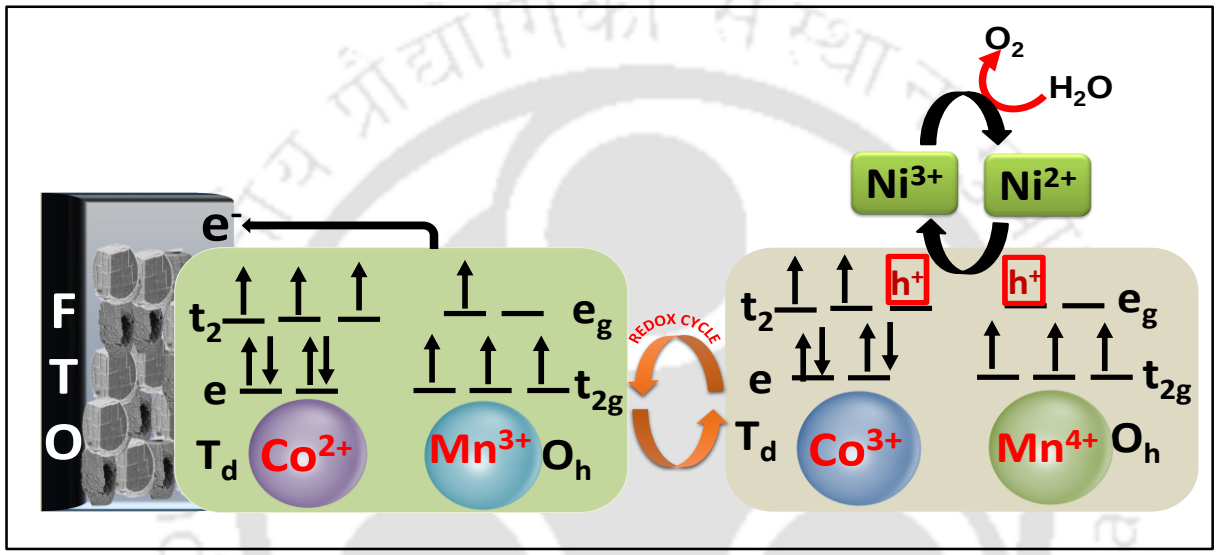

Scheme 5.2. Mechanistic pathway taking place in h-MCO/NiPi through different redox cycles for an efficient OER activity.

5.4 CONCLUSIONS

In summary, $MnCo_2O_4$ with hierarchical hollow cuboidal morphology was synthesised directly over the low-cost substrate by a green hydrothermal procedure. In-situ growth of hollow cuboidal $MnCo_2O_4$ over FTO provides good ohmic contact, which helps in faster charge transfer between hollow cuboidal $MnCo_2O_4$ and FTO. Deposition of NiPi over h-MCO through electrodeposition method enhances the OER activity of h-MCO/NiPi electrode to a lower overpotential of 230 mV and Tafel slope to 57 mV/dec. Surface modification using NiPi over h-MCO catalyst enhances the charge transfer kinetics of the modified electrode, which results in faster charge transfer at the interface of the working electrode and the electrolyte. A high C_{dl}

TH-2636_166122040

Part of this chapter has been published in **Chem. Commun.**, 2021,57, 8027

value of 31.9 mF/cm^2 signifies more available electrochemically surface active sites on the composite, with a TOF of 0.23 / sec which is ~ 3 fold higher than its bare counterpart. h-MCO/NiPi shows excellent long-term stability of 30 h without any significant decrease in current density, with a Faradic yield of 98 % confirming that the current generated is only due to the OER activity of the catalyst. High stability, low cost, and green synthesis procedure mark h-MCO/NiPi as one of the futuristic catalyst to be used in industrial applications.

5.5 REFERENCES

1. A.P. O'Mullane, M. Escudero-Escribano, I.E.L. Stephens, K. Krischer. *ChemPhysChem*, 2019, **20,** 2900.
2. G. Q. Li, S. T. Li, J. J. Ge, C. P. Liu and W. Xing. *J. Mater. Chem. A*, 2017, **5**, 17221.
3. X. Gao, J. Chen, X. Sun, B. Wu, B. Li, Z. Ning, J. Li, and N. Wang. *ACS Appl. Nano Mater*. 2020, **3**, 12269.
4. Y. Yan, B. Y. Xia, B. Zhao and X. Wang. *J. Mater. Chem. A*, 2016, **4**, 17587.
5. I. Concina, Z. H. Ibupoto and A. Vomiero. *Adv. Energy Mater.*, 2017, **7**, 1700684.
6. N.-T. Suen, S.-F. Hung, Q. Quan, N. Zhang, Y.-J. Xu and H. M. Chen. *Chem. Soc. Rev.*, 2017, **46**, 337.
7. B. You and Y. Sun. *Acc. Chem. Res.*, 2018, **51**, 1571.
8. Y. Zhu, Q. Lin, Y. Zhong, H. A. Tahini, Z. Shao and H. Wang. *Energy Environ. Sci.*, 2020, **13**, 3361.
9. X. Huang, H. Zheng, G. Lu, P. Wang, L. Xing, J. Wang and G. Wang. *ACS Sustainable Chem. Eng.*, 2019, **7**, 1169.
10. X. Du, H. Su and X. Zhang. *Int. J. Hydrogen Energy*, 2019, **44**, 21637.
11. A. Rebekah, E. Ashok Kumar, C. Viswanathan and N. Ponpandian. *Int. J. Hydrogen Energy*, 2020, **45**, 6391.

12. Y. Zhan, M. Lu, S. Yang, Z. Liu, and J. Y. Lee. *ChemElectroChem* , 2016, **3**, 615.
13. Y. Surendranath, M. W. Kanan and D. G. Nocera. *J. Am.Chem. Soc.*, 2010, **132**, 16501.
14. C. Yang, C. Laberty-Robert, D. Batuk, G. Cibin, A. V. Chadwick, V. Pimenta, W. Yin , L. Zhang , J.-M. Tarascon and A. Grimaud. *J. Phys. Chem. Lett.*, 2017, **8**, 3466.
15. P. W. Menezes, A. Indra, N. R. Sahraie, A. Bergmann, P. Strasser and M. Driess. *ChemSusChem*, 2015, **8**, 164.
16. W. Wang, L. Kuai, W. Cao, M. Huttula, S. Ollikkala, T. Ahopelto, A. P. Honkanen, S. Huotari, M. Yu and B. Geng. Angew. *Chem., Int. Ed.*, 2017, **56**, 14977.
17. I. Abidat, N. Bouchenafa-Saib, A. Habrioux, C. Comminges, C. Canaff, J. Rousseau, T. W. Napporn, D. Dambournet, O. Borkiewicz and K. B. Kokoh. *J. Mater. Chem. A*, 2015, **3**, 17433.
18. J. R. Han, S. Hao, Z. A. Liu, A. M. Asiri, X. P. Sun and Y. H. Xu, *Chem. Commun.*, 2018, **54**, 1077.
19. J. Huang, Y. Xiong, Z. Peng, L. Chen, L. Wang, Y. Xu, L. Tan, K. Yuan, Y. Chen. *ACS Nano*, 2020, **14**, 14201.
20. P. Sukha, P. Sirisinudomkit, A. Seubsai, M. Chareonpanich, P. Kongkachuichay, J. Limtrakul and M. Sawangphruk. *ACS Appl. Mater. Interfaces*, 2016, **8**, 34045.
21. F. S. Omar, A. Numan, S. Bashir, N. Duraisamy, R. Vikneswaran, Y.-L. Loo, K. Ramesh and S. Ramesh. *Electrochim. Acta*, 2018, **273**, 216.
22. V. Venkatachalam, A. Alsalme, A. Alghamdi and R. Jayavel. *J. Electroanal. Chem.*, 2015, **756**, 94.
23. H. Shao, N. Padmanathan, D. McNulty, C. O'Dwyer and K. M. Razeeb. *ACS Appl. Mater. Interfaces*, 2016, **8**, 28592.
24. Y. Zhang, L. Q. Luo, Z. Zhang, Y. P. Ding, S. Liu, D. M. Deng, H. B. Zhao and Y. Chen, *J. Mater. Chem. B*, 2014, **2**, 529.

TH-2636_166122040

Part of this chapter has been published in **Chem. Commun.,** 2021,57, 8027

25. M.A. Al-Omair, A.H. Touny and M.M. Saleh, *J. Power Sources*, 2017, **342**, 1032.

26. D. Guo, Z. Wu, Y. An, X. Li, X. Guo, X. Chu, C. Sun, M. Lei, L. Li, L. Cao, P. Li and W. Tang. *J. Mater. Chem. C*, 2015, **3**, 1830.

27. J. Chen, X. F. Wu and A. Selloni. Phys. Rev. B: Condens. *Matter Mater. Phys.*, 2011, **83**, 245204.

28. Y. Zhai, H. Mao, P. Liu, X. Ren, L. Xu and Y. Qian. *J. Mater. Chem. A*, 2015, **3**, 16142.

29. D. Fa, B. Yu and Y. Miao. *Colloids Surf., A*, 2019, **564**, 31.

30. J. Bao, X. Zhang, B. Fan, J. Zhang, M. Zhou, W. Yang, X. Hu, H. Wang, B. Pan and Y. Xie. *Angew. Chem., Int. Ed.*, 2015, **54**, 7399.

31. Y. Li, L. Zhang, X. Xiang, D. Yan and F. Li. *J. Mater. Chem. A*, 2014, **2**, 13250.

32. L. Kumar, M. Chauhan, P. K. Boruah, M. R. Das, S. A. Hashmi and S. Deka. *ACS Appl. Energy Mater.* 2020, **3**, 6793.

33. X. Zhang, C. Si, X. Guo, R. M. Kong and F. Qu. *J. Mater. Chem. A*, 2017, **5**, 17211.

34. C. Jiang, S. J. Moniz, A. Wang, T. Zhang and J. Tang. *Chem. Soc. Rev.*, 2017, **46**, 4645.

TH-2636_166122040

Part of this chapter has been published in **Chem. Commun.,** 2021,57, 8027

CHAPTER 6

Cuboidal $MnCo_2O_4$/h-boron nitride heterojunction: Enhanced oxygen evolution reaction via efficient hole extraction approach

In this chapter, complex spinel oxide is fabricated directly onto the substrate as a highly stable electrocatalytic anode material for oxygen evolution reaction (OER). Herein, efforts are done to replace noble-metal-based electrocatalyst, in OER activity. In the present chapter, surfactant-free cuboidal $MnCo_2O_4$ (C-MCO) was synthesized in-situ over by green and simple synthetic protocol. Stable and good ohmic contact between C-MCO and the substrate ensures efficient charge transfer at their interface. Hexagonal boron nitride (h-BN) nanosheets coupled with C-MCO, provides more electrochemically active surface sites for enhanced OER activity. The study in the present chapter can be used for large-scale clean energy production owing to its low-cost, efficient, eco-friendly, and long-term stability of C-MCO/h-BN electrocatalyst.

A. K. Shah, et al., **ACS Appl. Energy Mater,** 2022, 5, 1551

6.1 INTRODUCTION

The worldwide energy economy still largely based on hydrocarbon consumption, has hostile consequences on the climate, earth ecosystem, and human health.[1] It is essential for us to find green energy technologies for moving towards the net-zero carbon approach in the future. The technologies such as electrochemical and solar-driven photoelectrochemical water splitting for hydrogen and oxygen production are promising approaches to deliver affordable clean energy and mitigate the effect of climate change.[2] Electrochemical approach of water splitting for energy production is cost-effective, easy to operate, and can function in harsh environmental and climatic conditions. Electrochemical water splitting consists of two half-reactions: oxygen evolution reaction (OER) which takes place at the anode and hydrogen evolution reaction (HER) occurs at the surface of the cathode. OER is thermodynamically an uphill process and required more overpotential than the HER, therefore considered to be the rate-determining step for water splitting.[3,4] To overcome the large overpotential for the OER process, electrocatalysts are used to make the process less energy-intensive. In spite of substantial advancements in OER, it is essential to replace noble metal oxides like RuO_2 and IrO_2, and find alternative earth-abundant materials.[5] Traditional metal oxides are high in price, and their poor electrochemical stability hinders them to be used in the large-scale application.[6,7]

Various transition metal oxides (CoO_x, $ZnCo_2O_4$, and $MnCo_2O_4$), phosphides (CoP, $NiFeP_x$), and sulfides (Ni_3S_2, $FeNiS_2$) are explored for their OER applications.[3,7] Metal oxides owing to their wide electrochemical potential and their excellent stability in alkaline media are one of the preferred catalysts for OER activity. Spinel bimetallic oxide such as $MnCo_2O_4$, due to its low cost, high stability, easy fabrication technique, non-toxicity, and high intrinsic electrical conductivity, gaining popularity in OER studies.[8] OER activity of pristine $MnCo_2O_4$ is limited due to its high charge transfer resistance at electrode-electrolyte interface and sluggish OER kinetics.[9] The strategies such as, morphological tuning using various structure-

TH-2636_166122040

Part of this chapter has been published in **ACS Appl. Energy Mater:** 2022, 5, 1551

directing agents, surface engineering, and elemental doping were adopted to improve the OER activity of $MnCo_2O_4$.[9,10] Reports on $MnCo_2O_4$ for OER activity involved synthesis in the powder form and then drop-casting over the substrate giving a substantially reduced OER efficiency due to poor ohmic contact between the catalyst and the substrate.[11,12]

Recent research on OER emphasizes using materials such as carbon nanosheets, graphene, and hexagonal boron nitride (h-BN) nanosheets for their ease of fabrication, cost-effectiveness, and eco-friendly nature.[13-15] In particular, h-BN, a structural analog of graphene, also known as white graphene has shown great potential for OER due to its high chemical and thermal stability under harsh environmental conditions along with the efficient charge transfer kinetics.[16,17] h-BN nanosheets having an intrinsic negative charge, provides an excellent electronic interaction at the interfaces of the catalysts in a heterostructure, which also makes it a prominent hole acceptor agent for the OER process.[18]

In the present work, we have grown cuboidal structured $MnCo_2O_4$ directly over FTO substrate via a green synthetic protocol, which established good ohmic contact between the substrate and the catalyst, allowing easy flow of charge carriers at their interface. Cuboidal structure $MnCo_2O_4$ was synthesized without using any surfactant, facets in it provide a surface for easy deposition of co-catalyst, making active sites easily available and accessible for OER activity. Herein, we have incorporated noble metal-free h-BN nanosheets over $MnCo_2O_4$, to overcome its poor charge transfer kinetics. The surface modified $MnCo_2O_4$/h-BN displays, a lower overpotential for OER activity, apart from its enhanced OER kinetics and improved turnover frequency than its pristine counterpart. As, green and sustainable $MnCo_2O_4$/h-BN electrode shows good OER activity, along with long term stability in harsh alkaline conditions, it has the potential to be used in large-scale energy production application and can be used as a model system for understanding physical chemistry aspects of the OER process having a hole extractor at its disposal.

TH-2636_166122040

Part of this chapter has been published in **ACS Appl. Energy Mater:** 2022, 5, 1551

6.2 EXPERIMENTAL SECTION

6.2.1 Synthesis and Fabrication Protocol of C-MCO

Step-by-step fabrication for the C-MCO/h-BN electrode was shown in **Scheme 6.1**. The C-MCO was synthesized over FTO through a hydrothermal route.[8] $Mn(NO_3)_2.4H_2O$ (2 mmol), $Co(NO_3)_2.6H_2O$ (4 mmol), and urea (24 mmol) were dissolved in 70 ml deionized water, and the solution was kept under stirring for 2 h. In a 100 ml teflon-lined autoclave, FTO were kept facing up, and only 1 x 1 cm^2 of FTO was kept exposed to the solution. Polyimide tape which can sustain high temperature and pH was put over the FTO to control the area of FTO exposed to the solution. The above solution mixture was then transferred into the autoclave and was kept in an oven at 150 °C for 24 h. Pink-colored $MnCo(OH)_x$ was formed over FTO, which was later washed by deionized water and ethanol. After drying at 100 °C, it was transferred to a muffle furnace and was calcined at 450 °C for 3 h to form black coloured C-MCO electrode.

6.2.2 Synthesis of C-MCO/h-BN

Commercially procured bulk h-BN was exfoliated to get h-BN nanosheets, which were later drop-casted over C-MCO to form C-MCO/h-BN.[19] In a typical synthetic procedure, 600 mg bulk h-BN was put in 45 ml of water, 3 ml of ethanol, and 2 ml acetone. It was then sonicated for 12 h, later it was centrifuged at 2000 rpm for 1 h. The supernatant part was slowly poured into a beaker and precipitate was discarded. The above process was repeated twice to get highly dispersed h-BN nanosheets.100 µl cm^{-2} of exfoliated h-BN nanosheets was drop-casted over C-MCO, which was then heated at 120 $^{\circ}C$ for 1.5 h to form C-MCO/h-BN electrode, to complete one cycle of h-BN nanosheets deposition over C-MCO.

TH-2636_166122040

Part of this chapter has been published in **ACS Appl. Energy Mater:** 2022, 5, 1551

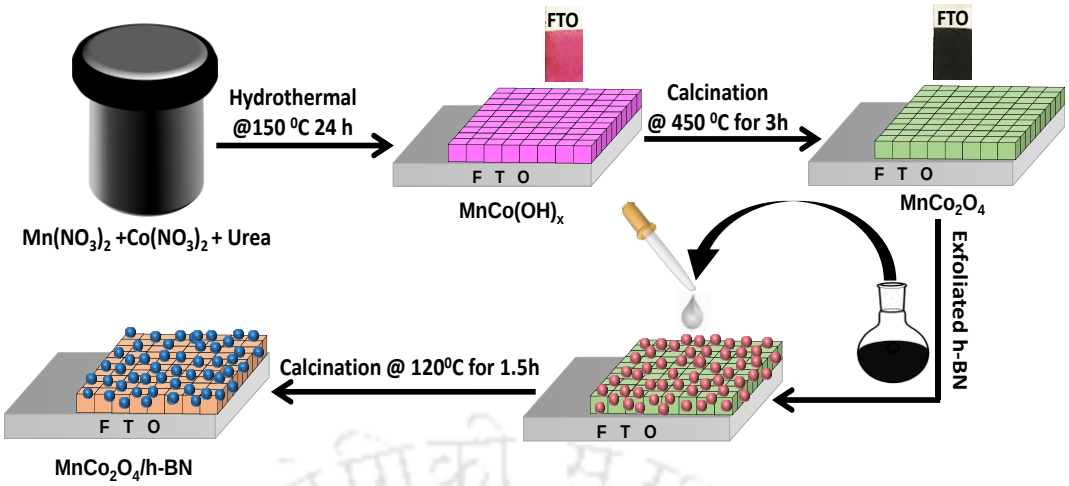

Scheme 6.1. Step-by-step synthetic protocol for green and cost-effective fabrication of C-MCO/h-BN electrode. Step 1 involves the hydrothermal aided formation of $MnCo(OH)_x$ as a pink-colored compound (photograph shown) followed by calcination to yield black $MnCo_2O_4$ formation (photograph shown). Step 2 involves deposition of h-BN through drop-casting, to form the heterojunction.

6.2.3 Mechanism for the Formation of Cuboidal $MnCo_2O_4$

Scheme 6.2 shows a plausible mechanism for the formation of cuboidal $MnCo_2O_4$ onto the FTO substrate. The crystal lattice of the $MnCo_2O_4$ is cubic, thereby under no additional influence/ reagents, it prefers to form the thermodynamically stable cuboidal shape. Initially, urea in the precursor solution reacts with water during the hydrothermal reaction to form the hydroxide, and then Co^{2+}, $Mn^{2+,}$ and OH^- reacts to form $MnCo(OH)_X$, which later undergoes nucleation to form nanoparticles.

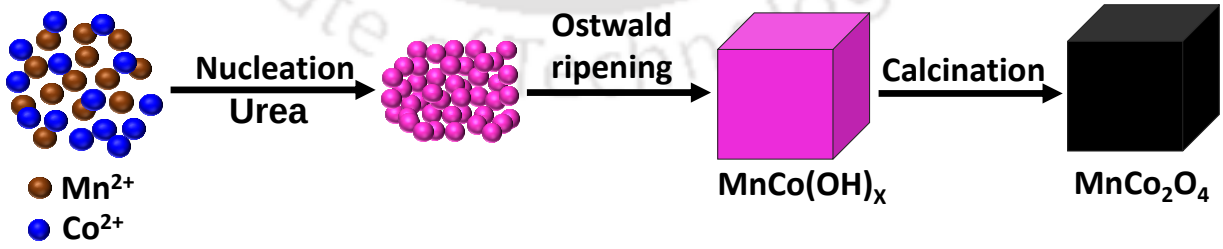

Scheme 6.2. Mechanistic steps involved in the formation of cuboidal $MnCo_2O_4$ directly over the conducting substrate under hydrothermal conditions.

Part of this chapter has been published in **ACS Appl. Energy Mater:** 2022, 5, 1551

The nucleated $MnCo(OH)_X$ nanoparticles, went through Ostwald ripening to form a thermodynamically stable cuboidal structure. The $MnCo(OH)_X$ due to Van der Waals or electrostatic force, gets adsorbed at FTO substrate, to form $MnCo(OH)_X$ thin film. The hydroxides in $MnCo(OH)_X$ decomposed upon calcination to form cuboidal $MnCo_2O_4$.[20,21]

6.2.4 Purification of Electrolyte (KOH)

The electrolyte, 1 M KOH was made iron-free for electrochemical measurements by using the following purification procedure.[22] 2g of 99.99 % $Ni(NO_3)_2 \cdot 6H2O$ was taken in a cleaned polypropylene centrifuging tube and were dissolved in 4 ml of Milli Q water. Then, 20 ml of 1 M KOH was added to form $Ni(OH)_2$ precipitate. The mixture was shaken well and then centrifuged, later decanting the supernatant part. Finally, 50 ml of 1 M KOH was put into the tube for purification. Then it was shaken for 10 min and was then kept undisturbed for 3 h. Later the mixture was centrifuged and the supernatant part was kept in a cleaned polypropylene bottle.

6.3 RESULTS AND DISCUSSION

6.3.1 Powder X-Ray Diffraction (PXRD) Analysis

Powder X-ray diffraction (PXRD) analysis was done to determine the formation of the electrocatalysts. **Figure 6.1 (a, b and c)** shows the PXRD pattern of C-MCO, h-BN nanosheets, and C-MCO/h-BN respectively. Corresponding (hkl) planes of all the catalysts were indexed, confirming the purity of C-MCO (JCPDS Card No - 00-023-1237) and h-BN (JCPDS Card No - 00-009-0012.[9, 23] **Figure 6.1 (c)** shows the PXRD pattern of the composite C-MCO/h-BN, where all the peaks corresponding to C-MCO were indexed, while due to very less amount of h-BN nanosheets loading over C-MCO, the diffraction peak of h-BN nanosheets was not detectable in the composite.

TH-2636_166122040

Part of this chapter has been published in **ACS Appl. Energy Mater:** 2022, 5, 1551

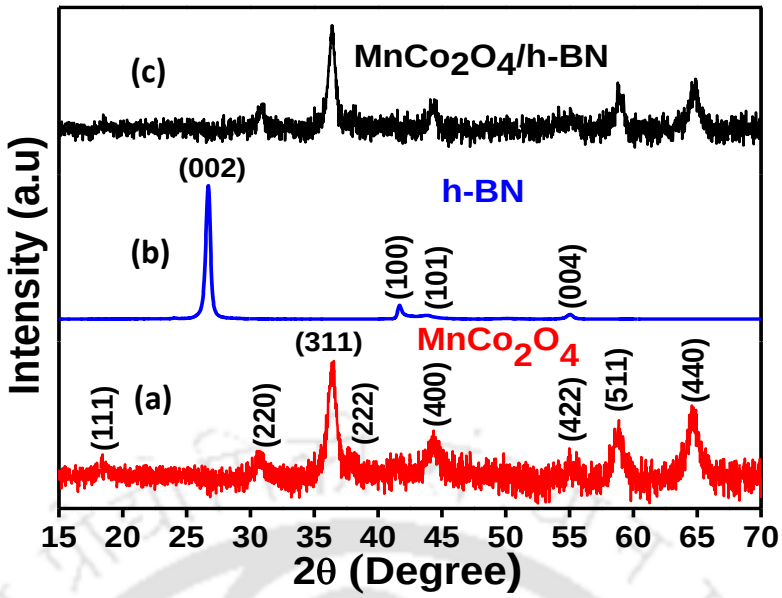

Figure 6.1. Powder X-ray diffraction (PXRD) patterns of spinel, (a) C-MCO (JCPDS Card No - 00-023-1237, Crystal System: cubic), (b) h-BN nanosheets (JCPDS Card No - 00-009-0012, Crystal System: Hexagonal), (c) C-MCO/h-BN.

6.3.2 Raman Spectroscopy Analysis

To further confirm the formation of composite C-MCO/h-BN, Raman spectra of C-MCO, h-BN nanosheets, and C-MCO/h-BN were recorded, as shown in **Figure 6.2**.

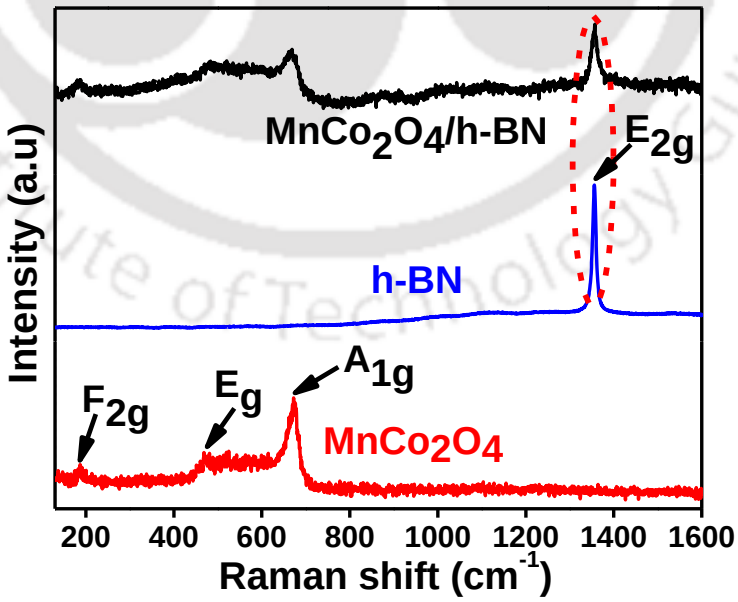

Figure 6.2. Laser Raman spectra of C-MCO, h-BN nanosheets, and C-MCO/h-BN. The presence of Raman bands parallel to C-MCO and h-BN nanosheets in C-MCO/h-BN indicates the formation of the composite.

TH-2636_166122040

Part of this chapter has been published in **ACS Appl. Energy Mater:** 2022, 5, 1551

Raman bands at 187 cm^{-1}, 473 $cm^{-1,}$ and 673 cm^{-1} corresponds to F_{2g}, E_g, and A_{1g} modes of spinel C-MCO respectively, while the band at 1356 cm^{-1} corresponds to E_{2g} mode of h-BN nanosheets.[24-26] Together presence of Raman bands, parallel to C-MCO and h-BN nanosheets in the C-MCO/h-BN confirms the formation of the composite. Moreover, broadening of the characteristics E_{2g} Raman band of h-BN in the composite when compared to pristine h-BN was observed, supporting the formation of the composite.

6.3.3 Morphological and Structural Analysis

To study the morphology of the electrocatalysts, field emission scanning electron microscopy (FESEM) analysis was done. **Figure 6.3 (a)** shows the FESEM image of closely packed and uniformly distributed, in-situ grown pristine C-MCO. **Figure 6.3 (b)** shows FESEM images of exfoliated h-BN nanosheets. **Figure 6.3 (c)** shows the FESEM image of the composite C-MCO/h-BN, displaying the deposition of h-BN nanosheets over C-MCO. The C-MCO, having different facets, makes active sites easily accessible to the electrolyte for OER activity and also offers surface for easy deposition of h-BN nanosheets.

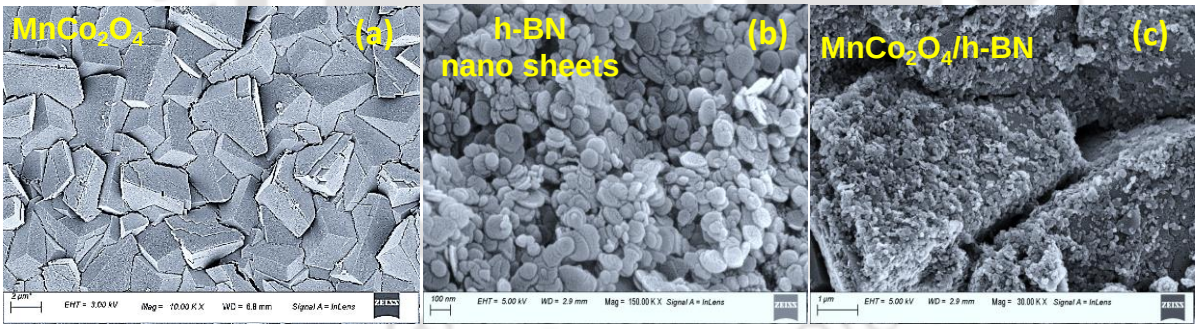

Figure 6.3. (a) FESEM image of in-situ grown C-MCO which are closely packed and uniformly distributed with an average size of ~ 4 µm. (b) FESEM image of h-BN nanosheets. (d) FESEM image of C-MCO-h/BN showing loading of h-BN over C-MCO.

Figure 6.4 (a) shows the FETEM image of bare C-MCO, which shows that the cuboidal structure of bare $MnCo_2O_4$ is formed by the combination of nanoparticles. **Figure 6.4 (b)** shows FETEM images of exfoliated h-BN nanosheets. Further to show, deposition of h-BN nanosheets over C-MCO, FETEM analysis of C-MCO/h-BN heterostructure was performed.

TH-2636_166122040
Part of this chapter has been published in **ACS Appl. Energy Mater:** 2022, 5, 1551

Figure 6.4 (c) shows the deposition of h-BN nanosheets over C-MCO. To confirm the formation of composite, a high-resolution transmission electron microscope (HRTEM) analysis of C-MCO/h-BN was done. HRTEM image of the composite C-MCO/h-BN in **Figure 6.4 (d)** with Inverse fast Fourier transformed (IFFT) image displays different lattice spacing of 0.30 nm and 0.21 nm, which corresponds to (220) and (101) crystal plane of C-MCO and h-BN nanosheets respectively, confirming the formation of composite.[27]

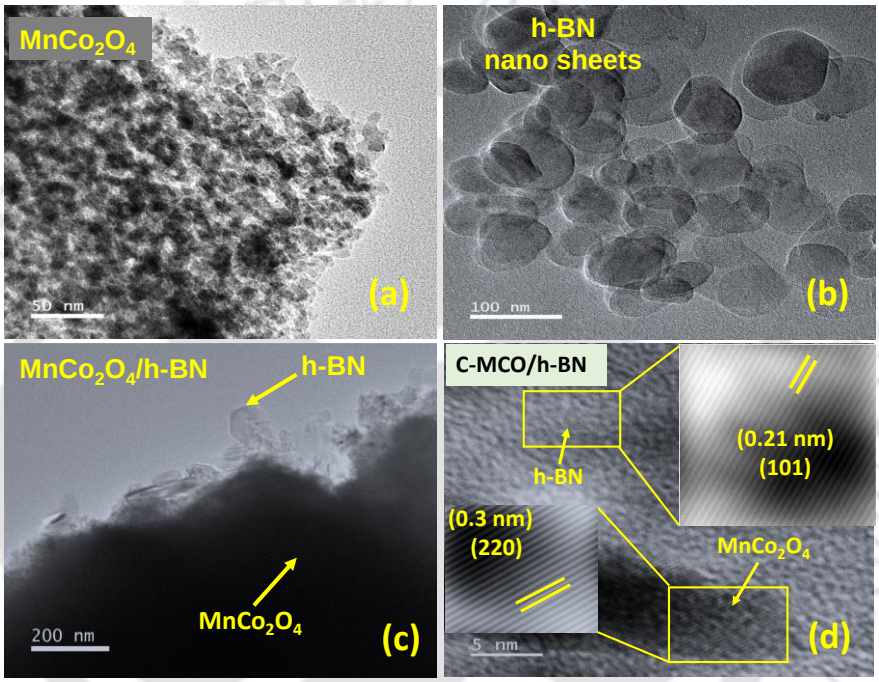

Figure 6.4. (a) FETEM image of pristine C-MCO. (b) FETEM image of h-BN nanosheets, showing well-exfoliated h-BN. (c) FETEM image of C-MCO/h-BN, showing deposition of h-BN nanosheets over C-MCO, indicating the formation of heterojunction between C-MCO and h-BN nanosheets. (d) HRTEM image of C-MCO/h-BN with d-spacing values of 0.3 nm and 0.21 nm corresponds to (220) and (101) plane of C-MCO and h-BN nanosheets respectively. The presence of both planes together in the composite confirms the formation of the composite.

Figure 6.5 (a-f) shows FESEM energy-dispersive X-ray spectroscopic (EDX) elemental mapping image of C-MCO-h/BN, confirming the presence and uniform distribution of all the elements available in the composite.

TH-2636_166122040

Part of this chapter has been published in **ACS Appl. Energy Mater:** 2022, 5, 1551

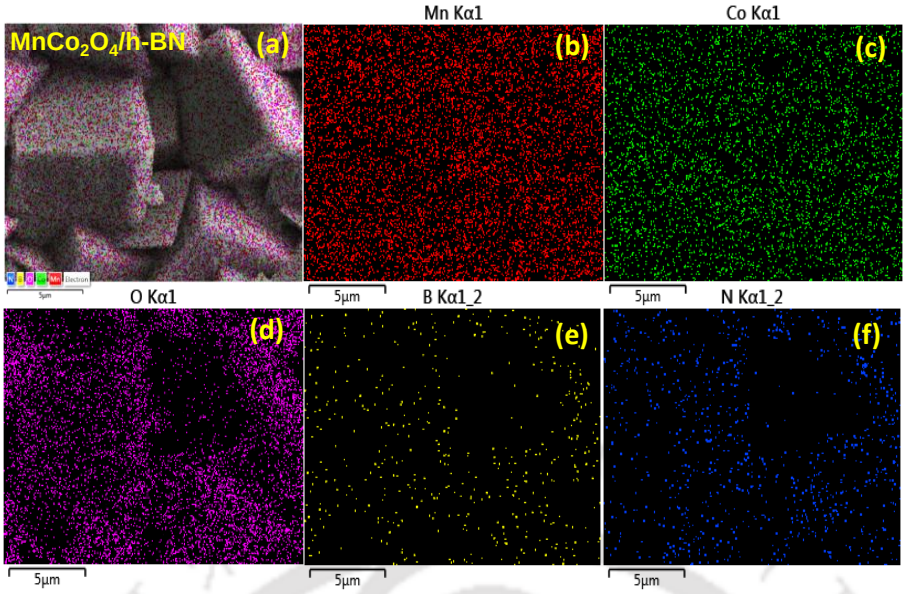

Figure 6.5. (a-f) FESEM energy-dispersive X-ray spectroscopic (EDX) elemental mapping image of C-MCO-h/BN. Elemental mapping shows the uniform distribution of each element present in C-MCO-h/BN throughout the composite.

6.3.4 FTIR Spectra Analysis

Further to determine the interaction between C-MCO and h-BN nanosheets in C-MCO/h-BN heterostructure, Fourier-transform infrared (FTIR) spectroscopy measurement was performed, as shown in **Figure 6.6 (a)** The presence of two strong peaks at 551 cm^{-1} and 657 cm^{-1} was attributed to the vibrational bending modes of Mn-O and Co-O respectively in C-MCO.

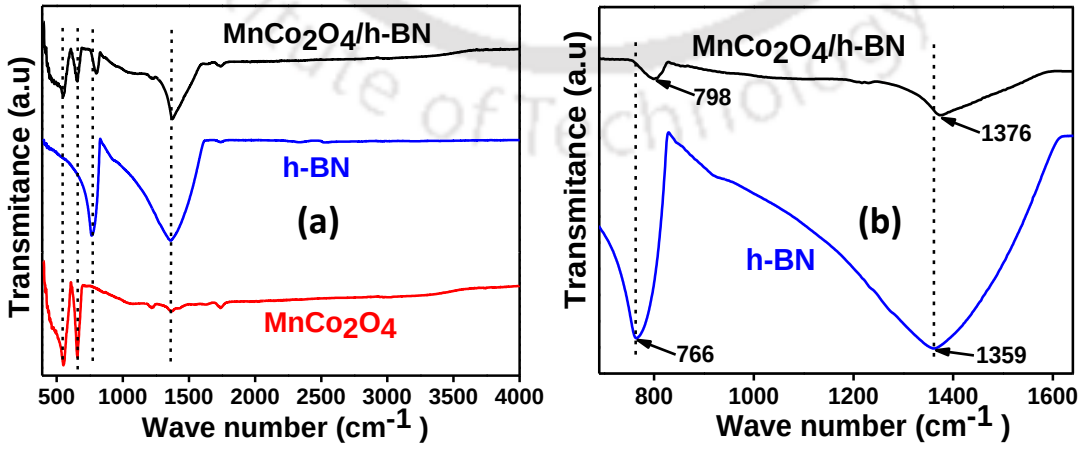

Figure 6.6. (a) Fourier-transform infrared (FTIR) spectra C-MCO, h-BN nanosheets, and C-MCO/h-BN. (b) Shift in the FTIR peaks of h-BN nanosheets in C-MCO/h-BN towards higher binding energy.

TH-2636_166122040

Peaks at 766 cm^{-1} and 1359 cm^{-1} in h-BN nanosheets correspond to B-N bending and B-N stretching modes of vibrations respectively.[25,28] A shift in the B-N peaks shown in **Figure 6.6 (b)** towards higher frequency in C-MCO/h-BN, indicates good interaction between C-MCO and h-BN nanosheets in the heterostructure.

6.3.5 X-Ray Photoelectron Spectroscopy (XPS) Analysis

To identify the valence state and change in the electronic environment around the elements, an X-ray photoelectron spectroscopy (XPS) analysis was carried out. The presence of corresponding elements present in C-MCO/h-BN, C-MCO, and h-BN was confirmed by the XPS survey spectra, as shown in **Figure 6.7 (a)**. **Figure 6.7 (b)** shows the core level Mn 2p XPS spectra of C-MCO/h-BN and C-MCO. Peaks at binding energy (BE), 641.93 eV, 641.51 eV corresponds to $2p_{3/2,}$ and peaks at BE, 653.36 eV, 652.80 eV corresponds to $2p_{1/2}$ for Mn^{2+} in C-MCO/h-BN and C-MCO respectively. Whereas peaks at BE, 643.55 eV, 643.31 eV corresponds to $2p_{3/2}$ and peaks at BE, 655.13 eV, 654.60 eV corresponds to $2p_{1/2}$ for Mn^{3+} in C-MCO/h-BN and C-MCO respectively. Peaks at BE, 647.97 eV, and 647.92 eV were assigned to the satellite peaks of C-MCO/h-BN and C-MCO respectively.[9,29] **Figure 6.7 (c)** shows the core level Co 2p XPS spectra of C-MCO/h-BN and C-MCO. Peaks at binding energy (BE), 780.63 eV, 780.27 eV corresponds to $2p_{3/2,}$ and peaks at BE, 795.72 eV, 795.46 eV corresponds to $2p_{1/2}$ for Co^{2+} in C-MCO/h-BN and C-MCO respectively. While peaks at BE, 782.24 eV, 781.79 eV corresponds to and $2p_{3/2}$ and peaks at BE, 797.29 eV, 797.20 eV corresponds to $2p_{1/2}$ for Co^{3+} in C-MCO/h-BN and C-MCO respectively. Peaks at BE, 787.42 eV, and 803.75 eV corresponds to satellite peaks of C-MCO/h-BN, whereas peaks at BE 787.32 eV and 803.70 eV were assigned to the satellite peaks of C-MCO.[9,30] **Figure 6.7 (d)** displays core level XPS spectra of B 1s of C-MCO/h-BN and h-BN nanosheets, peaks at BE, 190.22 eV and 190.32 eV corresponds to C-MCO/h-BN and h-BN respectively.[29,30] **Figure 6.7 (e)** shows N 1s core level spectra of C-MCO/h-BN and h-BN nanosheets, peaks at BE, 397.45 eV and 397.75 eV

TH-2636_166122040

Part of this chapter has been published in **ACS Appl. Energy Mater:** 2022, 5, 1551

corresponds C-MCO/h-BN and h-BN respectively. The shift in the peak position of N 1s and B 1s core level spectra towards lower binding energy in the composite was due to the formation of N-O bond between h-BN and C-MCO, which indicates good electronic interaction between C-MCO and h-BN nanosheets in the heterostructure.[31,32] **Figure 6.7 (f)** shows O 1s core level spectra of C-MCO/h-BN and pristine C-MCO. Peaks at BE, 529.80 eV, 530.41 eV, and 531.89 eV correspond to lattice oxygen (O_L) (metal-oxygen), oxygen vacancy (O_V), and adsorbed oxygen ($O_{ads.}$) respectively of pristine C-MCO. Peaks at BE, 529.90 eV, 530.56 eV, 531.42 eV, and 531.90 eV corresponds to O_L, O_V, N-O bond, and $O_{ads.}$, respectively in C-MCO/h-BN.[9,32] Appearance of N-O peak in the composite confirms bonding between nitrogen and oxygen of h-BN nanosheets and C-MCO respectively.

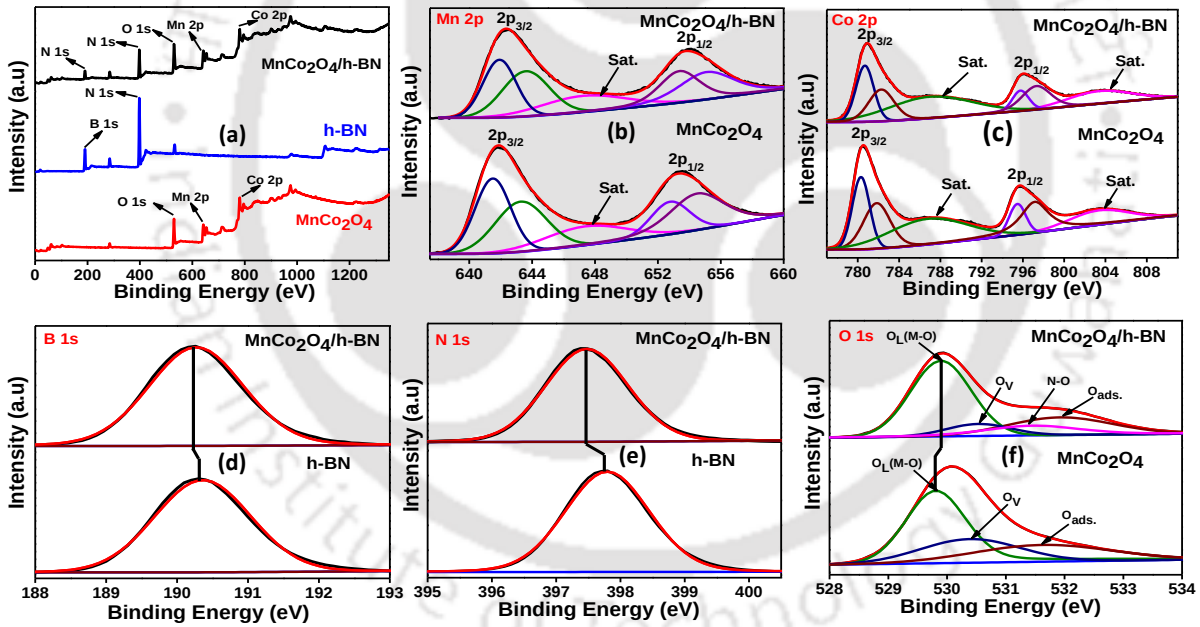

Figure 6.7. (a) Survey spectra of C-MCO/h-BN, C-MCO, and h-BN. (b) Core level XPS spectra of Mn 2p in C-MCO/h-BN and C-MCO were deconvoluted to show the presence of Mn in a mixed oxidation state (Mn^{2+} and Mn^{3+}). (c) Core level XPS spectra of Co 2p in C-MCO/h-BN and C-MCO were deconvoluted to show that Co is present in a mixed oxidation state (Co^{2+} and Co^{3+}). (d) Core level XPS spectra of B 1s in C-MCO/h-BN and h-BN nanosheets. (e) Core level XPS spectra of N 1s in C-MCO/h-BN and h-BN nanosheets. (f) O 1s core level spectra of C-MCO/h-BN and C-MCO.

TH-2636_166122040
Part of this chapter has been published in **ACS Appl. Energy Mater:** 2022, 5, 1551

6.3.6 Zeta Potential

To know the nature of surface charge in h-BN nanosheets, zeta potential measurements was carried out, as shown in **Figure 6.8**. Zeta potential value for h-BN nanosheets was found to be -33.1, which is highly negative in value, confirming hole extracting ability of h-BN nanosheet.[27]

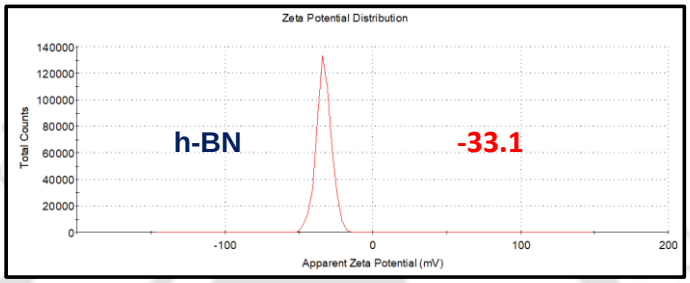

Figure 6.8. Zeta Potential value of h-BN nanosheets displaying highly negative Zeta potential value (-33.1).

6.3.7 Electrochemical Measurements

To determine the OER performance of electrocatalysts, linear-sweep voltammetry measurements (LSV) were performed. **Figure 6.9 (a)** shows the LSV curves of respective electrocatalysts, measured at the scan rate of 1 mV/sec, and the overpotential of each electrode was determined at the current density of 10 mA/cm^2 (η_{10}). The η_{10} value of pristine C-MCO was found to be 390 mV/cm^2, while for h-BN nanosheets η_{10} was calculated to be 425 mV/cm^2, and h-BN nanosheets modified C-MCO/h-BN electrode shows lower η_{10} value of 240 mV/cm^2. The OER performance of the C-MCO/h-BN electrode was determined with 1.20 mg/cm^2 and 0.11 mg/cm^2 loading of C-MCO and h-BN respectively to understand the mass activity. The OER performance of C-MCO/h-BN was compared with the benchmark catalyst (RuO_2), with the same loading amount of catalyst and under similar experimental conditions. RuO_2 displays η_{10} = 290 mV, indicating modified electrode displays better OER performance than the traditional metal oxide. **Figure 6.9 (b)** shows the optimised OER activity of C-MCO/h-BN with different loading amounts of h-BN nanosheets over C-MCO. The third cycle of h-BN nanosheets loading over C-MCO shows maximum OER activity. To examine the

TH-2636_166122040

Part of this chapter has been published in **ACS Appl. Energy Mater:** 2022, 5, 1551

reproducibility of the modified electrode, three consecutive linear sweep voltammetry measurement of the same $MnCo_2O_4$/h-BN electrode was carried out. The three consecutive measurements of $MnCo_2O_4$/h-BN, shown in **Figure 6.9 (c)** confirm the reproducibility of OER activity by the modified electrode.

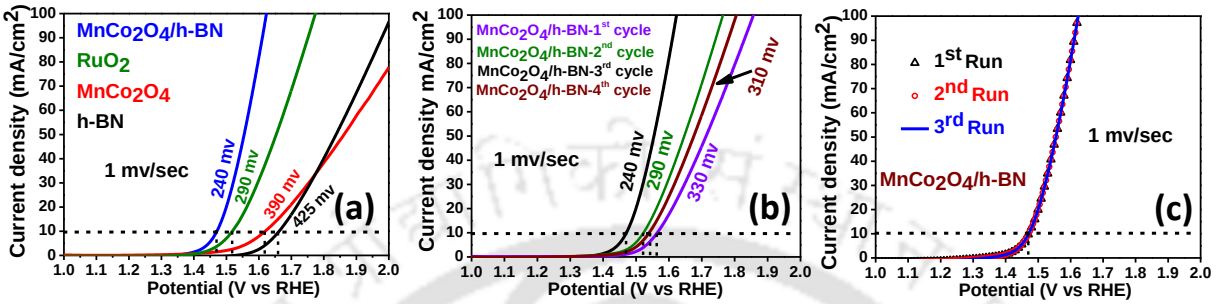

Figure 6.9. (a) Linear sweep voltammetry (LSV) curves of C-MCO/h-BN, RuO_2, C-MCO and h-BN nanosheets at the scan rate of 1 mV/sec in purified 1 M KOH. (b) Optimised LSV curves of C-MCO/h-BN electrode with different loading amount of h-BN nanosheets over C-MCO. (c) Reproducibility test of C-MCO/h-BN.

Further to determine the OER kinetics of the electrocatalysts, Tafel slope values were calculated. The Tafel slope is shown in **Figure 6.10 (a)** of each catalyst was calculated from their respective LSV curves. The metal-free surface-modified C-MCO/h-BN shows a lower Tafel slope value of 66 mV/dec, while pristine C-MCO displays a Tafel slope value of 207 mV/dec. Tafel slope values for h-BN nanosheets and RuO_2 were calculated to be 106 mV/dec and 78 mV/dec respectively. The Lower Tafel slope value of the composite indicates, C-MCO/h-BN displays faster OER kinetics than the precious metal oxide (RuO_2) and pristine C-MCO under harsh alkaline conditions.[13] To get insight into enhanced OER performance of the modified electrocatalyst, electrochemical impedance spectroscopy (EIS) measurement was done at 1.6 V vs RHE. Charge transfer resistance (R_{ct}) of the electrocatalysts was determined from the Nyquist plot, as shown in **Figure 6.10 (b)**. R_{ct} value of the composite C-MCO/h-BN was calculated to be 3.9 Ω, while for pristine C-MCO and h-BN, R_{ct} was found to be 23.9 Ω and 5.7 Ω respectively. The lower R_{ct} value of the modified electrode indicates the smooth transfer of charge carriers at the interface of composite (C-MCO/ h-BN) and the electrolyte.[33]

TH-2636_166122040

Part of this chapter has been published in **ACS Appl. Energy Mater:** 2022, 5, 1551

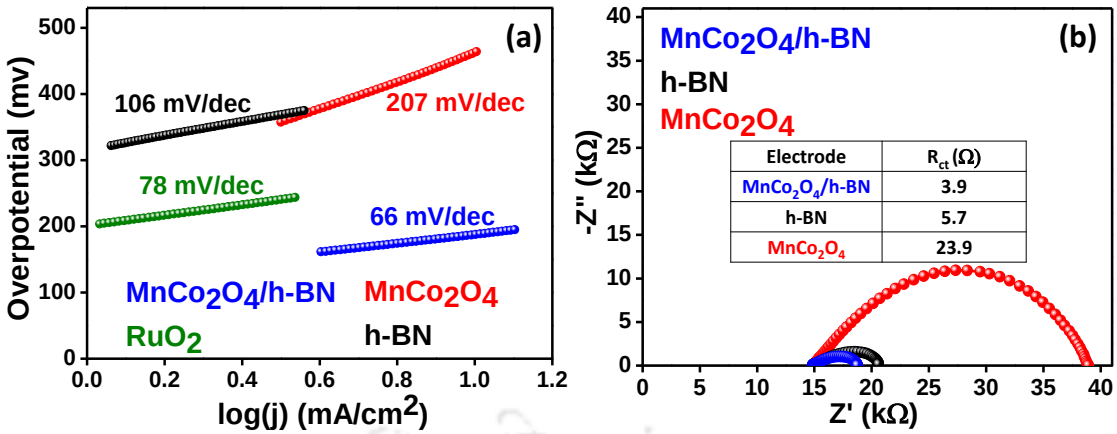

Figure 6.10. (a) Tafel plots of C-MCO/h-BN, RuO_2, C-MCO, and h-BN nanosheets. (b) Nyquist plot of C-MCO/h-BN, C-MCO, and h-BN at 1.6 V vs RHE.

Figure 6.11 shows cyclic voltammetry of pristine C-MCO electrode, displaying redox process taking place in it on the application of potential. In the voltammogram of C-MCO, on the applying potential across the electrode, Mn^{3+} get oxidised to Mn^{4+}, and Co^{2+} is oxidised to Co^{3+} and vice-versa.

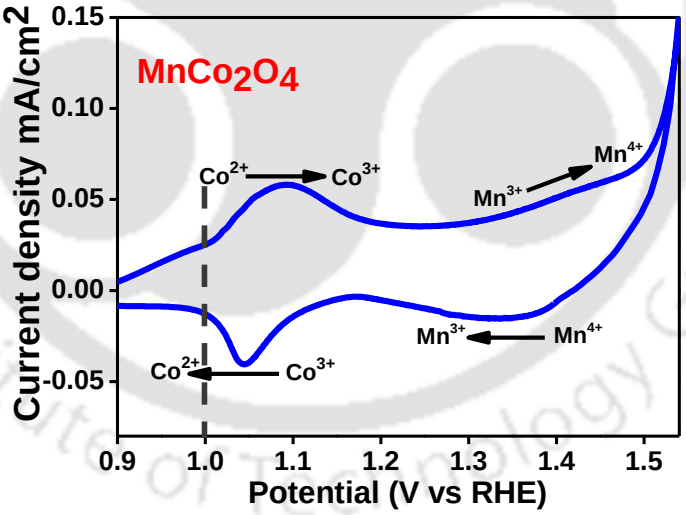

Figure 6.11. Cyclic voltammogram showing (Co^{2+}/ Mn^{3+} ↔ Co^{3+}/Mn^{4+}) redox cycle in bare C-MCO.

To further understand the cause for the enhancement in OER activity of C-MCO/h-BN with the incorporation of h-BN nanosheets, electrochemical surface area (ECSA) calculations were done. ECSA of an electrocatalyst is indicative of the number of electrochemically active sites present. The ECSA value of C-MCO/h-BN, C-MCO, h-BN, and RuO_2 were calculated

TH-2636_166122040

Part of this chapter has been published in **ACS Appl. Energy Mater:** 2022, 5, 1551

from the cyclic voltammetric measurements as shown in **Figure 6.12 (a, b, c, d)** respectively. Cyclic voltammetric measurements of each electrode were done at different scan rate (1-6) mV/sec. For maximum accuracy in C_{dl} estimation, we have avoided faradaic current zone and did cyclic voltammetry measurements of C-MCO and C-MCO/h-BN in the same potential range (0.965 – 1.025 V) vs RHE. They were measured at potentials sufficiently cathodic of the OER activity (non-faradaic region), and also away from metal cations redox features (**Figure 6.11**).[34] The C_{dl} value of all the catalysts was estimated at 1.0 V vs RHE. ECSA is directly propositional to double layer capacitance (C_{dl}), consequently, ECSA of pristine C-MCO and C-MCO/h-BN can be directly estimated by calculating their C_{dl} value from their respective cyclic voltammogram. The difference in current density (j_{anode} - $j_{cathode}$) of C-MCO/h-BN and C-MCO electrodes were plotted against the scan rate to calculate their respective slope values, whereas C_{dl} is half of the slope value, shown in **Figure 6.12 (e)**.[35]

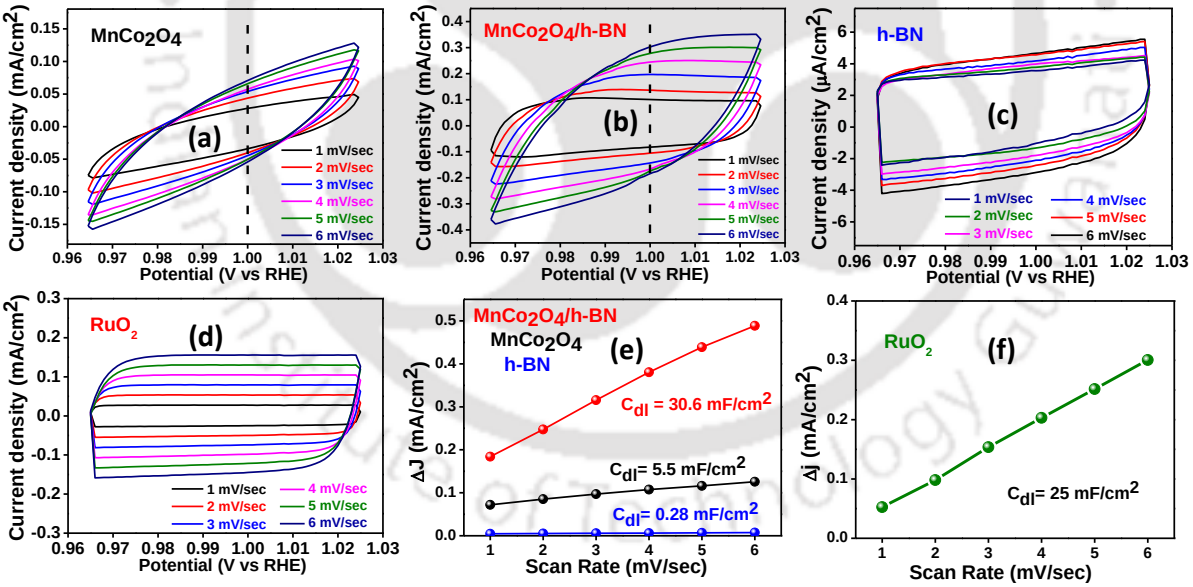

Figure 6.12. Cyclic voltammetry plot at different scan rates (1-6) mV/sec in the non-faradaic region of (a) C-MCO, (b) C-MCO/h-BN, (c) h-BN, (d) RuO_2. (c) double layer capacitance (C_{dl}) plot of C-MCO/h-BN, pristine C-MCO, h-BN, (d) RuO_2.

The C_{dl} value for surface modified heterostructure was calculated to be 30.6 mF/cm^2, while pristine C-MCO shows C_{dl} value of 5.5 mF/cm^2. The metal free h-BN nanosheets

modified C-MCO heterostructure displays a ~5.5-fold increase in C_{dl} value. While C_{dl} value of pristine h-BN and RuO_2 was calculated to be 0.28 mF/cm^2 and 25 mF/cm^2 respectively, shown in **Figure 6.12 (e)** and **Figure 6.12 (f)** respectively.

Turnover frequency (TOF) of C-MCO/h-BN, pristine C-MCO, and pristine h-BN electrodes were determined to estimate the number of oxygen molecules formed from the active sites of the electrocatalyst per unit time, at an operating potential of 1.53 V vs RHE, shown in **Figure 6.13**. To determine the TOF of the electrocatalyst for OER activity, the concentration of active sites (N_S) must be quantified first. The anodic current values were plotted against different scan rates, from the cyclic voltammogram of C-MCO/h-BN and pristine C-MCO, where they show a linear relationship. The slope of the catalysts was calculated using **equation 6.1**[36, 35]

$$Slope\left(\frac{J_{anodic}}{Scan\ rate}\right) = n^2F^2AN_S/4RT \quad \text{----------} \quad (6.1)$$

n (the number of electrons transferred), T (absolute temperature), and R (ideal gas constant). TOF was calculated using **equation 6.2**[37]

$$TOF = \frac{J \times A}{n \times F \times N_S} \quad \text{----------} \quad (6.2)$$

Herein, J (current density at particular overpotential (A/cm^2)), A (surface area of the electrocatalyst (cm^2)), n (number of electrons transferred to evolve a molecule of O_2), F (Faraday constant (96458 C/mol)), and N_S (concentration of active sites of the electrocatalysts (mol/cm^2)).

Surface modified C-MCO/h-BN heterostructure displays TOF of 0.195/sec, while its pristine counterpart shows a lower TOF of 0.07/sec and pristine h-BN shows a TOF value of 0.042/sec. The ~2.8-fold enhancement in TOF in the composite is due to the high hole

TH-2636_166122040

Part of this chapter has been published in **ACS Appl. Energy Mater:** 2022, 5, 1551

extracting ability of negatively charged h-BN nanosheets, efficient OER kinetics, and enhancement in charge transfer kinetics at the working electrode-electrolyte interface.

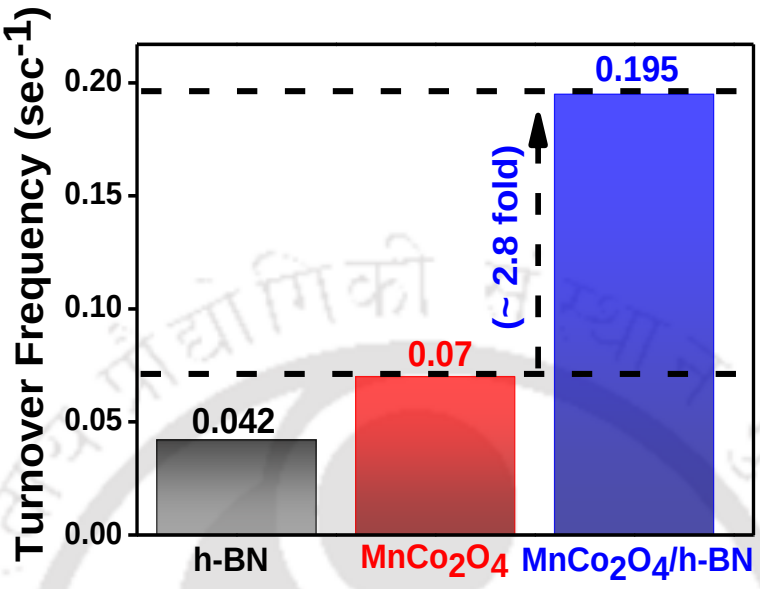

Figure 6.13. Turnover frequency (TOF) of C-MCO/h-BN, pristine C-MCO, and pristine h-BN.

6.3.8 Faradaic Yield and Stability Measurements

The Faradaic yield measurement of C-MCO/h-BN was performed to understand that the gas evolved during the OER process is owing to the oxidation of water and not due to the probable side reactions/products. Measurement of C-MCO/h-BN was performed with three electrodes system in an airtight electrochemical cell using 1 M KOH as an electrolyte (pH = 13), via chronoamperometry technique, at an applied potential of 1.47 V vs RHE. The amount of gas that evolved during the OER process was measured through an on-line gas chromatograph (GC), where argon was used as a carrier gas. Until 2 h of the OER process, after every 10 minutes, the amount of oxygen (O_2) gas evolved was measured using the GC. The theoretical calculation for the amount of gas evolved was done by using **equation 6.3**[38]

$$Amount\ of\ gas\ evolved = \frac{(J.t)}{(n.F)} \qquad \text{----------} \qquad (6.3)$$

Where J (current density (A/cm^2)), t (time (sec)), n (number of moles charge required to produce one mole of gas), and F (Faraday constant 96485 (C/mol)). The Faradaic yield was calculated using **equation 6.4**[38]

$$Faradaic\ yield = \frac{(amount\ of\ gas\ evolved\ measured\ experimentally)}{(amount\ of\ gas\ \ calculated\ theoretically)} \quad \text{-----} \quad (6.4)$$

Figure 6.14. (a) shows the Faradaic yield of C-MCO/h-BN alongside the amount of gas that evolved during the OER process. The Faradic yield of ~97% was obtained for the composite, confirming the current density obtained in **Figure 6.9. (a)** is solely due to the OER activity of the catalyst.

An additional critical parameter to validate the goodness of electrochemical performance is the long-term stability of the electrocatalysts. Stability tests of composite and its pristine counterpart were done in 1 M KOH solution at an applied potential of 1.6 V vs RHE, as shown in **Figure 6.14 (b)**. No significant decay in current density was observed in both C-MCO/h-BN and pristine C-MCO electrodes, holding constant electrocatalytic activity till 35 h of the OER process. LSV curve of the composite is shown in the inset of **Figure 6.14 (b)**, which displays no significant change in OER activity of C-MCO/h-BN before and after the stability test.

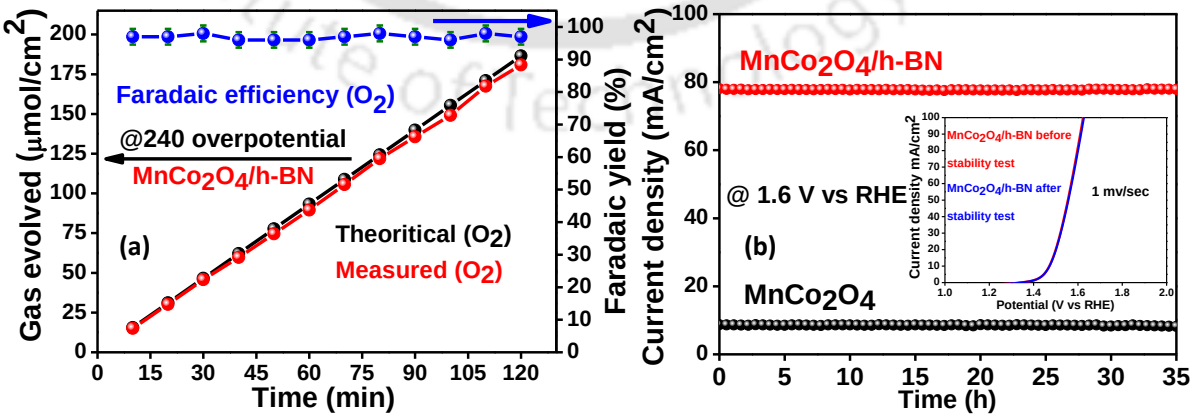

Figure 6.14. (a) The amount of oxygen gas evolved and the Faradaic yield of C-MCO/h-BN. (b) Long-term stability test of C-MCO/h-BN and pristine C-MCO electrodes at 1.6 V vs RHE in 1 M KOH solution. Both the electrode displays outstanding stability, showing constant current density till 35 h of OER performance.

The stability of C-MCO/h-BN and C-MCO were further checked by CV measurement. **Figure 6.15 (a, c)** shows 1000 CV cycles of C-MCO and C-MCO/h-BN respectively, performed at the scan rate of 10 mV/sec in the non-faradaic region. **Figure 6.15 (b, d)** shows an insignificant change in OER performance of both bare and composite electrodes, before and after their respective CV cycles, which further verifies the stability of both the electrodes.

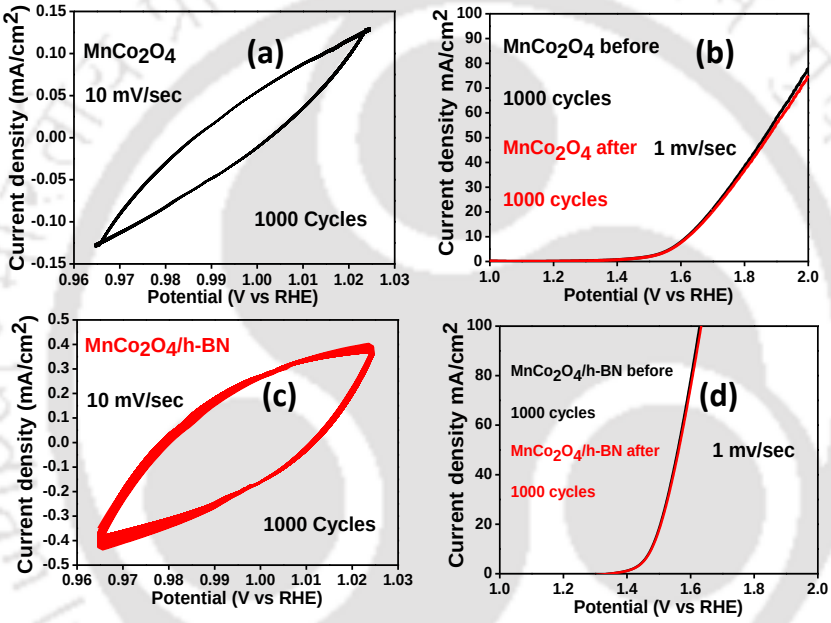

Figure 6.15. To check the stability of the C-MCO/h-BN and its bare counterpart. (a, c) 1000 cycles of cyclic voltammetry of C-MCO and C-MCO/h-BN respectively, at the scene rate of 10 mV/sec in a non-faradic region. (b, d) Current density of composite bare C-MCO and C-MCO/h-BN measured before and after 1000 cycles.

6.3.9 Possible Mechanism

Possible mechanistic pathway for enhanced OER activity in metal free surface modified C-MCO/h-BN heterostructure was discussed in **Scheme 6.3 (a)**.[9] In C-MCO, electrons and holes generates upon application of potential across the electrode. Holes generated in C-MCO travel towards its surface, oxidising Mn^{3+} to Mn^{4+} and Co^{2+} to Co^{3+}, while the electrons move towards the interface of FTO and C-MCO. The Mn^{4+} and Co^{3+} ions at the active sites of C-

TH-2636_166122040
Part of this chapter has been published in **ACS Appl. Energy Mater:** 2022, 5, 1551

MCO surface oxidises water to produce O_2 molecules. The electrons generated during water oxidation process, reduce Mn^{4+} and Co^{3+} ions back to Mn^{3+} and Co^{2+} ions. In C-MCO/h-BN, h-BN nanosheets helps faster restoration of original oxidation states in manganese and cobalt ions during OER activity. Here in the composite, h-BN nanosheets extracts holes generated in C-MCO, further, the holes were utilized for OER activity at the surface of h-BN nanosheets. Redox cycles taking place in the above-discussed mechanism was supported by cyclic voltammetry of C-MCO, shown in **Figure 6.11**. Voltammogram of C-MCO shows, on the application of a potential across the composite, Mn^{3+}get oxidised to Mn^{4+}, and Co^{2+} into Co^{3+} and vice-versa. **Scheme 6.3 (b)** shows the interaction between nitrogen and oxygen of h-BN and C-MCO respectively, in the composite. Better interaction at the interface allows easy movement of holes from C-MCO to h-BN for enhanced OER activity in the composite. **Figure 6.7 (e)** shows core level XPS spectra of N1s, shift in N1s peak of the composite towards lower binding energy illustrates the interaction between h-BN and C-MCO, through nitrogen and oxygen of h-BN and C-MCO respectively, in the composite.The O1s Core level XPS spectra of pristine C-MCO and C-MCO/h-BN shown in **Figure 6.7 (f)**. Appearance of N-O peak in O1s XPS spectra of composite confirms bonding between nitrogen and oxygen of h-BN nanosheets and C-MCO respectively.

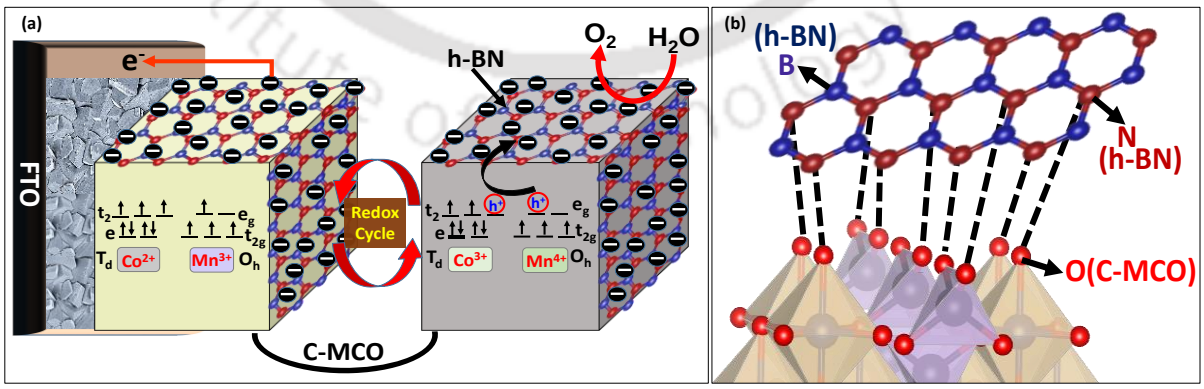

Scheme 6.3. (a) Mechanistic pathway for enhanced OER activity in metal free surface modified C-MCO/h-BN heterostructure. (b) Interaction between nitrogen and oxygen of h-BN and C-MCO respectively in C-MCO/h-BN.

6.4 CONCLUSIONS

In summary, surfactant free cuboidal $MnCo_2O_4$ was grown directly over low-priced FTO substrate by a green hydrothermal method, providing a good ohmic contact, which helps in a smooth transfer of charge carriers between cuboidal $MnCo_2O_4$ and FTO interface. Cuboidal $MnCo_2O_4$ modified with metal-free h-BN nanosheets, exhibits excellent hole extraction ability assisting in the upsurge of OER activity in C-MCO/h-BN heterostructure. C-MCO/h-BN displays an overpotential of 240 mV and a Tafel slope value of 66 mV/dec, making the electrode an efficient OER active catalyst. Surface modified C-MCO/h-BN shows efficient charge transfer kinetics at the working electrode and the electrolyte interface, with an R_{ct} value of 3.9 Ω. Moreover, C-MCO/h-BN shows ~5.5-fold enhancement in C_{dl} than its pristine counterpart, indicating more accessible electrochemically surface-active sites on it, therefore ~ 2.8-fold enhancement in TOF was observed. Green and sustainable C-MCO/h-BN electrode, shows excellent OER activity and exhibits 35 h of outstanding long-term stability in harsh alkaline conditions, thus it has the potential to be used in large-scale industrial application.

6.5 REFERENCES

1. S. E. Schwartz. *Energy Environ. Sci.*, 2008, **1**, 430.
2. I. Roger, M. A. Shipman, M. D. Symes. *Nature Reviews Chemistry*, 2017, **1**, 1.
3. S. Anantharaj, S. R. Ede, K. Sakthikumar, K. Karthick, S. Mishra, S. Kundu, *ACS Catal.*, 2016, **6**, 8069.
4. F. Song, L. Bai, A. Moysiadou, S. Lee, C. Hu, L. Liardet, X. Hu. *J. Am. Chem., Soc.*, 2018, **140**, 7748.
5. Q. Shi, C. Zhu, D. Du, Y. Lin. *Chem. Soc. Rev.*, 2019, **48**, 3181.
6. T. Bhowmik, M. K. Kundu, S. Barman. *ACS Appl. Mater. Interfaces*, 2016, **8**, 28678.
7. K. Zhang, R. Zou, *Small*, **2021**, 2100129.

TH-2636_166122040

Part of this chapter has been published in **ACS Appl. Energy Mater:** 2022, 5, 1551

8. J. Han, S. Hao, Z. Liu, A. M. Asiri, X. Sun, Y. Xu. *Chem. Commun.*, 2018, **54**, 1077.

9. A. K. Shah, S. Bhowmick, D. Gogoi, N. R. Peela, M. Qureshi, *Chem. Commun.*, 2021, **57**, 8027.

10. S. Hao, Y. Yang, *J. Mater. Chem. A*, 2017, **5**, 12091.

11. X. Huang, H. Zheng, G. Lu, P. Wang, L. Xing, J. Wang, G. Wang, *ACS Sustainable Chem. Eng.*, 2019, **7**, 1169.

12. P. W. Menezes, A. Indra, N. R. Sahraie, A. Bergmann, P. Strasser, M. Driess. *ChemSusChem*, 2015, **8**, 164.

13. F. Lyu, Q. Wang, S. M. Choi, Y. Yin. *Small*, 2019, **15**, 1804201.

14. C.X. Zhao, J.N. Liu, J. Wang, D. Ren, B.Q. Li, Q. Zhang *Chem Soc Rev*, 2021, **50**, 7745.

15. K. Zhang, Y. Feng, F. Wang, Z. Yang, J. Wang. *J. Mater. Chem. C*, 2017, **5**, 11992.

16. S. Chen, Y. Li, Z. Zhang, Q. Fu, X. Bao. *J. Mater. Chem. A*, 2018, **6**, 10644.

17. R. Han, F. Liu, X. Wang, M. Huang, W. Li, Y. Yamauchi, X. Sun, Z. Huang, *J. Mater. Chem. A*, 2020, **8**, 14384.

18. S. Meng, X. Ye, X. Ning, M. Xie, X. Fu, S. Chen. *Appl. Catal. B*, 2016, **182**, 356.

19. T. K. Mukhopadhyay, A. Datta, *J. Phys. Chem. C*, 2017, **121**, 811.

20. R. B. Waghmode, N. C. Maile, D. S. Lee, A. P. Torane. *Electrochim. Acta*, 2020, **350**, 136413.

21. J. M. Gonçalves, M. N. Silva, T. K. K. Naik, P. R. Martins. *J. Mater. Chem. A*, 2020, **9**, 3095.

22. L. Trotochaud, S. L. Young, J. K. Ranney, S. W. Boettcher. *J. Am. Chem. Soc.*, 2014, **136**, 6744.

23. Y. Sheng, J. Yang, F. Wang, L. Liu, H. Liu, C. Yan, Z. Guo. *Appl. Surf. Sci.*, 2019, **465**, 154.

TH-2636_166122040

 Part of this chapter has been published in **ACS Appl. Energy Mater:** 2022, 5, 1551

24. A. Guha, T. V. Vineesh, A. Sekar, S. Narayanaru, M. Sahoo, S. Nayak, S. Chakraborty, T. N. Narayanan, *ACS Catal.*, 2018, **8**, 6636.

25. V. Venkatachalam, A. Alsalme, A. Alghamdi, R. Jayavel, *J. Electroanal. Chem.*, 2015, **756**, 94.

26. S. Yuvaraj, A. Vignesh, S. Shanmugam, R. K. Selvan. *Int. J. Hydrogen Energy*, 2016, **41**, 15199.

27. M. K. Mohanta, T. K. Sahu, D. Gogoi, N. R. Peela, M. Qureshi. *ACS Appl. Energy Mater*., 2019, **2**, 7457.

28. V. Yadav, V. Kulshrestha. *Nanoscale*, 2019, **11**, 12755.

29. D. Y. Guo, Z. P. Wu, Y. H. An, X. J. Li, X. C. Guo, X. L. Chu, C. L. Sun, M. Lei, L. H. Li, L. X. Cao, P. G. Li, W. H. Tang. *J. Mater. Chem. C.*, 2015, **3**, 1830.

30. Y. Zhai, H. Mao, P. Liu, X. Ren, L. Xu, Y. Q. Qian. *J. Mater. Chem. A.*, 2015, **3**, 16142.

31. Y. Chen, J. Cai, P. Li, G. Zhao, G. Wang, Y. Jiang, J. Chen, S. X. Dou, H. Pan, W. Sun. *Nano Lett.*, 2020, **20**, 6807.

32. I.M. Patil, A. Swami, R. Chavan, M. Lokanathan, B. Kakade. *ACS Sustainable Chem. Eng.*, 2018, **6**, 16886.

33. K. Fan, H. Chen, Y. Ji, H. Huang, P. M. Claesson, Q. Daniel, B. Philippe, H. Rensmo, F. Li, Y. Luo, L. Sun. *Nat Commun.*, 2016, **7**, 11981.

34. M. B. Stevens, L. J. Enman, A. S. Batchellor, M. R. Cosby, A. E. Vise, C. D. M. Trang, S. W. Boettcher. *Chem. Mater.*, 2017, **29**, 120.

35. L. Kumar, M. Chauhan, P. K. Boruah, M. R. Das, S. A. Hashmi, S. Deka, *ACS Appl. Energy Mater.*, 2020, **3**, 6793.

36. Y. Li, L. Zhang, X. Xiang, D. Yan, F. Li. *J. Mater. Chem. A.*, 2014, **2**, 13250.

37. X. Zhang, C. Si, X. Guo, R. Kong, F. *J.* Qu. *Mater. Chem. A*, 2017, **5**, 17211.

38. C. Jiang, S. J. Moniz, A. Wang, T. Zhang, J. Tang. *Chem. Soc. Rev.*, 2017, **46**, 4645.

TH-2636_166122040

Part of this chapter has been published in **ACS Appl. Energy Mater:** 2022, 5, 1551

CHAPTER 7

Thesis overview and future perspectives

This chapter, in brief, outlines the outcomes and the overview of the current thesis. Herein, it also discusses the possible modification in the near future that can be done with the metal oxides to enhance OER and HER performance.

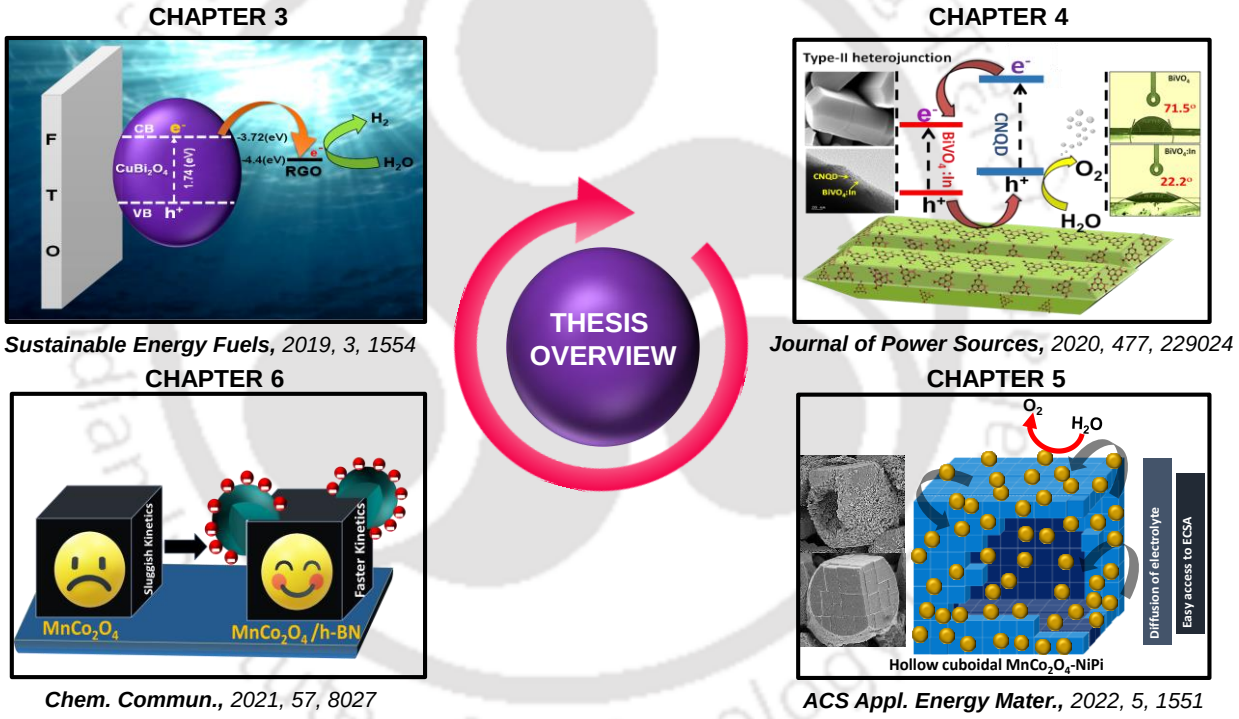

Sustainable Energy Fuels, *2019, 3, 1554*

Journal of Power Sources, *2020, 477, 229024*

Chem. Commun., *2021, 57, 8027*

ACS Appl. Energy Mater., *2022, 5, 1551*

TH-2636_166122040

Thesis Overview:

The present thesis primarily focused on design and development of in-situ grown metal oxide-based catalysts for efficient oxygen evolution reaction (OER) and hydrogen evolution reaction (HER). Herein, metal oxide semiconductors such as $CuBi_2O_4$ and $BiVO_4$ were used as a model system to carry out photoelectrochemical water splitting, while $MnCo_2O_4$ was used as an electrocatalyst to perform electrocatalytic water splitting. The formation of heterojunction using a co-catalyst, elemental doping, hole/electron extractor catalyst, and morphological changes are a few techniques that were tried on the metal oxide semiconductors to enhance their water-splitting efficiency. In the synthesis of the catalyst, importance was given to their direct growth over the substrate, which allows efficient transfer/ injection of charge carriers at the interface of the semiconductor and the substrate. In the current thesis, priority was given for the fabrication of working electrodes that are environment-friendly and cost-effective, along with developing them through a simple synthetic protocol. This thesis is arranged as follows: firstly, the introduction is given on the global energy consumption and environmental challenges, need for a sustainable energy source to produce zero-emission H_2/O_2 gas, in **Chapter 1**. Chapter 1 discusses in detail (photo)electrochemical techniques where H_2 is produced by water splitting. The basic principle of (photo)electrochemical water splitting and different strategies to enhance the water-splitting efficiency of the semiconductor were also discussed. A brief literature survey on the current state-of-the-art as well as challenges related to the fabrication of the electrodes is also discussed. At last, this chapter is concluded with the objectives of the present thesis. In **Chapter 2**, different instrumental techniques, performance parameters, and different experimental setups, which were adopted for the characterization, and determination of water splitting performance of the fabricated electrodes', were discussed in detail. The summary and conclusions for each chapter i.e. **chapter 3** to **chapter 6** provide

TH-2636_166122040

some valuable outcomes which are obtained from the work done during my Ph.D. tenure and summarized as follows:

- In **chapter 3**, we have proposed a noble metal-free, p-type $CuBi_2O_4$ directly fabricated over FTO, overlaid with reduced graphene oxide (RGO). Herein, we found that with the gradual deposition of RGO over $CuBi_2O_4$, there was an enhancement in the HER performance of the photocathode. The optimized number of RGO deposition cycles displayed the photocurrent density which was ~2-fold higher than that of the bare $CuBi_2O_4$ photocathode. It was also observed that with RGO modification over $CuBi_2O_4$ charge carrier density increases from 3.76 x 10^{20} cm^{-3} to 7.92 x 10^{20} cm^{-3}. A significant increase in photocurrent density in the modified electrode was due to efficient charge separation in the bulk and enhanced charge injection at the photocathode and electrolyte interface, owing to an efficient charge transfer from $CuBi_2O_4$ to RGO.
- In **chapter 4**, due to suitable band structure and stability, with a theoretical current density approaching 7 mA/cm^2, we have chosen monoclinic $BiVO_4$ as a model system for photoelectrochemical water oxidation. Herein, $BiVO_4$ with indium doping ($BiVO_4$:In) was grown directly over the substrate yield distinctive morphology. It was observed that indium doping in $BiVO_4$ favors the creation of oxygen vacancies, which improves charge separation and charge carrier density in $BiVO_4$:In photoanode. It was also observed that the $BiVO_4$:In photoanode shows higher surface hydrophilic characteristics, resulting in a more polar surface, leading to more active water at the reaction site. This photoanode forms a type II heterojunction ($BiVO_4$:In)-CNQD) with g-C_3N_4 quantum dots (CNQD) loading to address the shortcomings. A photocurrent density of ~2.42 mA/cm^2 with a cathodic shift of 136 mv was obtained in the dual modified electrode which was ~4-folds higher than its bare counterpart.

TH-2636_166122040

- In **chapter 5**, we have grown a hierarchical hollow cuboidal structure of $MnCo_2O_4$ directly over FTO substrate by a green hydrothermal procedure. In-situ growth of hollow cuboidal $MnCo_2O_4$ (h-MCO) over FTO provides good ohmic contact, helping in faster charge transfer between h-MCO and FTO substrate. It was observed that the deposition of NiPi over h-MCO enhances the OER activity of h-MCO/NiPi electrode to a lower overpotential of 230 mV and Tafel slope to 57 mV/dec. It was also witnessed that the surface modification using NiPi over h-MCO enhances the charge transfer kinetics of the modified electrode, resulting in faster charge transfer at the interface of the working electrode and the electrolyte. The enhancement of electrochemically surface active sites in the composite was also observed than its pristine counterpart. h-MCO/NiPi shows excellent long-term stability of 30 h without any significant decrease in current density. High stability, low cost, and green synthesis procedure mark h-MCO/NiPi as one of the futuristic catalysts to be used in industrial applications.
- In **chapter 6**, we have grown surfactant-free cuboidal $MnCo_2O_4$ (C-MCO) directly over the FTO substrate, for OER activity. C-MCO modified with metal-free h-BN nanosheets, which exhibits excellent hole extraction ability assisting in the upsurge of OER activity in C-MCO/h-BN heterostructure. C-MCO/h-BN displays an overpotential of 240 mV and a Tafel slope value of 66 mV/dec, making the electrode an efficient OER active catalyst. Moreover, C-MCO/h-BN shows ~5.5-fold enhancement in C_{dl} than its pristine counterpart, indicating more accessible electrochemically surface-active sites on it. The ~2.8-fold enhancement in TOF in the composite was noticed, which was due to the high hole extracting ability of negatively charged h-BN nanosheets, efficient OER kinetics, and enhancement in charge transfer kinetics at the working electrode-electrolyte interface. Green and sustainable C-MCO/h-BN

TH-2636_166122040

electrode, shows excellent OER activity and exhibits 35 h of outstanding long-term stability in harsh alkaline conditions.

Future Perspectives

In the current thesis, a detailed study on the metal oxide-based catalysts (photo and electro) was carried out to resolve issues related to charge carrier recombination, interfacial charge transfer resistance, ohmic contact at the interface, electrochemical surface active sites, and reaction kinetics. The research finding carried out in this thesis provides several scopes for the design and fabrication of heterojunction electrodes, it also offers a detailed study on the charge transfer mechanism in the heterojunction. Strategies adopted here have made substantial advancements in the field of (photo)electrochemical water splitting, still, numerous scopes are available to further improve the water-splitting efficiency of the metal oxides. The water-splitting efficiency of the metal oxides is still lower than their theoretical efficiency. There are several scopes to carry forward the current research study which are as follows:

- Though low bandgap $CuBi_2O_4$ absorbs a major portion of the solar spectrum, the high recombination rate inside the p-type $CuBi_2O_4$ is the major reason for its lower efficiency. Thereby, the formation of p-n heterojunction should reduce recombination in $CuBi_2O_4$, hence enhancing the HER efficiency of $CuBi_2O_4$.
- Fabricating nanostructures with a high surface area to solve the issue of lower diffusion length and enhance the number of reaction sites in $CuBi_2O_4$ photocathode.
- Synthesising $BiVO_4$ 3D-nanostructures will help in enhancing its exposed surface area to the electrolyte, hence improving its water oxidation performance.
- Use of redox couples over the surface of $BiVO_4$ to overcome the surface trap sites in the semiconductor.

TH-2636_166122040

- The overpotential of $MnCo_2O_4$ is still higher than the theoretical water splitting potential, doping in $MnCo_2O_4$ will be an important strategy to enhance its intrinsic conductivity, and increase the number of electrochemically active sites for better OER activity.
- Use of metal atom embedded single-layer materials over the surface of spinel $MnCo_2O_4$ to overcome its poor interfacial charge transfer resistance and poor electrochemically active sites.

TH-2636_166122040

LIST OF PUBLICATIONS AND CONFERENCES/WORKSHOPS ATTENDED

Journal Articles:

Included in Thesis:

1. **Adit Kumar Shah**, et al., Reduced graphene oxide modified $CuBi_2O_4$ as an efficient and noble metal free photocathode for superior photoelectrochemical hydrogen production, **Sustainable Energy Fuels**, 2019, 3, 1554.
2. **Adit Kumar Shah**, et al, Surface-engineering of decahedron shaped bismuth vanadate for improved photoelectrochemical water oxidation by indium doping coupled with graphitic carbon nitride quantum dots, **J. Power Sources**, 2020, 477, 229024.
3. **Adit Kumar Shah**, et al, Hollow cuboidal $MnCo_2O_4$ coupled with nickel phosphate: a promising oxygen evolution reaction electrocatalyst, **Chem. Commun.**, 2021, 57, 8027.
4. **Adit Kumar Shah** and Mohammad Qureshi, In-situ grown cuboidal $MnCo_2O_4$/h-boron nitride heterojunction: A noble metal-free approach based on efficient hole extraction for electrochemical oxygen evolution reaction, **ACS Appl. Energy Mater.** ACS Appl. Energy Mater., 2022, 5, 1551.

Work Contributed Off the Thesis:

1. Tushar Kanta Sahu, **Adit Kumar Shah**, et al, Effect of surface overlayer in enhancing the photoelectrochemical water oxidation of in situ grown one-dimensional spinel zinc ferrite nanorods directly onto the substrate, **Chem. Commun.,** 2018, 54, 10483.
2. Tushar Kanta Sahu, **Adit Kumar Shah**, et al., Enhanced surface and bulk recombination kinetics by virtue of sequential metal and nonmetal incorporation in hematite-based photoanode for superior photoelectrochemical water oxidation, **ACS Appl. Energy Mater.** 2019, 26, 4325.

TH-2636_166122040

3. Sourav Bhowmick, et al, Bimetallic cyclic redox couple in di-manganese copper oxide supported by nickel borate for boosted alkaline electrocatalytic oxygen evolution reaction, **Sustainable Energy Fuels,** 2021, 5, 2517.
4. Devipriya Gogoi, **Adit Kumar Shah**, et al., Silver grafted graphitic-carbon nitride ternary hetero-junction Ag/g-C_3N_4 (Urea)-g-C_3N_4 (Thiourea) with efficient charge transfer for enhanced visible-light photocatalytic green H_2 production, **Appl. Surf. Sci.,** 2021, 558, 149900**.**
5. Devipriya Gogoi, **Adit Kumar Shah,** et al., Step-scheme heterojunction between CdS nanowires and facet selective assembly of Mno_x-$BiVO_4$ for an efficient visible-light-driven overall water splitting, **ACS Appl. Mater. Interfaces,** 2021, 13, 45475.

Conferences/Workshops:

1. 5th International Conference on Advanced Nanomaterials and Nanotechnology (**ICANN-2017**), 18-21 December 2017, Indian Institute of Technology Guwahati, Guwahati, India (**Poster Presented & Volunteer**)
2. **Research Conclave'17**, 16-19 March 2017, Indian Institute of Technology Guwahati, Guwahati, India (**Poster Presented**)
3. 3rd National Workshop on MEMS/NEMS and Theranostic Devices, 21-23 March, 2017, Indian Institute of Technology Guwahati, Guwahati, India (**Attended**)
4. Full agenda of ACS on Campus at IIT Guwahati on Monday, January 16, 2017. (**Attended**)
5. One-Day Workshop on Vacuum Technology and its Application in Optical Science, Jointly Organized by SPIE IIT Guwahati Student Chapter and Pfeiffer Vacuum Pvt. Ltd., in association with Department of Physics, IIT Guwahati on 19th August, 2017 at Guwahati. (**attended**)

6. International Conference on Frontiers in Chemical Sciences (**FICS-2018**), 6-8th December 2018, Indian Institute of Technology Guwahati, Guwahati, India. (**Poster Presented**)
7. 6th International Conference on Advanced Nanomaterials and Nanotechnology (**ICANN-2019**), 18-21 December, 2019, Indian Institute of Technology Guwahati, Guwahati, India. (**Poster Presented**)
8. The international event "Conference on Electrochemistry in industry, Health an Environment" (**EIHE-2020**) held at Dae Convention Centre, Anushaktinagar, Bhabha Atomic Research Centre, Mumbai, India, During January 21-25, 2020. (**Oral presentation**)